

TWO-DIMENSIONAL MODELING OF PULSED INDUCTIVELY COUPLED PLASMAS
USING MODERATE PARALLELISM

BY

PRAMOD SUBRAMONIUM

B.Tech., Indian Institute of Technology, Madras, 1999

THESIS

Submitted in partial fulfillment of the requirements
for the degree of Master of Science in Chemical Engineering
in the Graduate College of the
University of Illinois at Urbana-Champaign, 2001

Urbana, Illinois

(RED BORDERED SIGNATURE PAGE HERE)

TWO-DIMENSIONAL MODELING OF PULSED INDUCTIVELY COUPLED PLASMAS USING MODERATE PARALLELISM

Pramod Subramonium, M.S.
Department of Chemical Engineering
University of Illinois at Urbana-Champaign, 2001
Mark J. Kushner, Advisor

Quantifying transient plasma processing phenomena such as startup, shutdown, recipe changes, and pulsed operation is important to optimizing plasma and materials properties. These long term phenomena are difficult to resolve in multi dimensional plasma equipment models due to the large computational burden. Hybrid models, which sequentially execute modules, may not be adequate to resolve the physics of transients. In the present study, we developed a new numerical technique in which a moderately parallel implementation of a 2-D Hybrid Plasma Equipment Model (HPEM) is used to address long term transients. In this implementation, the Electromagnetics Module (EMM), the Electron Energy Transport Module (EETM), and the Fluid Kinetics Simulation (FKS) of the HPEM are executed in parallel.

The model is employed to study the transient behavior in the pulsed operation of ICPs. The consequences of varying pulse repetition frequency, duty cycle, power, and pressure on the plasma properties are quantified. The investigations are performed in Ar and Ar/Cl₂ plasmas. The spatiotemporal dynamics of plasma properties such as electron density, electron temperature, and plasma potential are discussed. In Ar/Cl₂ plasmas, it was possible to extract negative ions from the plasma during the off period. The model predictions compared well with the experimental results.

ACKNOWLEDGMENTS

First and foremost, I would like to express my profound gratitude to my advisor, Prof. Mark J. Kushner, whose constant support and valuable suggestions have been the principal force behind my work. I am extremely thankful to him for showing me the right direction when I encountered difficulties. He has expanded my understanding of plasma physics tremendously. This work would not have been possible without his help and inspiration.

I would like to acknowledge the support of the Semiconductor Research Corporation (SRC) and National Science Foundation (NSF). I am also thankful to Dr G. A. Hebner for providing us with experimental data for comparison purposes and with valuable suggestions.

I am also thankful to my fellow members in the Computational Optical and Discharge Physics Group: Ron Kinder, Da Zhang, Junqing Lu, Kelly Collier, Dan Cronin, Rajesh Dorai, Brian Lay, Arvind Sankaran, Kapil Rajaraman, and Dyutiman Das. I would also like to thank Sony Joseph, a graduate student in theoretical and applied mechanics, and Mathew George, a graduate student in computer science, for their suggestions for resolving some of the parallel programming issues.

I am most indebted to my parents and relatives for their constant support and encouragement throughout the course of my education.

TABLE OF CONTENTS

	Page
1. INTRODUCTION	1
1.1 Pulsed Plasmas.....	1
1.2 Experimental Studies on Pulsed Plasmas.....	1
1.3 Modeling of Pulsed Plasmas.....	6
1.4 Conclusions.....	9
1.5 References.....	13
2. DESCRIPTION OF THE MODEL.....	15
2.1 Introduction.....	15
2.2 Hybrid Plasma Equipment Model (HPEM).....	15
2.3 The Electromagnetics Module (EMM).....	16
2.4 The Electron Energy Transport Module (EETM)	17
2.5 The Fluid Kinetics Simulation (FKS).....	19
2.6 Parallel HPEM	22
2.6.1 Variables: shared or private.....	25
2.6.2 Dynamic load balancing.....	26
2.6.3 Validation of the parallel hybrid model.....	28
2.6.4 Performance evaluation.....	29
2.7 Conclusions.....	30
2.8 References.....	35
3. INVESTIGATIONS OF ARGON PULSED PLASMAS	36
3.1 Introduction.....	36
3.2 Comparison with Experiments	36
3.3 Base Case Conditions	38
3.4 Effect of Duty Cycle.....	39
3.5 Effect of Power	43
3.6 Effect of Pulse Repetition Frequency.....	44
3.7 Effect of Pressure.....	46
3.8 Conclusions.....	47
3.9 References.....	68
4. INVESTIGATIONS OF Ar/Cl ₂ PULSED PLASMAS.....	69
4.1 Introduction.....	69
4.2 Comparison with Experiments	69
4.3 Base Case Conditions	70
4.4 Effect of Duty Cycle.....	72
4.5 Effect of Power	77
4.6 Effect of Pulse Repetition Frequency.....	78
4.7 Effect of Pressure.....	80
4.8 Conclusions.....	82
4.9 References.....	104

5. CONCLUSIONS.....	105
APPENDIX A: LIST OF REACTIONS FOR Ar.....	107
APPENDIX B: LIST OF REACTIONS FOR Ar/C ₂	108

1. INTRODUCTION

1.1 Pulsed Plasmas

Low pressure, high plasma density discharges are gaining importance for advanced semiconductor processing in the fabrication of fine features in microelectronics. To meet the stringent requirements, novel methods of plasma operation are investigated. The demand for plasma etching processes with better uniformity, anisotropy, and selectivity has led to the development of high plasma density sources such as inductively coupled plasmas (ICP) and electron cyclotron resonance (ECR) plasmas. ICPs provide the process design engineer with added ability to decouple bulk plasma characteristics from ion energy distribution incident on the wafer surface, which in turn affects the etching rates and deposition uniformity. The operating characteristics of these sources can be improved by modulating the radio frequency (rf) power deposited into the plasma. This proposal has led to the use of power modulated plasmas or "pulsed plasmas" in semiconductor processing. *Power modulated plasmas* technically refers to the mode of plasma operation in which the rf power to the inductively coupled coil is modulated at a predetermined frequency and duty cycle.

1.2 Experimental Studies on Pulsed Plasmas

Earlier studies¹⁻⁷ of pulsed plasmas have shown that, compared to continuous wave (cw) operation, they enable improved etch or deposition rate, uniformity and etch selectivity by modifying the fluxes of species incident on the wafer. Recently, pulsed plasmas have been used to suppress etching anomalies such as "notching" by reducing

charge buildup in features.⁸ By varying the modulation frequency and duty cycle, pulsed plasmas extend the range of continuous wave operation with additional degrees of freedom⁹. Thus, it is possible to optimize and control the performance of processing plasmas by varying these parameters in addition to conventional control parameters such as gas pressure, flow rate and input power. Pulsed operation of ECR²⁻⁷ and helicon¹⁰ plasmas can produce highly selective, anisotropic etching with higher rates.

Malyshev et al.¹⁰ investigated the temporal dynamics of pulsed chlorine plasmas. Their studies were performed in a transformer coupled plasma reactor at pressures between 3 mTorr and 20 mTorr with average power of 500 W, pulse repetition frequency of 10 kHz, and duty cycle of 50%. Electron density during the on period reached a peak of $1 \times 10^{10} \text{ cm}^{-3}$. During the off period, they observed a large degree of modulation in electron density, nearly two orders of magnitude lower with a characteristic decay time of approximately 30 μs . Hebner et al.⁹ also investigated pulse-modulated ICPs in argon and chlorine. Measurements were performed for peak rf powers between 150 W and 400 W at 13.56 MHz, duty cycles between 10% and 70%, and pulse repetition frequencies between 3 and 20 kHz. Their results indicate that during the first 5-30 rf cycles of each time modulated pulse, the discharge may operate in a capacitive discharge mode with rf variations in plasma potential and relatively low electron density. The steady state electron density is observed to be a function of duty cycle in a chlorine plasma, which may be due to the varying ratio of Cl/Cl_2 with duty cycle.

Ashida et al.¹¹ investigated pulsed argon plasmas in ICPs at a pressure of 5 mTorr. The time averaged input power in their studies was 80 W and was modulated at a frequency of 10 kHz with duty cycle of 50%. Their measurements indicate that the

plasma density is higher than that for the continuous wave excitation of the same average power and larger densities are obtained at smaller duty ratios. They also observed that electron densities increase monotonically as the period is decreased. Ishigaki et al.¹² measured charged particles and neutral radicals in a pulsed ICP using langmuir probes, quadrupole mass spectrometer, and plasma oscillation method to control etching using CF_4/H_2 mixtures at a pressure of 15 mTorr. Measurements were made at peak rf power of 1 kW at 13.56 MHz, duty cycles between 5% and 100%, and pulse repetition frequencies between 10 kHz and 100 kHz. They observed that the ratio CF_x/F ($x = 2, 3$) increased with decreasing rf on time as time averaged electron temperature decreased with shorter rf on times. Boswell et al.¹ observed that etch rates rise as the pulse length decreases until with 2-ms pulses, the etch rate reaches the continuous rate in pulsed ICPs for etching silicon using SF_6 gas. Their studies were performed at pressures between 5 mTorr and 15 mTorr with peak power of 1 kW modulated at 0.1-0.5 kHz and duty cycle of 20%. A heuristic model of the etching was also developed to accurately predict the pulsed plasma etch rates and to set limits on important parameters, such as the number of F atoms yielded by the SF_6 , the reaction probability of F with Si, and the overall efficiency of the etching process. The model predicted results such as etching rates that matched experiments for pulsed etching of silicon, but it is totally inadequate for predicting etching of silica.

Samukawa et al.^{5, 6} observed highly selective, highly anisotropic, notch-free and damage-free polycrystalline silicon etching using chlorine gas at a pressure of 2 mTorr in pulsed ECR plasmas. Measurements were performed for peak power of 1 kW at 2.45 GHz, duty cycle of 50%, and pulse repetition frequencies between 10 kHz and 100

kHz. Etching characteristics are controllable due to the independent control of the ion density and ion energy distribution. Pulsed operation over the range of a few tens of microseconds suppresses the amount of charge that accumulates in the feature and results in reduced damage. Various researchers^{2, 4, 13} investigated pulse modulated ECRs for etching SiO₂ using CHF₃. Measurements were performed in 2 mTorr discharges for peak input power of 1 kW at 2.45 GHz, duty cycle of 50%, and pulse repetition frequencies between 10 kHz and 100 kHz. Pulsed operation achieves a high ratio of SiO₂ etching to Si etching and reduces microloading effects during SiO₂ contact hole etching. The ratio of CF₂/F in CHF₃ depends largely on the duty cycle. Mieno et al.¹⁴ studied pulsed ECR plasmas in C₂ and argon gases. Measurements were performed in 2 mTorr discharges for peak power of 1 kW at 2.45 GHz, with variable duty cycles and pulse repetition frequencies between 2.5 kHz and 100 kHz. Their study shows that pulse modulation of C₂ plasma produces a large density of negative ions. Pulsed operation also changes the flow of charged particles through the sheath region to the substrate surface¹⁷ as the plasma potential becomes very low in the off period, which enables highly anisotropic and charge-free poly-Si etching.

Maruyama et al.⁸ reported detailed analysis of etching characteristics under various modulations and microwave conditions in pulsed ECRs with chlorine gas to achieve simultaneously no local side etch, high etch rate, and selectivity. Measurements were performed in 50 mTorr discharges for peak power of 4 kW at 2.45 GHz, duty cycle of 50%, and pulse repetition frequency of 5 kHz. They observed that local side etch depth in the region of high aspect ratio reduced as the off time increased, which may be due to the reduction in charge build-up in the features.

Malyshev et al.¹⁹ reported an analysis of the dynamics of a pulsed power, inductively coupled chlorine plasma operated with continuous rf bias applied to the substrate. Their studies were performed in a 10 mTorr chlorine plasma with average power of 500 W at 13.56 MHz, duty cycle of 50%, and pulse repetition frequencies between 0.3 and 10 kHz. The rf bias power on the substrate was 300 W. They observed that there is no significant difference in plasma characteristics with or without rf bias during the on period. In the off period, with rf bias, electron temperature increased rapidly in the late afterglow after dropping down in the early after glow. Electron and ion density continued to decrease in the off period with or without bias and were affected only later in the afterglow.

Samukawa⁷ investigated pulsed ECRs with chlorine gas and low rf substrate bias. Measurements were performed in 2 mTorr discharges for peak power of 1 kW at 2.45 GHz, rf bias power of 100 W, duty cycle of 50%, and pulse repetition frequencies between 10 kHz and 100 kHz. He reported that poly-Si etching improved by increasing the pulse interval of the microwaves to more than 50 μ s for a 50% duty cycle and applying a 600 kHz rf bias to the substrate. This was due to increased generation of negative ions in after glow and acceleration of these ions to the substrate due to the rf bias. High etch rate and reduced charging resulted from alternating acceleration of negative and positive ions to the substrate surface due to the presence of rf bias. Yasaka et al.¹⁵ performed an experimental study of pulsed ECR discharges for deposition of poly-Si films using an Ar/H₂ mixture. Measurements were performed in 0.5 mTorr discharges for peak power of 100-300 W at 2.45 GHz, duty cycle of 50%, and pulse repetition frequency of 1 kHz. A larger selectivity of SiH₃ over SiH₂ was observed using pulsed

operation. As a result, the deposited films contained lower density hydrogenated bonds than those produced using continuous discharges.

Mackie et al.¹⁶ investigated pulsed and continuous wave deposition of thin fluorocarbon films from saturated fluorocarbon/H₂ ICP rf plasmas. Measurements were performed in 300 mTorr discharges for peak power of 300 W at 13.56 MHz. They reported significant differences in film chemistry and deposition rates between pulsed and CW systems. The pulsed films were dominated by CF₂ groups, while the continuous wave films were completely amorphous with multiple CF_x species throughout the film. Film properties such as cross-linking and percentage of CF₂ groups deposited are dependent on the duty cycle and the relative on and off times because the production and consumption of free radicals affecting the fluorocarbon film deposition vary with duty cycle.

1.3 Modeling of Pulsed Plasmas

Meyyappan²⁰ investigated plasma characteristics of pulse-time modulated high plasma density chlorine and CF₄ discharges using a spatially averaged model. The simulations were performed at a pressure of 3 mTorr. The peak rf power was 1200 W modulated at 10 kHz with duty cycle of 25%. The model predicted negligible rates of electron impact reactions during the off part of the cycle. The plasma density increased significantly at duty ratios less than 50% for periods of 25-100 μs and electron temperature rose and fell very sharply during pulsing. In CF₄, the ratio of CF₂/F was enhanced by pulsing as a result of modulation of low threshold energy reactions. In CF₄ plasmas, electrons in after glow showed an enhanced decay rate due to the presence of

negative ions.²⁴ Ashida et al.²¹⁻²³ also investigated pulsed high plasma density, low-pressure plasmas using global models. They performed studies in argon and chlorine plasmas at a pressure of 5 mTorr. In their simulations, they used a time averaged power of 500 W varied with a duty cycle of 25% and modulation period varying from 10 μ s to 1ms. Their model predicted similar results to those of the model developed by Meyyappan²⁰. The time average electron density can be considerably higher than that for a continuous wave discharge for the same time average power. For a duty cycle of 25%, the highest plasma density was more than twice the density of the continuous wave plasma.

Lymberopoulos et al.²⁴ developed a one-dimensional (1-D) fluid model to investigate spatiotemporal dynamics of pulsed power ICP argon plasma at 10 mTorr. The simulations were performed with an absorbed power of 750 W/m² varied at 2-100 kHz with a duty cycle of 25%. The model predicts generation of superthermal electrons by metastable reactions affecting the time scale of plasma potential decay in the afterglow. They particularly studied extraction and acceleration of positive ions by a rf bias applied in the afterglow stage of the pulsed discharge. Application of rf bias resulted in modification of sheaths near walls and in particle fluxes to the plasma boundaries. In the positive part of the rf bias more negative ions reached the walls, while during the negative part of the bias more positive ions reached the walls, thus reducing charge buildup. Midha et al.²⁵ computationally studied pulsed chlorine plasmas by varying pressures, powers, pulse repetition frequencies, and duty cycles. The base conditions for the simulation were a pressure of 20 mTorr, power density of 1 W/cm³, pulse period of 100 μ s, and duty cycle of 50%. Simulation results showed a spontaneous separation of

the plasma into an ion-ion core and a electron-ion edge during the power-on fraction of the cycle. A transition from electron dominated plasma to ion-ion plasma was observed at power-off. They observed that the formation of ion-ion plasma is favored at lower power levels, higher pressures, and lower duty cycles.

Boswell et al.^{26, 27} developed a particle-in-cell (PIC) model with non periodic boundary conditions, including ionization and ion motion, to simulate pulsed electropositive and electronegative plasmas. The simulations were performed at pressure of 20 mTorr. The applied rf voltage was 1 kV with a period of 20 μ s and duty cycle of 50%. The model suggested that plasmas pulsed at around 1 kHz would reduce the lifetime of negative ions, thereby reducing the possibility of particulate growth. In electropositive plasmas, plasma density is four times lower but reduces faster when compared to electronegative discharges.

Yokozawa et al.²⁸ performed simulation of ECRs by assuming an axially symmetric three-dimensional system. The behavior of electrons, positive and negative ions during pulsing in C_2 plasma was successfully simulated at a pressure of 2 mTorr with a peak power of 500 W modulated at 10 kHz and with duty cycle of 50%. The model predicted a larger flux of Cl^- ions to the surface during the off period of the pulse, which resulted in higher etching rates. Yasaka et al.¹⁵ developed a two-dimensional (2-D) fluid simulation of ECRs to obtain spatial and temporal evolution of plasmas and radical species for deposition of poly-Si films using an $\text{Ar}/\text{H}_2/\text{SiH}_4$ mixture. The simulations were performed at a pressure of 1 mTorr. The peak microwave power was 200 W with a frequency of 5 kHz and duty cycle of 50%. The simulation qualitatively reproduced the differences

between continuous and pulsed discharges such as higher electron temperature and enhanced selectivity of SiH_3 in pulsed discharges.

Mostaghimi et al.²⁹ developed a 2-D axisymmetric model to study the response of rf ICP in an Ar/H₂ mixture to a sudden change in its active power at around atmospheric pressure conditions. The simulations were performed at pressures between 200 Torr and 760 Torr with peak power of 20 kW and pulse off time of 35 ms. The effects of discharge pressure, frequency, torch diameter, and flow rate on the response of the ICP were investigated. Response time of the plasma to the pulsing was dependent on the position in the reactor. The fastest response as well as the largest change in variables, was in the skin-depth region, where the power is dissipated.

1.4 Conclusions

There have been few modeling efforts to investigate pulsed modulated, high plasma density, low pressure ICPs. Experimental efforts to characterize plasma properties in pulsed plasmas have been successful. Global and 1-D models are inadequate to study the effect of pulsed plasmas in producing highly selective, highly anisotropic, and highly uniform etching. To characterize pulsed plasmas more accurately, better 2-D plasma models need to be developed.

In the present study a 2-D hybrid model was developed employing moderate parallelism to parallelize the Hybrid Plasma Equipment Model (HPEM). The spatiotemporal dynamics of plasma characteristics such as electron density, electron temperature, and plasma potential are investigated. The simulations are performed for a Gaseous Electronics Conference Reference Cell (GECRC) modified to include an

inductive coil. A schematic diagram of the reactor assembly used is shown in Fig. 1.1. The antenna is a five-turn planar coil that couples to the plasma through a quartz window. The reactor has a radius of 12.5 cm and a height of 11.6 cm. The top assembly of the source is installed in a modified 3.37 cm flange that mates to the reference cell chamber. The gap between the quartz window and the lower electrode is 4.05 cm. The lower electrode extension is 16.5 cm in diameter. It is a disk that rests on top of the standard lower electrode. Bias can be applied to the lower electrode. This reactor system is similar to the configuration developed by Miller et al.³⁰

The model is described in Chapter 2. Simulations were performed for both electropositive (argon) and electronegative [Ar/Cl₂ (80%/20%)] discharges, and the results are presented in Chapters 3 and 4. The extraction and acceleration of negative ions to surfaces is discussed in Chapter 4. The effects of pulse period, duty cycle and pressure on the plasma characteristics are also studied. The 2-D spatial dynamics are presented and analyzed to understand long term transients in pulsed plasmas.

A parametric study is performed by varying duty cycle, power, pressure, and pulse repetition frequency. The duty cycles were varied from 10% to 70% to study the effect of duty cycle on the 2-D evolution of electron density, plasma potential, and ion fluxes. It is observed that at lower duty cycles, the peak plasma potential is higher. The peak input power was varied between 300 W and 165 W. The electron density is observed to scale linearly with power. The pulse repetition frequency was varied from 5 kHz to 20 kHz. A higher average electron density was observed at higher pulse repetition frequencies. The pressures were varied between 10 mTorr and 20 mTorr. It is observed that higher pressures result in lower electron temperature. In the present study, the 2-D

temporal dynamics of fluxes and plasma potential are analyzed. The effect of the spatial distribution of plasma potential on the ion fluxes is also investigated.

The simulated results compare favorably with published experimental results^{9, 11}, indicating that the model correctly captures the physics. The computational consistency of the model is established as for a steady state simulation, both serial and parallel hybrid models give the same results. The model can be extended to study pulsed ECR plasmas. With moderate parallelism, attempts can be made to interface equipment-scale models and feature-scale models so that various challenging issues in etching fine features in pulsed plasmas can be adequately modeled.

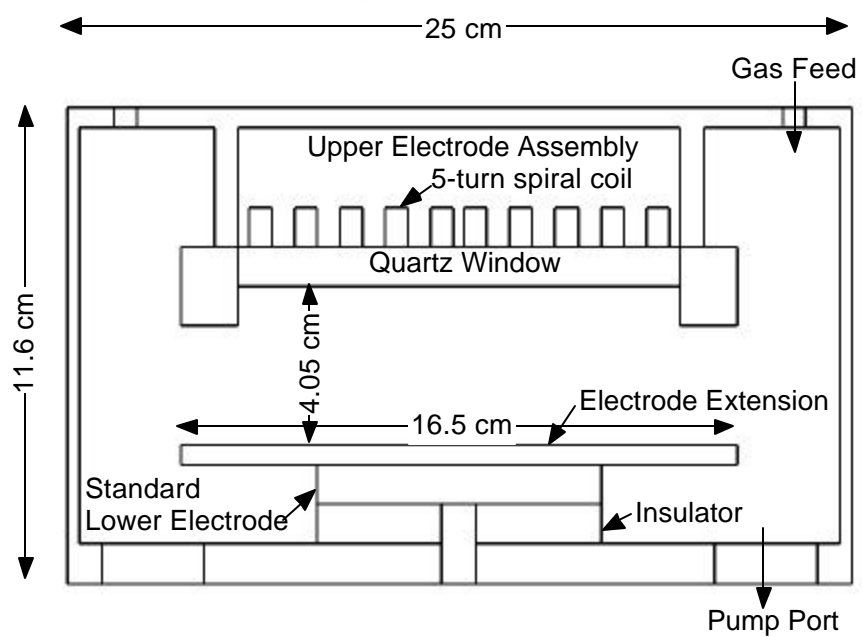


Figure 1.1 Schematic of the GEC Reference Cell Reactor

1.5 References

1. R. W. Boswell and R. K. Porteous, *J. Appl. Phys.* **62**, 3123 (1987)
2. S. Samukawa, *Jpn. J. Appl. Phys. Part 1* **32**, 6080 (1993)
3. S. Samukawa and K. Terada, *J. Vac. Sci. Technol. B* **12**, 3300 (1994)
4. S. Samukawa, *Jpn. J. Appl. Phys. Part 1* **33**, 2133 (1994)
5. S. Samukawa and T. Meino, *Plasma Sources Sci. Technol.* **5**, 132 (1996)
6. S. Samukawa and H. Ohtake, *J. Vac. Sci. Technol. A* **14**, 3049 (1996)
7. S. Samukawa, *Appl. Phys. Lett.* **68**, 316 (1996)
8. T. Maruyama, N. Fujiwara, S. Ogino, and M. Yoneda, *Jpn. J. Appl. Phys. Part 1* **36**, 2526 (1997)
9. G. A. Hebner and C. B. Fleddermann, *J. Appl. Phys.* **82**, 2814 (1997)
10. M. V. Malyshev, V. M. Donnelly, S. Samukawa, and J. I. Colonell, *J. Appl. Phys.* **86**, 4813 (1999)
11. S. Ashida, M. R. Shim, and M. A. Lieberman, *J. Vac. Sci. Technol. A* **14**, 391 (1996)
12. T. Ishigaki, X. Fan, T. Sakuta, T. Banjo, and Y. Shibuya, *Appl. Phys. Lett.* **71**, 3787 (1997)
13. K. Takahashi, M. Hori, and T. Goto, *Jpn. J. Appl. Phys. Part 2* **34**, L1088 (1993)
14. T. Meino and S. Samukawa, *Plasma Sources Sci. Technol.* **6**, 398 (1997)
15. Y. Yasaka and K. Nishimura, *Plasma Sources Sci. Technol.* **7**, 323 (1998)
16. N. M. Mackie, N. F. Dalleska, D. G. Castner, and E. R. Fisher, *Chem. Mater.* **9**, 349 (1997)
17. L. J. Overzet, J. H. Beberman, and J. T. Verdeyen, *J. Appl. Phys.* **66**, 1622 (1989)

18. A. Kono, M. Haverlag, G. M. W. Kroesen, and F. J. de Hoog, *J. Appl. Phys.* **70**, 2939 (1991)
19. M. V. Malyshev and V. M. Donnelly, *Plasma Sources Sci. Technol.* **9**, 353 (2000)
20. M. Meyyappan, *J. Vac. Sci. Technol. A* **14**, 2122 (1996)
21. S. Ashida, C. Lee, and M. A. Lieberman, *J. Vac. Sci. Technol. A* **13**, 2498 (1995)
22. M. A. Liebermann and S. Ashida, *Plasma Sources Sci. Technol.* **5**, 145 (1996)
23. S. Ashida and M. A. Liebermann, *Jpn. J. Appl. Phys. Part 1* **36**, 854 (1997)
24. D. P. Lymberopoulos, V. I. Kolobov, D. J. Economou, *J. Vac. Sci. Technol. A* **16**, 564 (1998)
25. V. Midha and D. J. Economou, *Plasma Sources Sci. Technol.* **9**, 256 (2000)
26. R. W. Boswell and D. Vender, *IEEE Trans. Plasma. Sci.* **19**, 141 (1991)
27. D. Vender, H. B. Smith, and R. W. Boswell, *J. Appl. Phys.* **80**, 4292 (1996)
28. A. Yokozawa, H. Ohtake, and S. Samukawa, *Jpn. J. Appl. Phys. Part 1* **35**, 2433 (1996)
29. J. Mostaghimi, K. C. Paul, and T. Sakuta, *J. Appl. Phys.* **83**, 1898 (1998)
30. P. A. Miller, G. A. Hebner, K. E. Greenberg, and P. D. Pochan, *J. Res. Natl. Inst. Stand. Technol.* **100**, 427 (1995)

2. DESCRIPTION OF THE MODEL

2.1 Introduction

In this chapter, the Hybrid Plasma Equipment Model (HPEM) is described. The implementation of the parallel hybrid model (HPEM-P) is discussed in Section 2.6. The validity of the model with respect to both numerics and physics is also discussed. The performance evaluation of the HPEM-P showed that nearly linear speedup is obtained.

2.2 Hybrid Plasma Equipment Model (HPEM)

The HPEM is a plasma equipment model developed at the University of Illinois to numerically investigate plasma processing reactors in two and three dimensions.¹⁻⁶ The HPEM has the capability of modeling complex reactor geometries and a wide variety of operating conditions. A flowchart of the HPEM is shown in Fig. 2.1. The main body of the two-dimensional HPEM consists of an Electromagnetics Module (EMM), an Electron Energy Transport Module (EETM) and a Fluid Kinetics Simulation (FKS). The EMM calculates inductively coupled electric and magnetic fields as well as static magnetic fields produced by the inductive coils and permanent magnets. The EETM spatially resolves the electron energy transport by either solving the electron energy conservation equation or using a Monte Carlo Simulation (MCS) to track the electron trajectories over many rf cycles to generate the spatially dependent electron energy distributions (EEDs). The EEDs are used to generate sources for electron impact processes and electron transport coefficients. Finally, the FKS solves the continuity, momentum and energy equations coupled with Poisson's equation to determine the spatially dependent density of charged and neutral species as well as electrostatic fields. In the sequential version of

HPEM, the interaction between the modules occurs in the following fashion. The fields produced by the EMM and the FKS are used in the EETM while EEDs produced in the EETM are used to calculate electron impact source functions for the FKS. Finally, the spatial density distributions produced by the FKS are used to calculate the conductivity for the EMM. These modules are iterated until a converged solution is obtained. The HPEM has numerous other modules that are described in greater detail elsewhere.¹⁻⁶

2.3 The Electromagnetics Module (EMM)

The Electromagnetics Module produces the azimuthal electric fields and r-z magnetic fields due to the inductively coupled coils and the radial and axial magnetic fields due to permanent magnets or dc coils. To determine the time harmonic azimuthal electric fields, Maxwell's equation are solved under time harmonic conditions:

$$-\nabla \cdot \frac{1}{\mathbf{m}} \nabla E_f = \omega^2 \mathbf{e} E_f - j \omega J_f \quad (2.1)$$

where \mathbf{m} is the permeability, \mathbf{e} is the permittivity, ω is the driving frequency, and the current J_f is the sum of the driving current J_o and the conduction current in the plasma. The conduction current is assumed to be of the form $J_f = \mathbf{S} E_f$. At pressures where the electrons are sufficiently collisional, the conductivity of the plasma is

$$\mathbf{S} = \frac{q_e^2 n_e}{m_e} \frac{1}{\mathbf{n}_{me} + i \omega} \quad (2.2)$$

where q is the charge, n_e is the electron density, m is the mass, and \mathbf{n}_n is the momentum transfer collision frequency. The azimuthal electric field solution is determined by the iterative method of successive overrelaxation (SOR) where convergence is assumed when the relative change is less than 10^{-6} .

The static magnetic fields in the axial and radial directions are also determined in the EMM. Assuming azimuthal symmetry allows the magnetic field to be represented by a vector potential \mathbf{A} with only an azimuthal component. \mathbf{A} can be solved using

$$\nabla \times \frac{1}{\mu} \nabla \times \mathbf{A} = \mathbf{j}, \quad \mathbf{B} = \nabla \times \mathbf{A} \quad (2.3)$$

where j is the source term due to closed current loops at mesh points representing permanent magnets or dc coils. This equation is also solved using SOR.

The coil, its power supply and its matching network are represented by solving an equivalent circuit model for the coil and matchbox to provide coil currents and voltages. The coil currents are used as the driving current boundary conditions in the EMM, and the voltages are used as boundary conditions in the solution of Poisson's equation in the FKS. The circuit model varies the matchbox capacitor values (parallel and series) to minimize the reflected power from the plasma. At the same time, the generator voltage is adjusted to deliver the desired inductively coupled power to the plasma.

2.4 The Electron Energy Transport Module (EETM)

The EETM solves for electron impact sources and electron transport properties by using electric and magnetic fields computed in the EMM and FKS. There are two methods for determining these parameters. The first method determines the electron temperature by solving the electron energy conservation equation in the electron energy equation module (EEEM). The second method uses a Monte Carlo Simulation to launch electron particles and collect statistics to generate spatial EEDs.

The EEEM solves the zero-dimensional Boltzmann equation for a range of E/N , electric field divided by plasma density, to tabulate the EEDs over this range and allow

the determination of electron transport properties. This information is used in the solution of the electron energy equation

$$\nabla k \nabla T_e + \nabla \cdot (\Gamma T_e) = P_{heating} - P_{loss} \quad (2.4)$$

where k is the thermal conductivity, \mathbf{G} is the electron flux determined by the FKS, T_e is the electron temperature equal to three halves the average energy determined from the EEDs, and $P_{heating}$ is the power added due to conductive heating equal to $\mathbf{SE} \cdot \mathbf{E}$. The conductivity is determined in the FKS. The electric field is the sum of the azimuthal field from the EMM and the radial and axial field found in the FKS. The P_{loss} is the power loss due to collisions by the electrons.

The second method for determining electron transport properties is the Electron Monte Carlo Simulation (EMCS). The EMCS simulates electron trajectories according to local electric and magnetic fields and collision processes. Initially the electrons are given a Maxwellian distribution and are randomly distributed in the reactor weighted by the current electron density. Particle trajectories are computed using the Lorentz equation:

$$\frac{d\bar{\mathbf{v}}}{dt} = \frac{q_e}{m_e} (\bar{\mathbf{E}} + \bar{\mathbf{v}} \times \bar{\mathbf{B}}) \quad (2.5)$$

and

$$\frac{d\bar{\mathbf{r}}}{dt} = \bar{\mathbf{v}} \quad (2.6)$$

where $\bar{\mathbf{v}}$, $\bar{\mathbf{E}}$, and $\bar{\mathbf{B}}$ are the electron velocity, local electric field, and magnetic field respectively. Equations (2.5) and (2.6) are updated using a second-order predictor corrector method. The electron energy range is divided into discrete energy bins. Within an energy bin, the collision frequency ν_i , is computed by summing all the possible collisions within the energy range:

$$\mathbf{n}_i = \left(\frac{2\epsilon_i}{m_e} \right)^{\frac{1}{2}} \sum_{j,k} \sigma_{ijk} N_j \quad (2.7)$$

where ϵ_i is the average energy within the bin, σ_{ijk} is the cross section at energy i , for species j and collision process k , and N_j is the number density of species j . The free-flight time is randomly determined from the maximum collision frequency. After the free-flight, the type of collision is determined by the energy of the pseudoparticle. The corresponding energy bin is referenced and a collision is randomly selected from that energy bin, with a null reaction making up the difference between the maximum and actual collision frequencies. Finally, the electron temperature, collision frequency, and electron impact rate coefficients are evaluated based on EEDs with the process cross section at the specified location.

2.5 The Fluid Kinetics Simulation (FKS)

The FKS solves the fluid transport equations to provide species densities and fluxes and temperature. The module also includes chemical reactions and a solution of Poisson's equation or an ambipolar field solution for the electric potential and time-dependent electrostatic fields. Electron transport coefficients and electron impact rates needed to solve the fluid and potential equations are obtained from the EETM. Ion and neutral transport coefficients are obtained from a database or by using Lenard-Jones parameters. The species densities are calculated from the continuity equation:

$$\frac{\partial N_i}{\partial t} = -\nabla \cdot \Gamma_i + S_i \quad (2.8)$$

where N_i , Γ_i , and S_i are the species density, flux, and source for species i . The flux for each species can be determined by using a drift diffusion or a heavy body momentum equation. Electron densities are determined using the drift diffusion formulation,

$$\Gamma_i = \mu_i N_i \bar{E}_s - D_i \nabla N_i \quad (2.9)$$

where μ_i is the mobility of species i , D_i is the diffusion coefficient, q_i is the species charge in units of elementary charge, and E_s is the electrostatic field. Heavy ion and neutral fluxes can be determined by using the previous drift diffusion method or by using the heavy body momentum equation:

$$\frac{\partial \Gamma_i}{\partial t} = -\frac{1}{m_i} \nabla(N_i k T_i) - \nabla \cdot (N_i \bar{v}_i \bar{v}_i) + \frac{q_i}{m_i} N_i \bar{E} - \sum_j \frac{m_j}{m_i + m_j} N_i N_j (\bar{v}_i - \bar{v}_j) \nu_{ij} \quad (2.10)$$

where T_i is the species temperature, \bar{v}_i is the species velocity given by Γ_i / N_i , and ν_{ij} is the collision frequency between species i and species j .

The gas and ion temperatures are determined from the energy equation for each species:

$$\begin{aligned} \nabla \cdot (\kappa_i \hat{e}_i \nabla T_i) - P_i \nabla \cdot \bar{v}_i - \nabla \cdot (\bar{\mathbf{j}}_i \hat{\mathbf{a}}_i) + \frac{N_i q_i^2}{m_i \nu_i} E_s^2 + \frac{N_i q_i^2 \nu_i}{m_i (\nu_i^2 + \omega_i^2)} E^2 \\ + \sum_j 3 \frac{m_{ij}}{m_i + m_j} N_i N_j R_{ij} k (T_j - T_i) \end{aligned} \quad (2.11)$$

where N_i is the density of species i , c_v is specific heat, T_i is the species temperature, κ_i is the thermal conductivity of species i , P_i is the partial pressure of species i , \bar{v}_i is the species velocity, $\bar{\mathbf{j}}_i$ is the flux of species i , $\hat{\mathbf{a}}_i$ is the internal energy of species i , E_s is the electrostatic field, E is the rf field, m_i is the mass of species i , m_{ij} is the reduced mass, ν_i is the momentum transfer collision frequency for species i , and R_{ij} is the collision frequency for the collision process between species i and j .

Solutions to Equations (2.9)-(2.11) require knowledge of the local electrostatic fields. Electrostatic fields can be determined in two ways. The first method solves Poisson's equation for the electric potential. Using the drift diffusion equation, (2.9), an implicit form of Poisson's is

$$\nabla \cdot \left(\left(\mathbf{e} - \Delta t \boldsymbol{\sigma} + \Delta t \sum_i q_i^2 \mu_i N_i \right) \nabla \phi^{t+\Delta t} \right) = -\mathbf{r}^t + \Delta t \nabla \cdot \left(\sum_i q_i D_i \nabla N_i^t - \sum_j q_j \Gamma_j^t \right) \quad (2.12)$$

where $\boldsymbol{\sigma}$ is the material conductivity and is nonzero only outside of the plasma region, e is elemental charge; q_i , μ_i , N_i , and Γ_i are the charge state, mobility, density, and the flux of species i at time t , respectively; Γ_j is the flux for species j at time t ; and $\phi^{t+\Delta t}$ is the electric potential at time $t + \Delta t$. The summations over i are taken for those species using the drift diffusion formulation, and the summation over j is taken for those species using the momentum equation. Equation (2.12) is a modified form of Poisson's equation and is solved using the successive over relaxation (SOR) method. The time step taken in the charged-particle update requires that the fields donot reverse in a single time step. This is known as the dielectric relaxation time. It can be interpreted as the Courant limit on Poisson's equation. The implicit method described here allows the time steps to be larger than the dielectric relaxation time.

The second method for determining the electric potential uses an ambipolar approximation. Using this assumption, the electron density is computed assuming that the plasma is quasi-neutral at all points. The flux conservation equation can be written, after substituting the drift diffusion formulation, as

$$\sum_i q_i \nabla \cdot (q_i n_i \mu_i \nabla \phi - D_i \nabla n_i) = \sum_i q_i S_i \quad (2.13)$$

where S_i is the electron source function. Equation (2.13) can be rewritten to give Poisson-like equation for the electrostatic potential:

$$\nabla \cdot \left(\sum_i q_i^2 n_i \mathbf{m} \nabla \mathbf{f} \right) = \sum_i (q_i D_i \nabla n_i) + \sum_i q_i S_i \quad (2.14)$$

where the summation is now taken over all the charged species, including electrons. This Poisson-like equation is discretized and solved using a SOR method. By solving for the electrostatic potential using the ambipolar approximation, the time step is only limited by the Courant limit.

2.6 Parallel HPEM

As described in Sections 2.3-2.5, HPEM is set up to address disparate time scales separately. In the existing setup, HPEM employs a modular approach consisting primarily of three main modules to address disparate time scales individually. Currently, HPEM consists of a series of quasi-independent modules for electron, ion, and neutral transport; electromagnetics; plasma surface interactions; and electrical circuitry. These modules are designed to exchange required input and generated outputs in an independent fashion. As a result there is a lag in time for the information used by different modules to evaluate plasma properties. This is a hindrance when long term transients are to be addressed. The serial HPEM efficiently addresses disparate time scales in plasma simulations. In each iteration, the time spent in the EMM is much shorter than the time required to perform the EMCS in the EETM. This time is in turn significantly lower than the time taken to execute the FKS if the number of particles in the EMCS is small.

Since the time scales in plasma simulations are so disparate, it is our working premise that some type of hybrid scheme is required to model transients. A strategy to address issues of modeling transients is to employ moderate "task parallelism".

The most common parallel programming paradigms are shared-memory programming, message-passing programming, and array programming. Moderate parallelism with shared memory is the preferred method for parallelizing the HPEM. Task parallelism can be implemented using OpenMP compiler directives available for shared memory parallel programming. This programming style was adapted for parallelizing HPEM, referred to as HPEM-P.

OpenMP is a collection of compiler directives, library routines, and environment variables that can be used to specify shared memory parallelism. An OpenMP program begins execution as a single task, called the master thread. When a parallel construct is encountered, the master thread creates a team of threads. The statements enclosed by the parallel construct, including routines called from within the enclosed construct, are executed in parallel by each thread in the team. At the end of the parallel construct the threads in the team synchronize, and only the master thread continues execution. All variables are shared by all tasks executing the parallel region unless otherwise specified.

The task parallelism is implemented using the PSECTIONS compiler directive provided by the Kuck and Associates (KAI) implementation⁷ of OpenMP. Parallelism is specified to execute the EMM, EETM, and FKS of the HPEM-P in parallel as different tasks on three different processors of a symmetric multi processor computer with shared memory. HPEM-P starts execution as a single thread. The single thread initializes all variables and accesses the required reaction data and geometry information for the

plasma processing reactor, as was done previously in the serial HPEM. In each iteration of HPEM-P, the single thread generates three tasks by an explicit spawning technique. Explicit spawning is implemented using PSECTIONS compiler directives by which the individual tasks of each processor are explicitly specified by the programmer. The three tasks are to execute the EMM, EETM, and FKS simultaneously by three different threads.

HPEM-P is not a sequentially equivalent version as it allows the individual modules to use the most recent values of plasma parameters and does not require strict order of the access and update of the shared variables. This type of unordered update is not desired in many of the parallel applications, but is a desired feature in the HPEM-P. The objective in the HPEM-P is to make the most recent values of plasma parameters available for different modules whenever they are required. Hence, the variable updates need not be ordered as in the sequential execution. Only synchronization of the variable updates need to be performed so as to avoid race conditions arising from a module accessing a variable while it is being updated by another module.

The updates of a variable and the accessing of a variable have to be synchronized to avoid race conditions. Race conditions arise when there are two memory references taking place in two different tasks which are not ordered, and the references are to the same memory location and one of them is a memory write. In HPEM-P, race conditions are eliminated by the CRITICAL synchronization compiler directive in OpenMP. The critical directive defines the scope of a critical section. Only one thread is allowed inside the critical section at a time. The name of the critical section has global scope. Two critical directives with the same name are mutually exclusive. This means that if a thread

is executing a critical section with a particular name, then any other thread trying to execute the critical section with the same name has to wait until the thread currently executing the critical section exits. This synchronization is performed for all the variables shared between the EMM, EETM, and FKS.

When performing parallelization, one must perform data dependency analysis to establish flow dependence, antidependence, and output dependence in the sequential version of the code. All these dependencies are potentially dangerous and must be eliminated for the parallel execution to be race free. In HPEM all these dependencies are encountered as variables are updated and accessed frequently by the three modules. The dependencies in HPEM are eliminated by using critical sections, so that only one operation is performed at a time among the dependent operations. Thus, the dependent operations are synchronized to eliminate any dependencies.

2.6.1 Variables: shared or private

In the sequential HPEM, Maxwell's equations provide steady state solutions and hence need to be solved only once every iteration in the EMM. While investigating transients, these sequential updates cannot capture the physics because there is loss of information between iterations. The HPEM-P solves this problem by updating the plasma conductivity and collision frequency continuously during the FKS. The flow of information in the parallel hybrid model is shown in Fig. 2.2. These updated parameters are made available in shared memory to be accessed by the EMM to enable continuous updates of the electromagnetic fields. The EMM module is executed several times in an iteration whenever an update of plasma conductivity is obtained from the FKS as

opposed to only once in the serial version of HPEM. More frequent updates of the electromagnetic and magnetostatic fields are made available in EETM for the update of electron impact source functions and transport coefficients.

The electron impact source functions and transport coefficients are obtained in the EETM using the electromagnetic fields from the EMM, and the densities, ambipolar electric fields, and fluxes from the FKS. In the sequential HPEM, sources and transport coefficients are updated only at the end of the EETM. In HPEM-P these variables are more frequently updated. The sources and transport coefficients are in turn used in the FKS to compute densities, fluxes and fields which are required in the EETM, and to compute plasma conductivity and electron collision frequency needed in the EMM. The information needed in different modules is readily made available "on the fly". All the other variables are private and are accessed only within the individual modules. Thus, there is a very tightly knit exchange of information among the three modules. Each task is dependent on information from the other two tasks to update its variables. Thus, it is not required to impose any order on the updates because such an attempt will make the execution sequential, which is not desired. The employed numerical technique enables the EMM, EETM, and FKS to execute in truly parallel mode without necessarily waiting for other modules to complete their tasks.

2.6.2 Dynamic load balancing

Implementation of dynamic load balancing is required to make the HPEM-P more efficient. Since the three modules execute for disparate times, it is desirable to balance the time spent in each module and so ensure that the processors are not idle for a

significant amount of time. The bottleneck in these simulations is typically the FKS module. The EMM typically takes the least time. Electromagnetic fields are required only in the EETM, so the EMM needs to be executed only until the EETM is complete. Therefore a dynamic load balancing strategy is adopted to equalize the time for each task.

First, the time in the MCS is dynamically adjusted between iterations to make the execution time of the EETM nearly the same as the FKS. If the FKS takes a longer time to execute than the EETM, then the time in the MCS is reduced, and vice versa. The time in the MCS is initially just enough to obtain acceptable statistics. Then the time in the MCS is adjusted by changing the time for integrating electron trajectories. By tracking which processor completes the task first in the current iteration, the time in the MCS for the next iteration is correspondingly set. The imbalance between the EETM and the FKS was reduced to a large extent by the load balancing. However, there is a minimum amount of time that needs to be spent in the MCS to generate acceptable statistics. If the time spent in the EETM is more than the time spent in the FKS, then the number of particles in the MCS can be decreased so as to decrease the time in the EETM. For almost all simulations the time initially spent in the FKS is significantly greater than the time in the EETM. Hence, by adopting this strategy, time in the FKS and the EETM can be made nearly equal.

Next, the execution times in the EETM and the EMM were made nearly equal. This was achieved by executing the EMM several times in an iteration. The EMM generates fields which are used in the MCS. Hence, the strategy adopted is to execute the EMM until the EETM is completed in each iteration. The load balancing between the EMM and the EETM was effective, as shown in Fig. 2.4.

Dynamic load balancing increases the tasks of individual processors when compared to a sequential execution of HPEM. This increase in problem size is desired because as the time spent in the MCS increases, better statistics are obtained. Similarly when investigating transients, the EMM needs to be executed several times in an iteration to update the electromagnetic fields more frequently so as to capture the transients accurately.

The simulation time in different modules as the problem size is increased is shown in Fig. 2.3. The problem size is increased by either increasing the number of particles in the EMCS or by increasing the mesh size. As the problem size increases, the disparity between the time spent in each module increases and hence dynamic load balancing becomes essential. The change in execution time with and without dynamic load balancing is shown in Fig. 2.4. With dynamic load balancing, the load on the processor executing the EMM and the EETM is increased to match the load on the processor executing the FKS. Thus all three processors execute for nearly the same period of time decreasing the load imbalances.

2.6.3 Validation of the parallel hybrid model

The parallel implementation is not a sequentially equivalent implementation of the HPEM. However, it is a numerically consistent implementation. HPEM-P was validated by comparing the sequential and parallel results for steady state simulations. To validate the model, a typical simulation is performed in a GEC reference cell with Ar gas feed. The simulation was carried out for 100 iterations at a pressure of 20 mTorr. The peak input power was 300 W and the flow rate was 20 sccm. As shown in Fig. 2.5, the

spatial electron density distributions for serial and parallel simulations of a steady state case are similar. The electron density estimation by HPEM-P was 3-5% higher than the electron density estimation by the serial HPEM. This disparity is due to the difference in the numerical strategies of HPEM-P and HPEM. The spatial distribution of plasma potential for the serial and parallel simulation is shown in Fig. 2.6. The temporal evolution of electron temperature for the serial and parallel simulations is shown in Fig. 2.7. A detailed comparison of the experimental and simulation results will be discussed in Chapter 3 for Ar gas feed.

2.6.4 Performance evaluation

Though not the primary concern of this thesis, the improvement in computer performance obtained with the HPEM-P is promising. A speedup of 2.8 is typically achieved on a three processor SUN Microsystems 400 MHz workstation. In every iteration of the sequential HPEM, the EMM, the EETM, and the FKS are executed only once. The time in the EETM is also kept constant in the serial HPEM. However, in the HPEM-P, the EMM is executed several times and the time in the EETM is typically increased to equal the execution time of the FKS. When serial HPEM took about 12 hrs for completing a simulation, the HPEM-P took only 9.5 hrs to execute the larger task.

The speedup of 2.8 is a nearly linear speedup on a three processor multi computer. In the current implementation of HPEM-P, only a linear speedup was expected. This may be attributed to the bottleneck in these simulations, which is the FKS module. Hence, at best simulation time can be reduced to the time required to execute the FKS module. This then means a speedup lower than 2.8. However, since the EMM and the EETM are

executed for the same amount of time as the FKS in HPEM-P, the problem size is increased. Since the three tasks, namely, the EMM, EETM and FKS, are executed together in the same amount of time as the FKS, the speedup of 2.8 can be achieved. The speedup is below the expected value of 3, as in each iteration there is some sequential execution for post processing, some amount of time spent in acquiring locks, and some imbalance as one processor waits for the rest of the processors to complete their tasks. This may be also due to the parallel overhead involved in creating threads at the beginning of each iteration. With all these limitations, the speedup of 2.8 is encouraging.

2.7 Conclusions

The proposed method for addressing transients based on moderate parallelism interfaces the short scale plasma time scales with the long term neutral time scales. Plasma transport, neutral fluid transport, and electromagnetics are simultaneously computed on separate processors. Fluid conditions (e.g., changes in pressure, mole fractions, and flow fields) which are slowly evolving over time are made available to the simultaneous calculation of plasma properties (e.g., electron and ion density, electrostatic fields) through shared memory. The plasma properties will therefore “track” (in an almost adiabatic sense) the more slowly varying fluid properties while continually updating electron impact sources.

Thus, moderate parallelism takes the hybrid approach from using quasi-steady-state serial updates to using real-time-simultaneous updates and hence becoming truly capable of addressing long term transients.

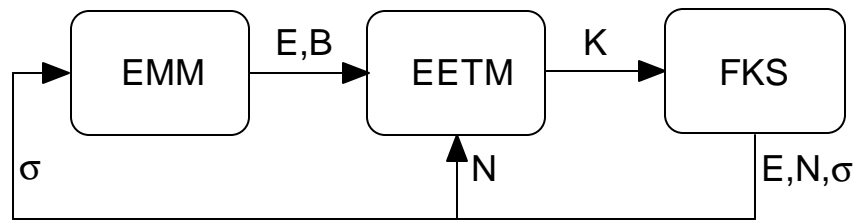


Figure 2.1 Schematic of the main body of the 2-D Hybrid Plasma Equipment Model (HPEM).

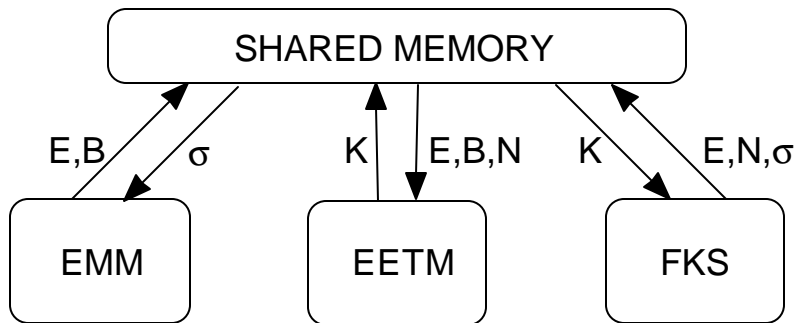


Figure 2.2 Schematic of 2-D parallel HPEM (HPEM-P).

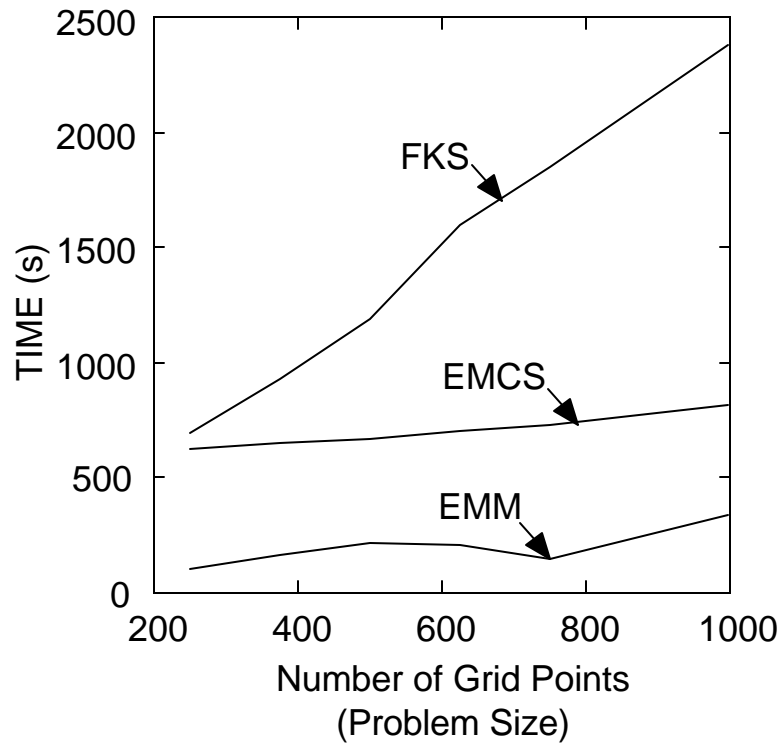


Figure 2.3 Plot of time spent in each module for 100 iterations for a steady state case versus the problem size.

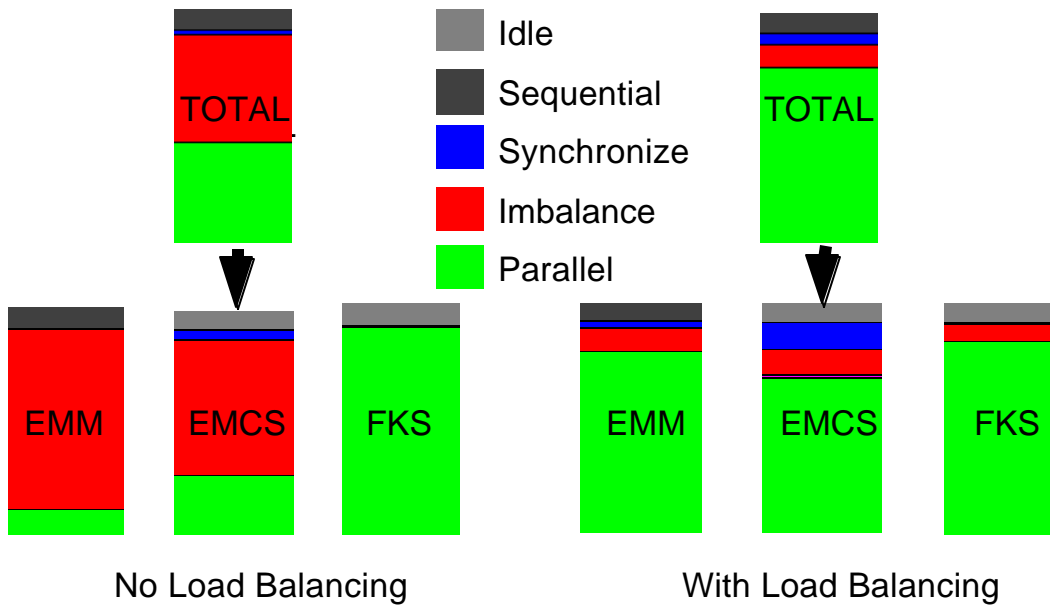
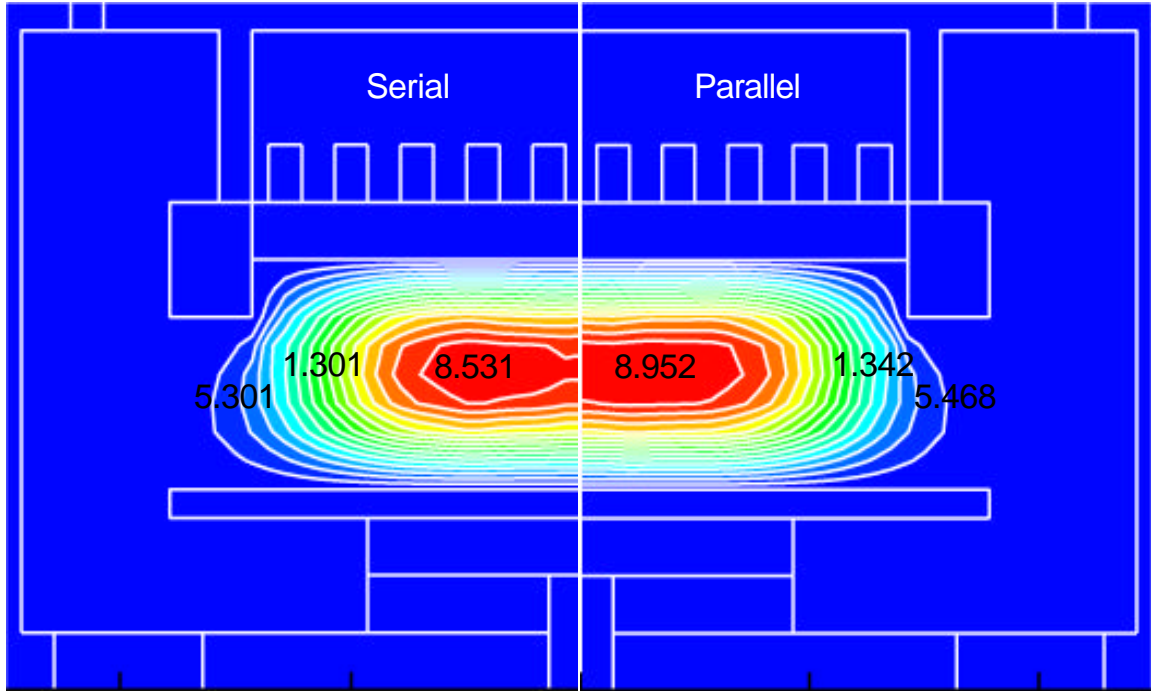
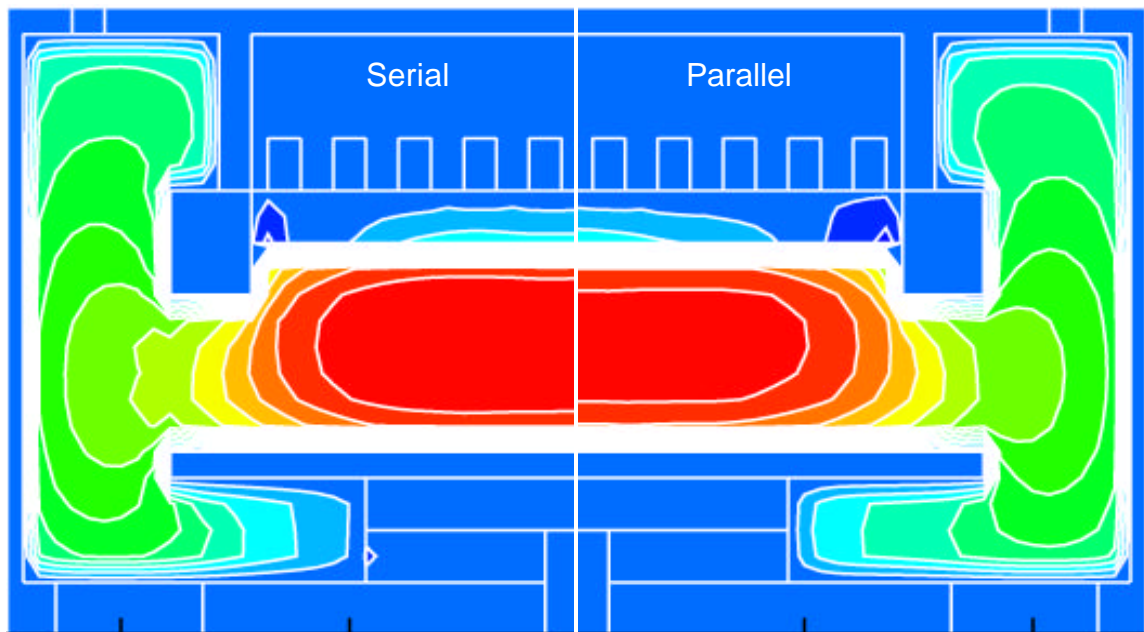


Figure 2.4 Comparison of CPU times for 100 iterations of a steady state case with and without dynamic load balancing.



$5 \times 10^{10} \text{ cm}^{-3}$  $8 \times 10^{11} \text{ cm}^{-3}$

Figure 2.5 Comparison of 2-D electron density for serial and parallel simulations for a steady state case.



-2 V  23 V

Figure 2.6 Comparison of 2-D plasma potential for serial and parallel simulations for a steady state case.

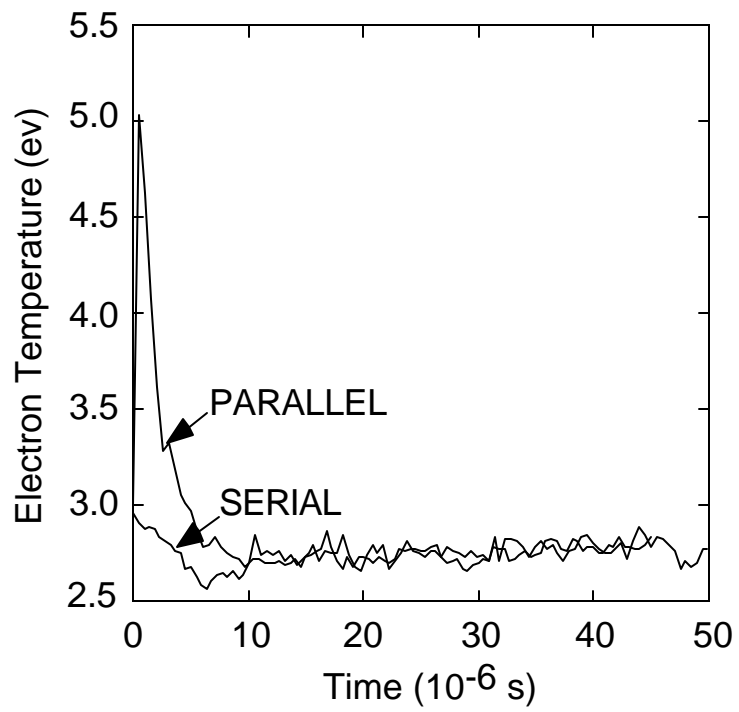


Figure 2.7 Comparison of the temporal evolution of electron temperature for serial and parallel simulations for a steady state case.

2.8 References

1. P. L. G. Ventzek, R. J. Hoekstra, and M. J. Kushner, *J. Vac. Sci. Technol. B* **12**, 416 (1993)
2. P. L. G. Ventzek, M. Grapperhaus, and M. J. Kushner, *J. Vac. Sci. Technol. B* **16**, 3118 (1994)
3. W. Z. Collison and M. J. Kushner, *Appl. Phys. Lett.* **68**, 903 (1996)
4. M. J. Kushner, W. Z. Collison, M. J. Grapperhaus, J. P. Holland, and M. S. Barnes, *J. Appl. Phys.* **80**, 1337 (1996)
5. M. J. Grapperhaus and M. J. Kushner, *J. Appl. Phys.* **81**, 569 (1997)
6. S. Rauf and M. J. Kushner, *J. Appl. Phys.* **81**, 5966 (1997)
7. <http://www.kai.com/parallel/kappro/>

3. INVESTIGATIONS OF ARGON PULSED PLASMAS

3.1 Introduction

In this chapter, the results from our investigation of pulsed plasmas are presented. The investigations were performed to quantify the consequences of the duty cycle, power, pulse repetition frequency, and pressure on various plasma properties such as electron density, electron temperature, and plasma potential. A periodic steady state was attained in all the simulations by employing multiple pulses. The spatiotemporal dynamics of the plasma properties as the pulse progresses are also discussed. The simulation results show similar trends as seen in experiments.

3.2 Comparison with Experiments

To validate the model, the simulation results were compared with experiments.^{1, 2} Hebner et al.¹ had characterized pulse modulated ICPs in argon plasmas in a Gaseous Electronics Conference Reference Cell (GECRC) by measuring the time dependent electron density as a function of duty cycle, pulse repetition frequency, and power. They also reported rf plasma potential for 6 μ s of the operation when the power is turned on. The peak electron column density was obtained from simulations by integrating the electron density radially at a height of 4.8 cm from the bottom of the reactor. In the experiments, the electron column density was measured using a microwave bridge interferometer.

The simulation conditions were similar to the experiments. The comparison of the electron density for two cases of simulation with the experiment for a peak input power of 300 W, pulse repetition frequency of 10 kHz, and duty cycle of 50% is shown in

Fig. 3.1. The simulation results (case 1) show trends similar to those of experiments. The difference in the numerical values is not significant considering the uncertainties in various parameters such as reaction cross sections used in the modeling and various assumptions of the model. In the case 2 shown in Fig. 3.1, there is more of electron impact ionizations due to higher concentration of metastables. The case 2 shows better match with the experiments. Thus, with these uncertainties the model predictions are good. The comparison of peak electron column density for a peak input power of 190 W, modulated at a frequency of 10 kHz and duty cycle of 30%, is shown in Fig. 3.2. The simulation closely captures the trend, though there is some disparity in the exact numerical values.

The peak electron column density for a peak input power of 300 W, pulse repetition frequency of 20 kHz, and duty cycle of 50% is shown in Fig. 3.3. The simulation results capture the trends in electron density. The peak electron column density in experiments was $1.6 \times 10^{12} \text{ cm}^{-2}$, while the peak electron column density in simulation was $1.0 \times 10^{12} \text{ cm}^{-2}$. This disparity is due to the lower rate coefficients for the de-excitation of doubly excited metastables to singly excited metastables. For case 2 with a higher concentration of metastables, the peak electron column density was $1.4 \times 10^{12} \text{ cm}^{-2}$, which was closer to the value measured in experiments.

The decay and rise times predicted in simulations were similar to the values reported.² The experiments performed by Ashida et al.² showed decay times of 63 μs and rise times of 14 μs for plasma density for a pulse repetition frequency of 10 kHz and duty cycle of 30% in pulse modulated argon ICPs at pressure of 5 mTorr. The total absorbed power in the experiments was 120 W. The simulations predicted a rise time of 18 μs .

The decay time in simulations was greater than 70 μs as the electron density was monotonously decaying.

3.3 Base Case Conditions

Simulations were performed for conditions corresponding to a GECRC as shown in Fig. 1.1. The details of the reactor are described in Chapter 1. The base case conditions are an Ar gas pressure of 20 mTorr and peak power of 300 W, modulated at a pulse repetition frequency of 10 kHz and a duty cycle of 50%. The Ar reaction chemistry is given in Appendix A. In our study, the duty cycle was varied from 10% to 70% and the pulse repetition frequency was varied from 5 kHz to 20 kHz. The peak power was varied from 165 W to 300 W, while the pressure was varied from 10 mTorr to 20 mTorr.

Power modulation for the base case was performed as shown in Fig. 3.4. The final two pulses in a series of several pulses are shown in Fig. 3.4. For the base case, the pulse repetition frequency was 10 kHz and the duty cycle was 50%. Prior to pulsing the plasma, a quasi steady state was attained at the same average power as that obtained in pulsed operation. The plasma properties attain a quasi-steady state as shown in Fig. 3.5. The power is then turned off and on for four or more pulses in order to reach a periodic steady state. The peak input power of the base case was 300 W. It was reduced to 3×10^{-3} W over a period of 17 μs and then kept constant at this value for the rest of the off period. The power turn-off period (17 μs) was same in all the simulations. The power was turned on over a period of 5 μs and kept constant at 300 W for the rest of the on period. The peak input power was never reduced to zero as the MCS requires electric fields from the EMM to calculate the statistics for generating source functions. The strategy adopted here

was to decrease the power to a value sufficiently low that it was negligible (3×10^{-3} W). The power was turned on or off over a small period of time to avoid the convergence problems encountered in the successive over relaxation (SOR) solver used for computation of the plasma potential.

The electron density and plasma potential variation for all the pulses is as shown in Fig. 3.5. When the plasma is turned off, the electron density decays monotonously. The time scales of electron decay are based on the ion losses to the walls. For the results presented in Fig. 3.5, the time for electron decay is more than 50 μ s (the off period). Thus there is a significant amount of cold electrons in the late afterglow. However, during the pulse-on time the electron density attains a steady state corresponding to the continuous wave operation. The plasma potential shows faster dynamics than electron density. This is because the decay in plasma potential scales with the ion energy loss to the wall. When the power is turned off, the plasma potential decays to a few volts in about 15 μ s. When the power is turned on, the plasma potential peaked for a short period of time. The peak plasma potential needed to avalanche the plasma was about 1.5 times the steady state value.

3.4 Effect of Duty Cycle

Duty cycle is defined as the ratio of the on pulse period to the total period. In pulsed operation, duty cycle provides the process design engineer with an additional degree of freedom to optimize the plasma operation. The effect of duty cycle on the plasma properties is shown in Figs. 3.6 - 3.12. The duty cycle was varied from 10% to

70%, keeping the pulse repetition frequency at 10 kHz, peak input power at 300 W, and pressure at 20 mTorr.

The temporal dynamics of peak electron density are shown in Fig. 3.6 for the duty cycles of 10%, 30%, 50%, and 70. Electron density attained a steady state value at $1 \times 10^{12} \text{ cm}^{-3}$ for the duty cycles of 30%, 50%, and 70%. Electron density reached a peak of $4 \times 10^{11} \text{ cm}^{-3}$ for the duty cycle of 10%. For the 10% duty cycle, the power is not on for enough time for the plasma to attain a steady state. This is because the time required for the production of electrons by electron impact ionization reactions to equal the diffusion losses is larger than the on-pulse time. The electron density in the late afterglow was lower in the 10% case, so more on-pulse time is required to attain the steady state. Thus increasing the duty cycle resulted in a constant steady state electron density because there was enough time to establish the balance between the loss and gain of electrons. The electron density decayed monotonously after the power turn-off. As the plasma was turned off, the sources for electrons such as electron impact ionizations decrease rapidly while the ambipolar diffusion losses to the wall occur slowly. The electron density decayed to a lower value as the plasma was turned off for a longer time as in the 10% duty cycle case. The time taken for the electron density decay scales with the ion loss to the wall, and hence a lower electron density results for the lower duty cycle. The rise time for power turn-on was much smaller than the decay time as the rate of production of electrons increases rapidly at power turn-on, superseding the rate of diffusion losses.

The 2-D electron density at different instants during a pulse is shown in Fig. 3.7. When the pulse power is turned on, the electron density peaks near the inductive coil, as most of the power deposition occurs at that position as shown in Fig. 3.7(b). The power

deposition scales as the square of the electric field, and the electric field is larger near the coils. As time progresses, the source of electrons closer to the coil decreases as the electron temperature falls to the value corresponding to the continuous wave operation, and electrons diffuse out resulting in a steady state profile as shown in Fig. 3.7(c). In the early afterglow, as soon as the power is turned off, the ambipolar losses dominate over the generation of electrons. This results in a rapid decrease in the electron density as seen in Fig. 3.7(d). The ambipolar losses scale with electron temperature. The electron temperature reduces to few eV in a short period of time after the pulse is turned off. Hence, the ambipolar losses decrease as the pulse progresses, though it is still dominating over the generation of electrons. Hence, the rate of electron decay reduces in the late afterglow and a significant number of electrons exist in the plasma even in the late afterglow as seen in Fig. 3.7(e)-(f). The electron temperature reduces faster at the center, resulting in a reduced source for electrons; this results in a faster decay in electron density at the center than near the walls as seen in Fig. 3.7(d)-(f). The spatiotemporal dynamics of electron density for the other duty cycles is similar to the 50% duty cycle case. At lower duty cycles, the plasma is turned off for a longer time, resulting in a lower electron density near the walls in the late afterglow. This is because the diffusion losses were dominant for longer duration in lower duty cycle. Thus, for lower duty cycles, the plasma is more confined to the center of the reactor as shown in Fig. 3.8. This results in an enhanced diffusion at higher duty cycle, and it result in further loss of electrons.

The plasma potential and electron temperature are shown in Figs. 3.9 and 3.10 respectively. As the duty cycle decreases, the peak electron temperature and peak plasma potential increase. This is because at lower duty cycles, electron density is low in the late

afterglow; therefore a higher electron temperature is required to avalanche the plasma. The peak plasma potential was about 45 V for a duty cycle of 10%, while it was 33 V for a duty cycle of 70%. Similarly, the electron temperature peaked at around 5.8 eV for a duty cycle of 10%, but for a duty cycle of 70%, the peak electron temperature was only 4.2 eV. For higher duty cycles, the plasma potential and electron temperature attain a steady state corresponding to the continuous wave operation. The rate of electron temperature decay scales with collision frequency, and as all the simulations were at the same pressure, the collision frequencies were similar, resulting in equal decay times as seen in Fig. 3.10. The plasma potential decreased to few volts in about 20 μ s.

The 2-D plasma potential and electron temperature are shown in Figs. 3.11 and 3.12, respectively. The plasma potential peaks near the inductive coil at the power turn-on, and then the peak in potential drifts down to the center of the reactor. As the power deposition occurs mostly closer to the coil, the electron temperature is highest near the coils, causing a large source for ions. Hence, the plasma potential peaks to redistribute the ions to the bulk plasma. At the plasma turn-off, the plasma potential decreases faster at the walls than at the center of the plasma as shown in Fig. 3.11(d)-(f). This is because even when the power is turned off, there is a source of electrons in the center, and so in order to distribute the ions the plasma potential exists. The electron temperature peaks under the coil where the power deposition is a maximum, as shown in Fig. 3.12(b). As the electrons diffuse out, the electron temperature decreases to a steady state value as shown in Fig. 3.12(c). When plasma is turned off, the electric fields are larger at the periphery than at the center, causing the hot electrons to move out and resulting in a lower electron temperature in the center as seen in Fig. 3.12(d)-(f). The flux

of Ar^+ ions responds to the change in the plasma potential almost immediately. The flux of positive ions is always directed away from the peak of the plasma potential. During the plasma turn-off, the Ar^+ flux to the walls decreases, but during the plasma turn-on, a large flux of Ar^+ ions to the wall is generated. Even though this flux exists only for a few μs , it can cause device damage. As the duty cycle decreases, the flux to the walls is higher at plasma turn-on, because the peak plasma potential is higher, which is more destructive for the device. Thus varying duty cycle, the flux to the wall can be controlled, which in turn affects the etching rates and controls the charge buildup in features

3.5 Effect of Power

The electron density scales linearly with power. In the present study, the peak input power was varied from 165 W to 300 W. For a peak input power of 300 W, the peak electron density was $1 \times 10^{12} \text{ cm}^{-3}$, while for a peak input power of 190 W, the peak electron density was about $7 \times 10^{11} \text{ cm}^{-3}$. As shown in Fig. 3.13, for a duty cycle of 30%, the electron density does not attain a steady state. As the power is turned off, the electron density decays with similar decay times for different power. This is because the electron density decay depends on the ion loss to the wall, and at power turn-off the ion flux is determined by the collision frequency, which is a constant as the pressure is same. The peak electron density decayed to $1 \times 10^{11} \text{ cm}^{-3}$ as the power was turned off. The spatiotemporal dynamics in electron density were similar in all the simulations with peak input power of 165 W, 190 W, and 300 W. The electron density was higher at larger power due to increased source of electrons from electron impact ionization reactions.

The plasma potential and electron temperature did not show significant variations as the power was varied as shown in Figs. 3.14 and 3.15. The plasma potential peaked at 38 V and electron temperature at about 4.6 eV. This is because the electron density decayed to nearly the same values for different power. Hence, to avalanche the plasma from the late afterglow with nearly the same plasma density, the same peak electron temperature was only required. The electron temperature decayed to a few tenths of an electron volt in about 10 μ s at plasma turn-off. The rise time was about 4 μ s and was much shorter than the decay time. This is because the rise time is determined by the electric field, causing the acceleration of charged species, while the decay time is determined by the collision frequency.

3.6 Effect of Pulse Repetition Frequency

The pulse repetition frequency can be varied in the pulsed operation to optimize the plasma properties. By decreasing the pulse repetition frequency, the afterglow in the plasma can be sustained for a longer period. Thus, the pulse period can be adjusted to meet the process requirements such as the extent of etching and selectivity. The pulse repetition frequency is varied from 5 kHz to 20 kHz. The pulse repetition frequency significantly altered the electron density, electron temperature, and plasma potential.

The variation of electron density with pulse repetition frequency is shown in Fig. 3.16. As the pulse repetition frequency is increased, the peak electron density in the late afterglow increases. For a pulse frequency of 5 kHz, the peak electron density in the late afterglow was $1.2 \times 10^{11} \text{ cm}^{-3}$, but as the frequency was increased to 20 kHz, the peak electron density increased to $3 \times 10^{11} \text{ cm}^{-3}$. The time averaged electron density also

increased as the pulse repetition frequency increased. This is due to shorter duration of electron density decay in the after glow with the increase in pulse repetition frequency. By varying the pulse repetition frequency, process specified time averaged electron density can be maintained in the reactor. Higher pulse repetition frequencies can be chosen to reduce the charge buildup as the flux to the walls is altered intermittently at a faster rate. The electron density in the late afterglow and steady state is shown in Fig. 3.17(a)-(f). The results are shown for pulse repetition frequencies of 5 kHz, 10 kHz, and 20 kHz. The electron density distribution in the late afterglow is different for different pulse repetition frequencies. The peak in the electron density is larger at 20 kHz as plasma is turned off for less time. A large electron density of nearly $2 \times 10^{11} \text{ cm}^{-3}$ exists even in the late afterglow. The electron density distributions for various frequencies are similar at steady state as shown in Fig. 3.17(d)-(f). This is because in all these cases, the on-time is sufficient for the plasma to return to the steady state as in continuous wave operation.

The variation of plasma potential and electron temperature with pulse repetition frequency are shown in Figs. 3.18 and 3.19. The peak plasma potential was higher for the lower pulse repetition frequency and decreased with the increase in the frequency. The peak plasma potential was 38 V for a pulse repetition frequency of 5 kHz and 33 V for a pulse repetition frequency of 20 kHz. The decay time for the plasma potential was 20 μs and was the same for all the frequencies as it is a function of collision frequency, which depends on pressure. The rise time was about 5 μs and was the same for all the frequencies. The peak electron temperature was 4.7 eV for a pulse repetition frequency of 5 kHz and 4 eV for pulse repetition frequency of 20 kHz. The decay and rise time were

similar to the plasma potential. The peak plasma potential and electron temperature were higher for the lower pulse repetition frequency because the electron density is much lower at lower pulse repetition frequency, so higher electron temperature is needed to avalanche the plasma from lower electron density.

The spatial distribution of plasma potential and electron temperature at the plasma turn-on for different pulse repetition frequencies are shown in Fig. 3.20. The electron temperature peaks under the inductive coil as most of the power deposition occurs in this region due to higher electric fields near the coil. The electron temperature distribution shows that higher electron temperature occurs for a lower pulse repetition frequency. As time progresses the electron temperature at the center of the plasma becomes more uniform as the hot electrons diffuse out and a steady state is attained. At the plasma turn-off, the center of the plasma becomes the coldest as all the hot electrons diffuse out and are closer to the walls. The plasma potential also shows a distribution similar to that of electron temperature. The peak in plasma potential is closer to the coil during the plasma turn-on. The peak in plasma potential is also larger at lower pulse repetition frequency, as shown in Fig. 3.20.

3.7 Effect of Pressure

The variation of pressure has a significant effect on the spatiotemporal dynamics of plasma properties such as electron density, electron temperature, and plasma potential in pulsed operation. In the present study the pressure is varied from 10 mTorr to 20 mTorr. The steady state electron density increased marginally with increase in pressure, as shown in Fig. 3.21. The peak electron density in the afterglow is higher at higher

pressures as the rate of diffusion losses is lower at higher pressures. The 2-D spatial distribution of electron density in the late afterglow is shown in Fig. 3.22. As seen from Fig. 3.22(c)-(d), the diffusion losses to the wall are larger at lower pressure as the effective diffusion coefficient is higher.

The plasma potential and electron temperature are shown in Figs. 3.23 and 3.24. The peak electron temperature is higher at lower pressures as the electron density in the late afterglow is lower at lower pressures due to the higher rate of diffusion loss. Therefore, to increase the plasma density to the steady state value at 300 W, higher electron temperature is required. The plasma potential shows a similar behavior. The peak plasma potential was 48 V at the pressure of 10 mTorr, while it was only 36 V at 20 mTorr. Similarly the electron temperature was 5.8 eV at 5 mTorr, but was only 4.3 eV at 20 mTorr. The electron temperature and plasma potential at the peak as the plasma is turned on are shown in Fig. 3.25. The peaks in electron temperature and plasma potential were below the inductive coil due to larger electric fields near the coil, and they were higher at lower pressures to avalanche the plasma from a lower electron density in the late afterglow.

3.8 Conclusions

The simulation studies of pulsed operation in argon ICPs show that pulse repetition frequency and duty cycle can significantly change plasma properties such as electron density, electron temperature, and plasma potential. In the present study, the 2-D simulations were performed by varying duty cycle, power, pulse repetition frequency, and pressure. As the duty cycle decreased, the peak electron temperature increased and

the peak value changed as the duty cycle was varied. The diffusion losses are significant even in late afterglow at higher duty cycles. The dynamics of plasma properties did not vary much with changes in peak input power. The plasma properties showed changes as the pulse repetition frequency varied. As the pulse repetition frequency decreased, the peak in electron temperature increased. The time averaged electron density was larger at higher pulse repetition frequencies. The spatial distribution of electron temperature showed a larger peak at lower pulse repetition frequencies. The peak electron temperature was higher as the pressure was lowered. The spatial distribution of electron density showed that losses due to diffusion are higher at lower pressures in the late afterglow. The simulation results compared well with the experiments.¹ The dynamics predicted captured the experimental trends closely. The rise and fall time predicted by the model were similar to the times reported.²

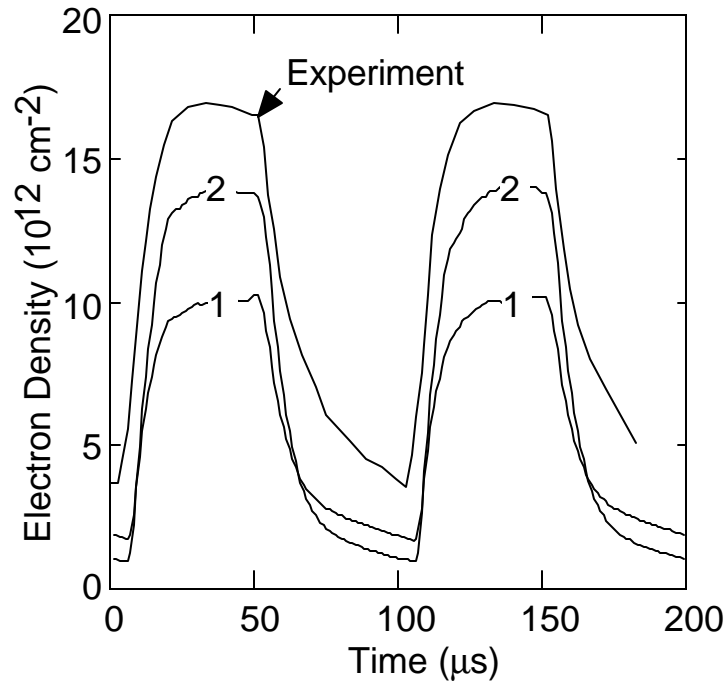


Figure 3.1 Comparison of experimental electron density with results of the simulations (1 and 2) for a peak input power of 300 W, pulse repetition frequency of 10 kHz, and duty cycle of 50%.

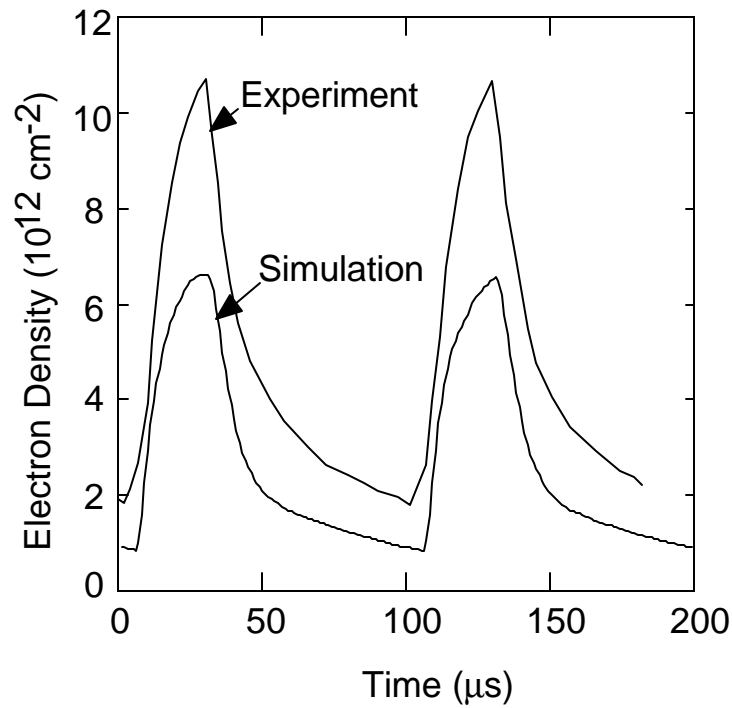


Figure 3.2 Comparison of experimental electron density with results of the simulation for a peak input power of 190 W, pulse repetition frequency of 10 kHz, and duty cycle of 30%.

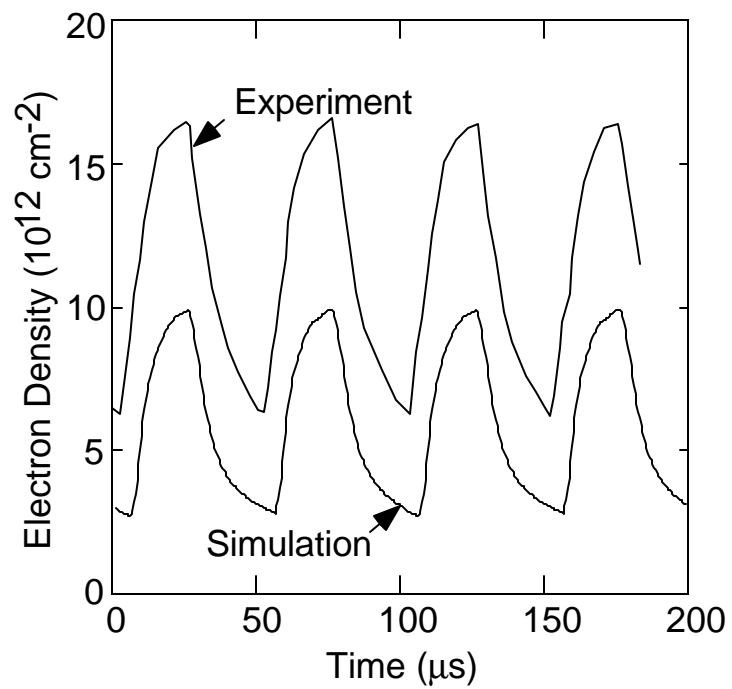


Figure 3.3 Comparison of experimental electron density with results of the simulation for a peak input power of 300 W, pulse repetition frequency of 20 kHz, and duty cycle of 50%.

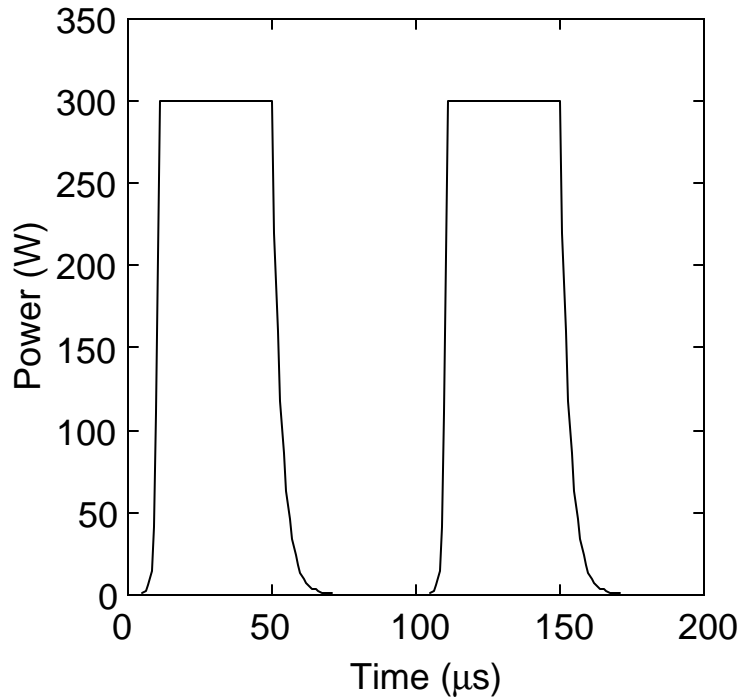


Figure 3.4 Power modulation for the base conditions (peak input power of 300 W, pulse repetition frequency of 10 kHz, and duty cycle of 50%).

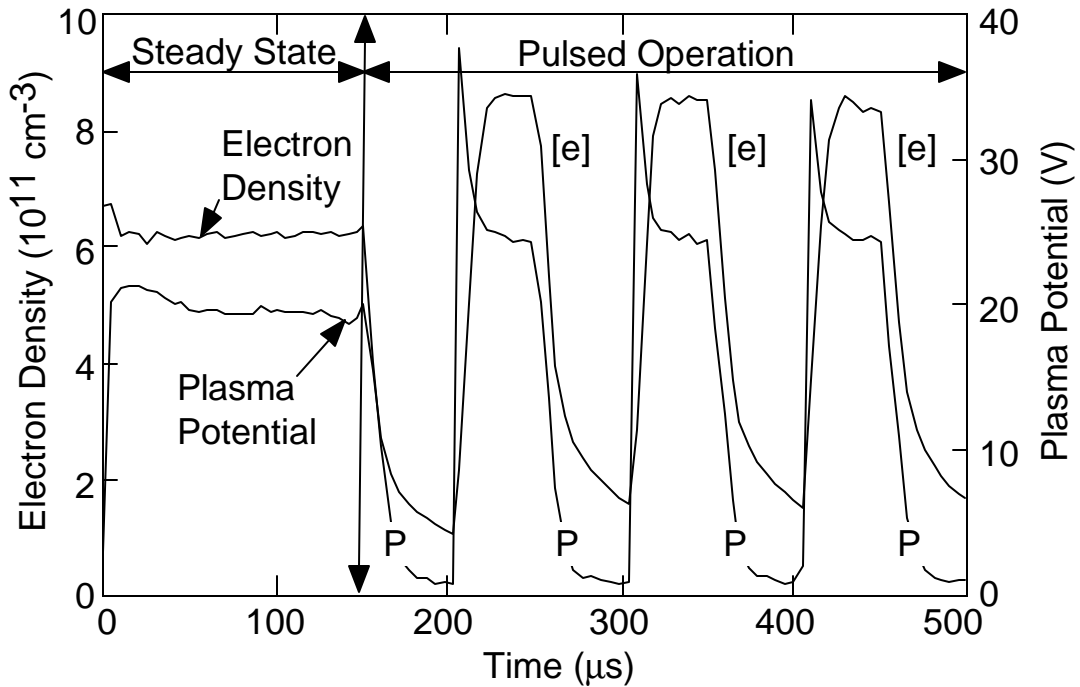


Figure 3.5 Peak electron density and plasma potential for the base case conditions of peak input power of 300 W, pulse repetition frequency of 10 kHz, and duty cycle of 50%.

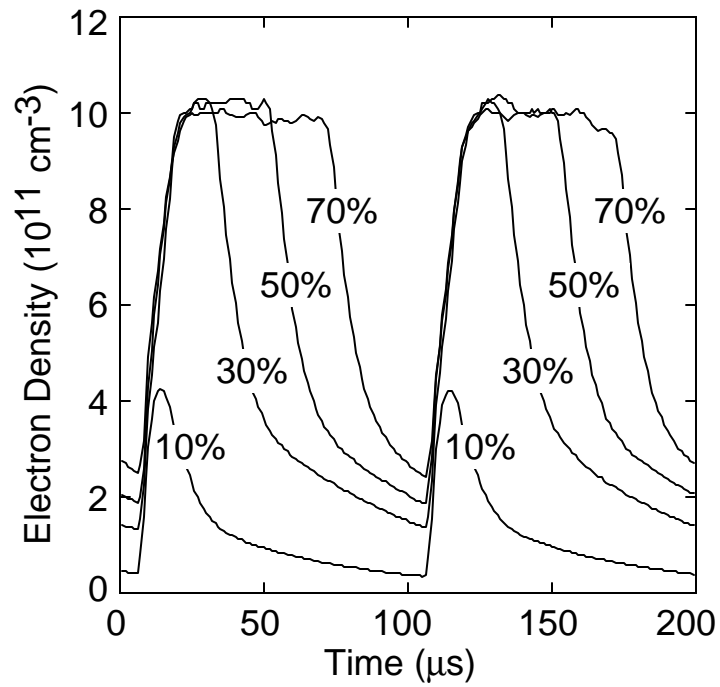


Figure 3.6 Electron density in argon plasma as a function of time for different duty cycles for a constant peak power of 300 W and pulse repetition frequency of 10 kHz.

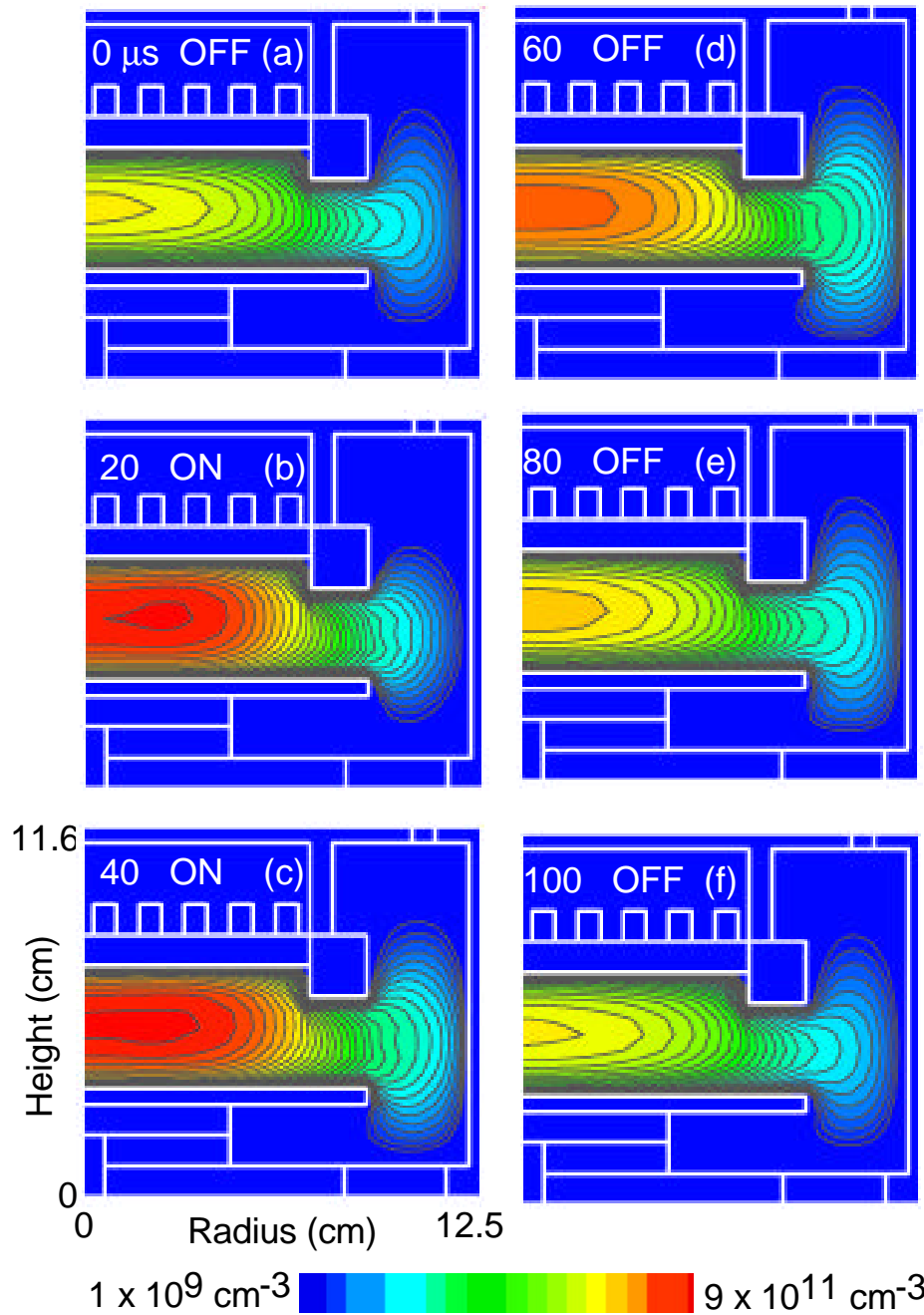


Figure 3.7 Electron density at different times as the pulse is turned on and off with a frequency of 10 kHz and duty cycle of 50%. The figures a, b, and c are at 0 μs , 20 μs , 40 μs during the pulse after the power is turned on and figures d, e, and f are at 60 μs , 80 μs , 100 μs during the pulse after the power is turned off at 50 μs .

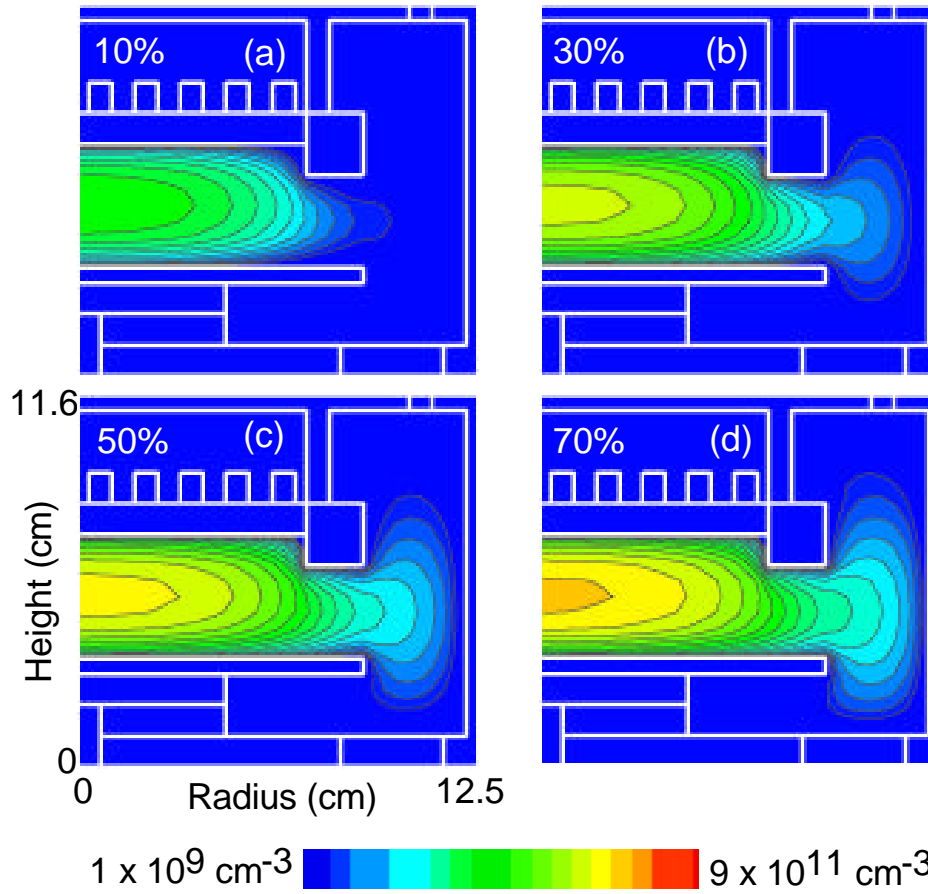


Figure 3.8 Electron density in the late afterglow as a function of duty cycle for a peak input power of 300 W and pulse repetition frequency of 10 kHz. The figures a, b, c, and d are for duty cycles of 10%, 30%, 50%, and 70% respectively.

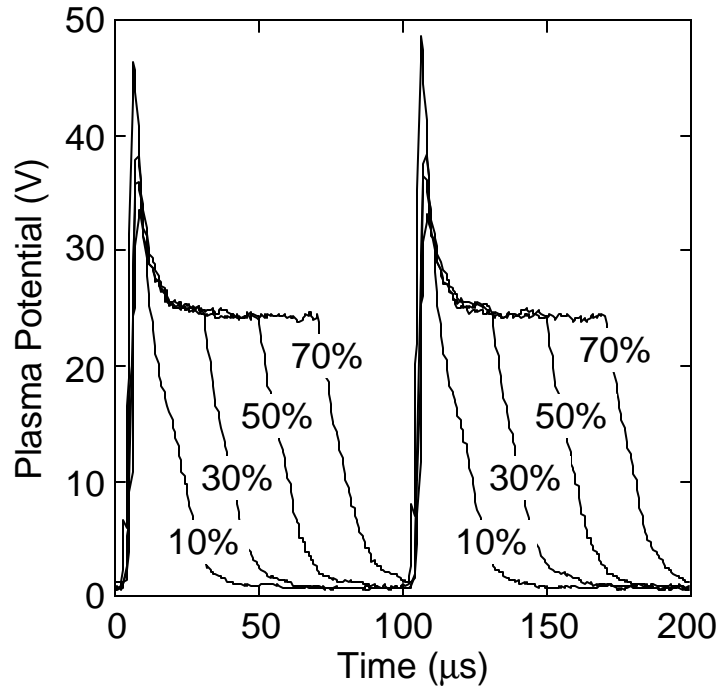


Figure 3.9 Plasma potential in argon plasma as a function of time for different duty cycles for a constant peak power of 300 W and pulse repetition frequency of 10 kHz.

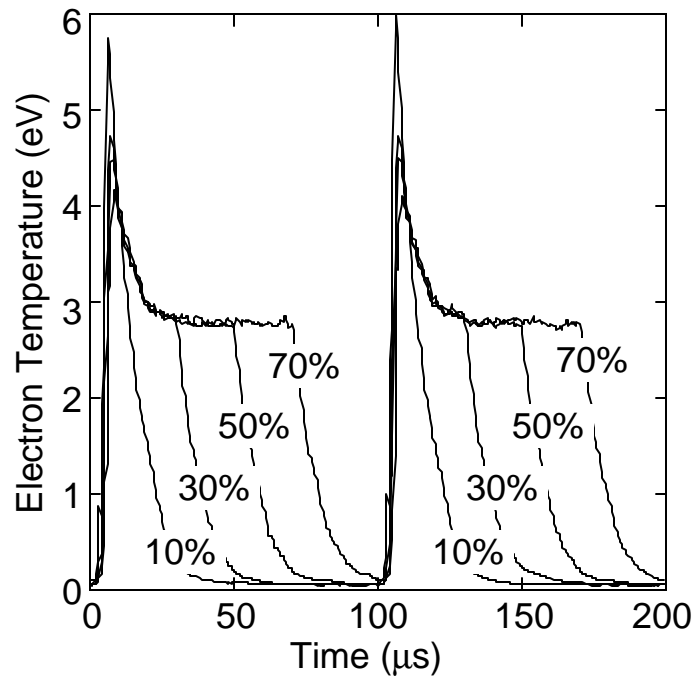


Figure 3.10 Electron temperature in argon plasma as a function of time for different duty cycles for a constant peak power of 300 W and pulse repetition frequency of 10 kHz.

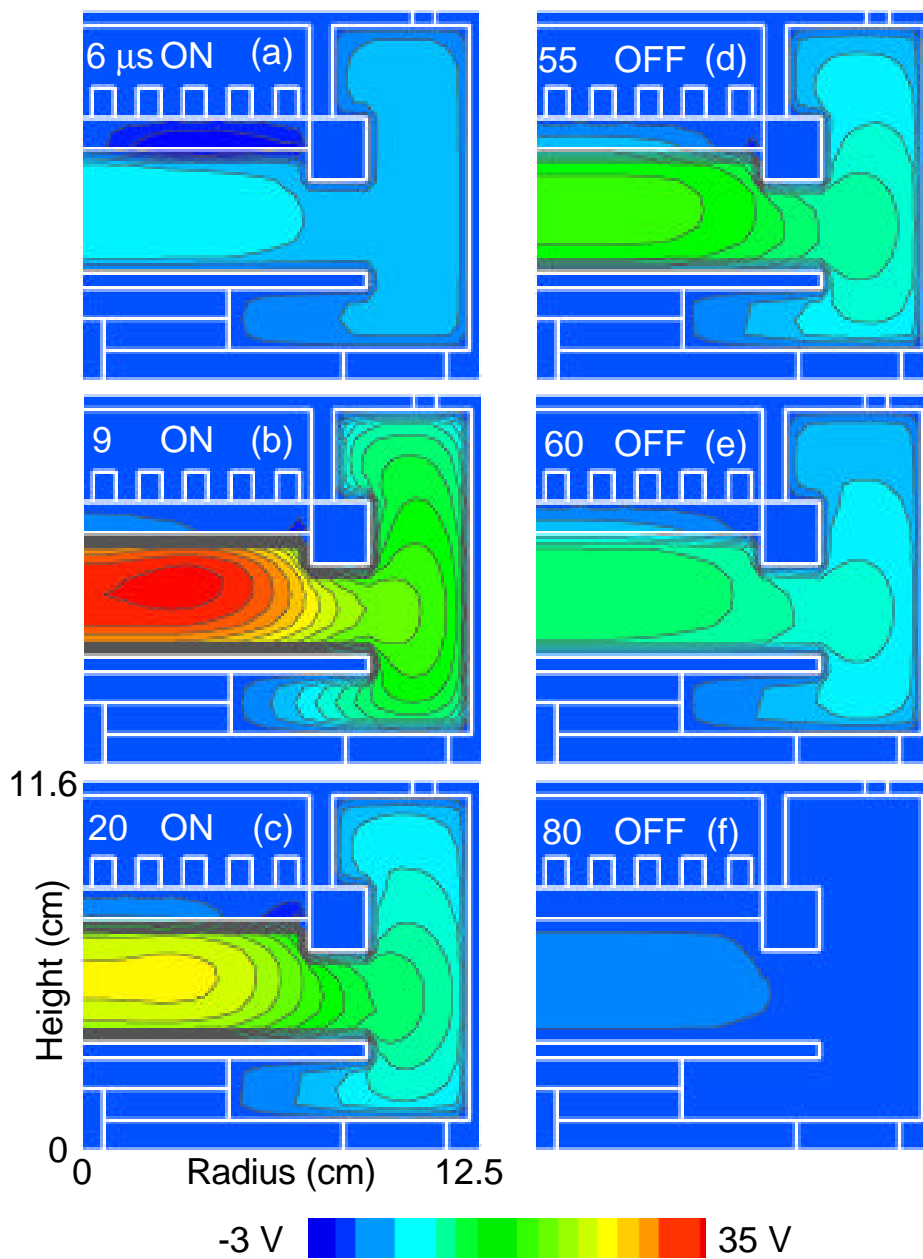


Figure 3.11 Plasma potential at different times as the pulse is turned on and off with a frequency of 10 kHz and duty cycle of 50%. The figures a, b, and c are at 6 μs , 9 μs , 20 μs during the pulse after the power is turned on and figures d, e, and f are at 55 μs , 60 μs , 80 μs during the pulse after the power is turned off at 50 μs .

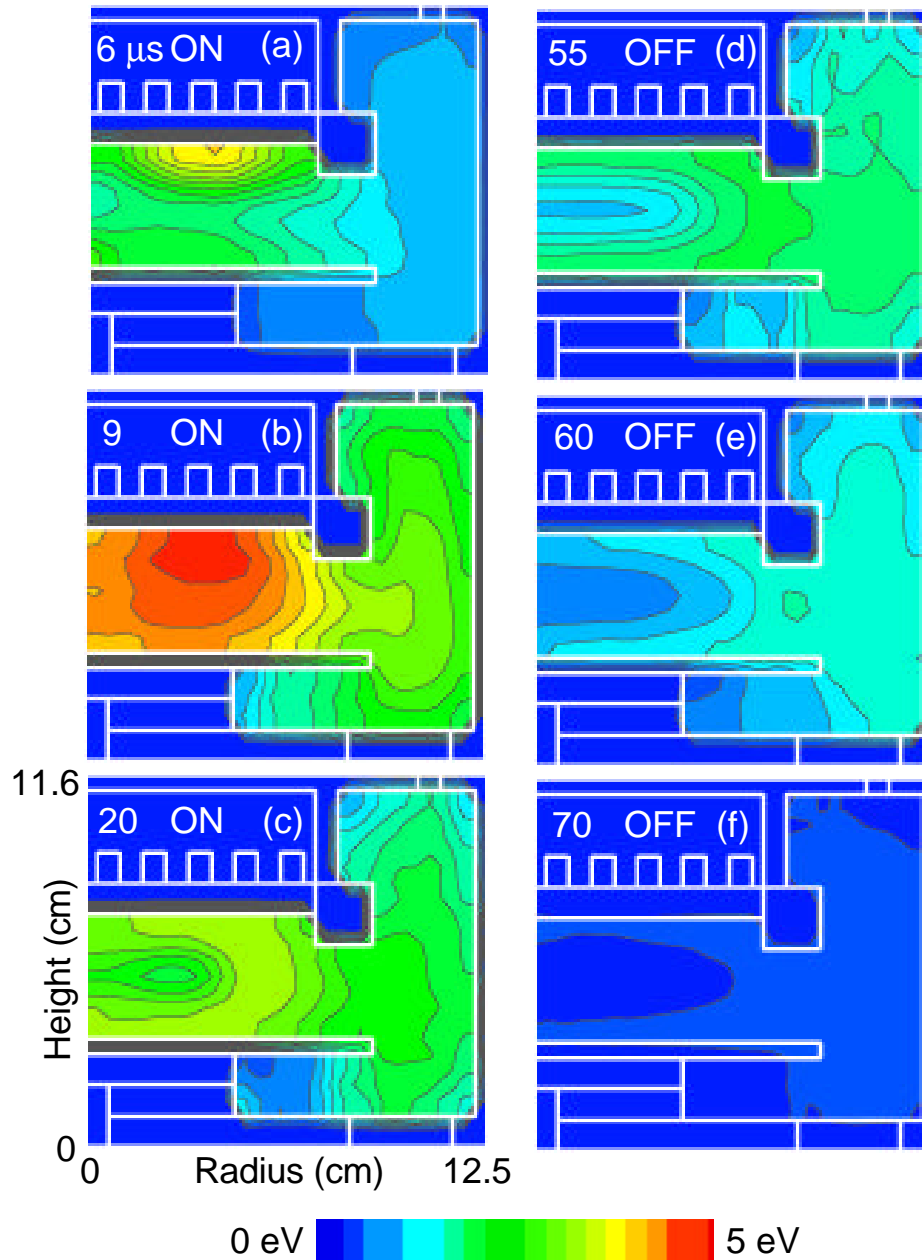


Figure 3.12 Electron temperature at different times as the pulse is turned on and off with a frequency of 10 kHz and duty cycle of 50%. The figures a, b, and c are at 6 μ s, 9 μ s, 20 μ s during the pulse after the power is turned on and figures d, e, and f are at 55 μ s, 60 μ s, 80 μ s during the pulse after the power is turned off at 50 μ s.

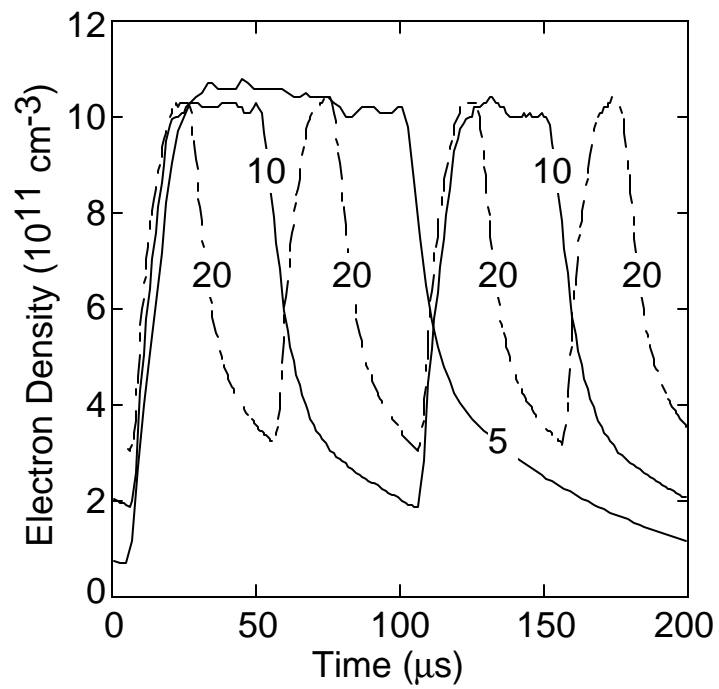


Figure 3.13 Electron density at different times as a function of power for a pulse repetition frequency of 10 kHz and duty cycle of 30%.

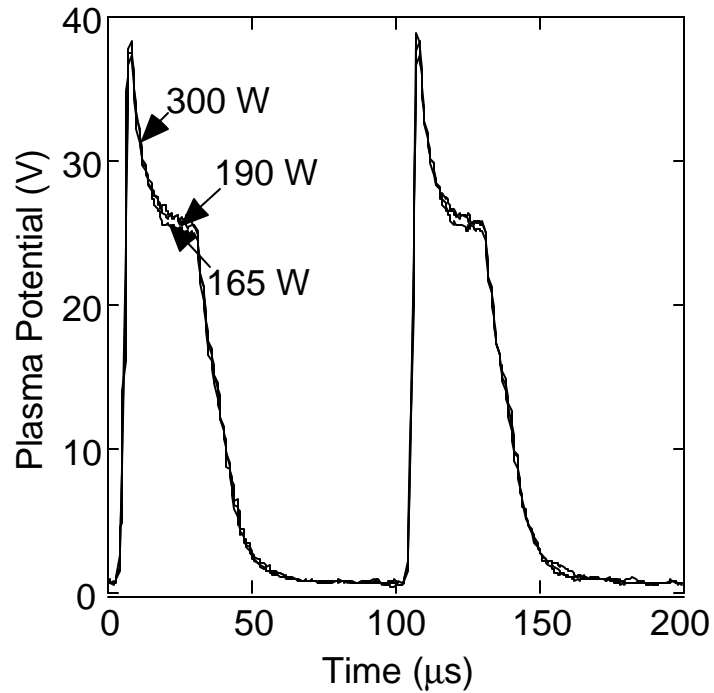


Figure 3.14 Plasma potential at different times as a function of power for a pulse repetition frequency of 10 kHz and duty cycle of 30%.

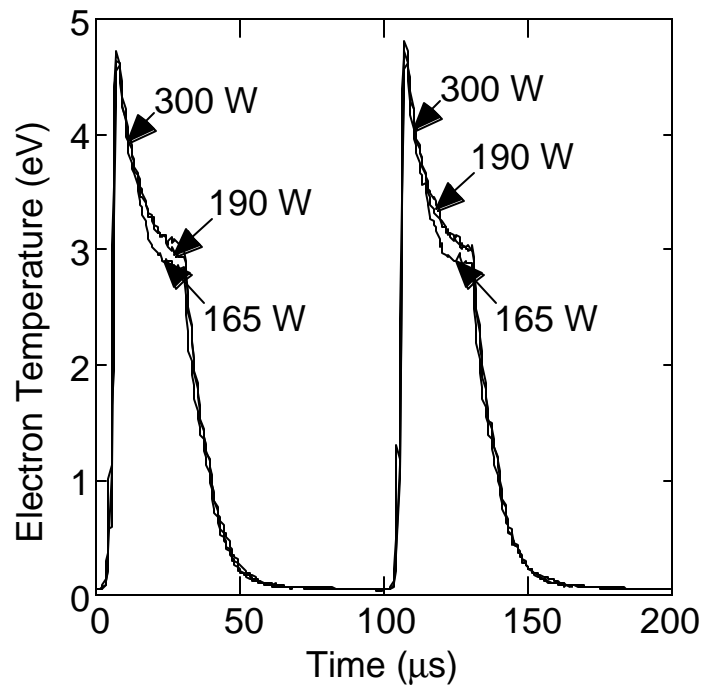


Figure 3.15 Electron temperature at different times as a function of power for a pulse repetition frequency of 10 kHz and duty cycle of 30%.

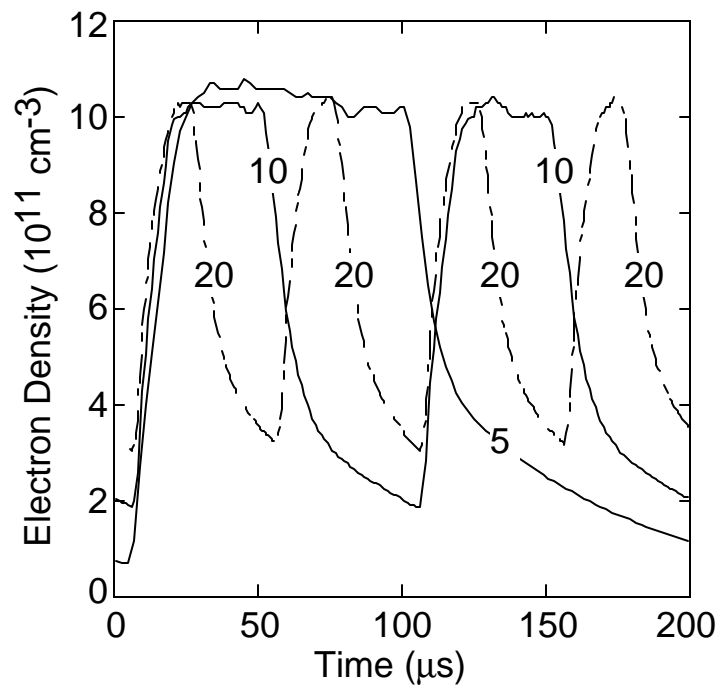


Figure 3.16 Electron density at different times as a function of pulse repetition frequency for a peak input power of 300 W and duty cycle of 30%.

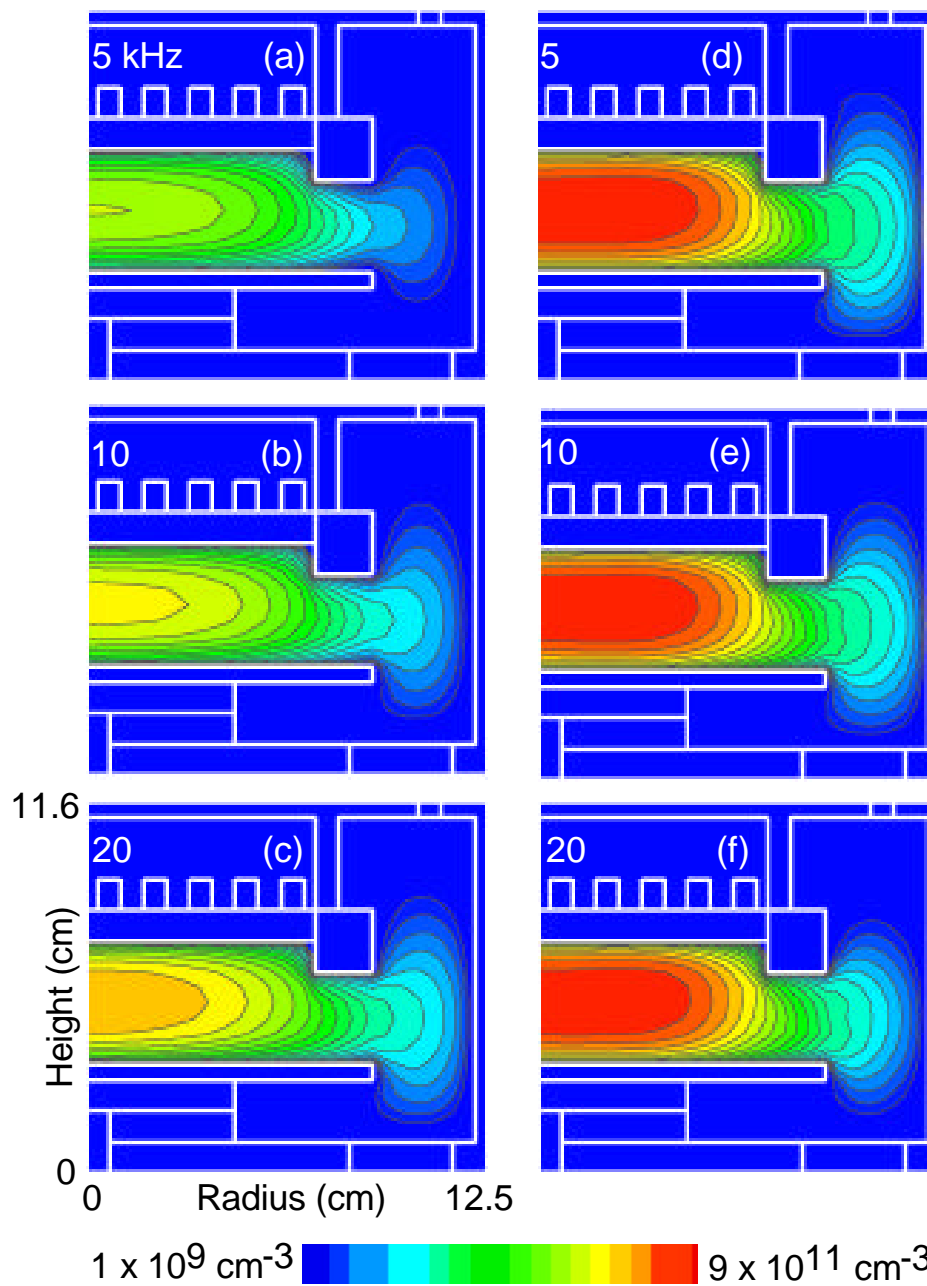


Figure 3.17 Electron density in late after glow (a-c) and steady state (d-f) as a function of pulse repetition frequency for a peak input power of 300 W and duty cycle of 50%.

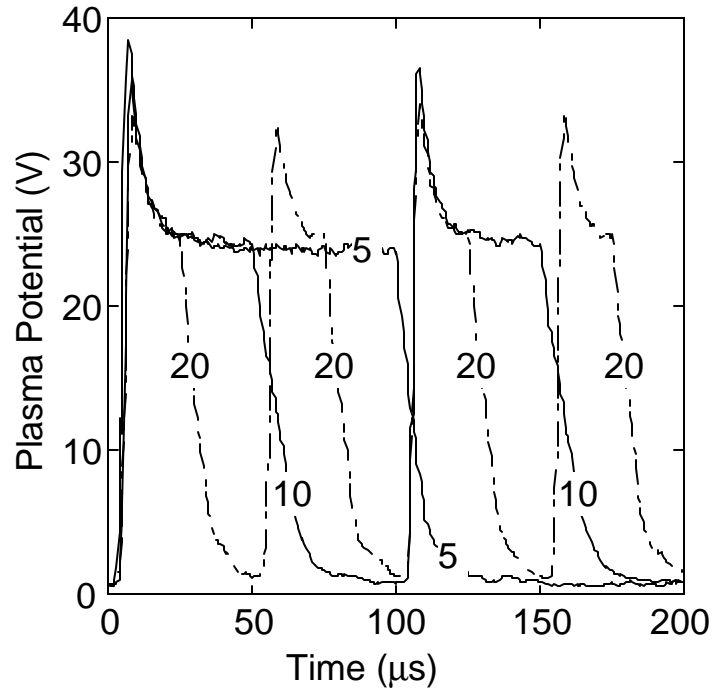


Figure 3.18 Plasma potential at different times as a function of pulse repetition frequency for a peak input power of 300 W and duty cycle of 30%.

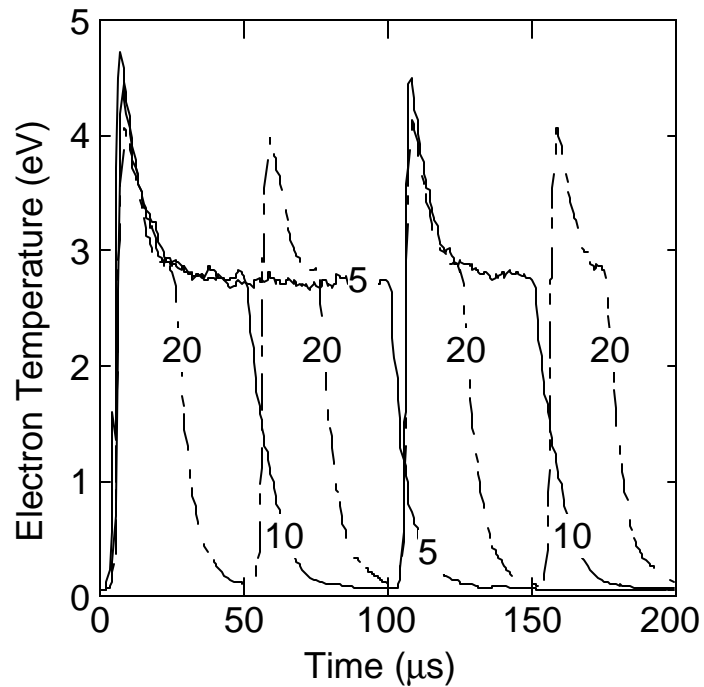


Figure 3.19 Electron temperature at different times as a function of pulse repetition frequency for a peak input power of 300 W and duty cycle of 30%.

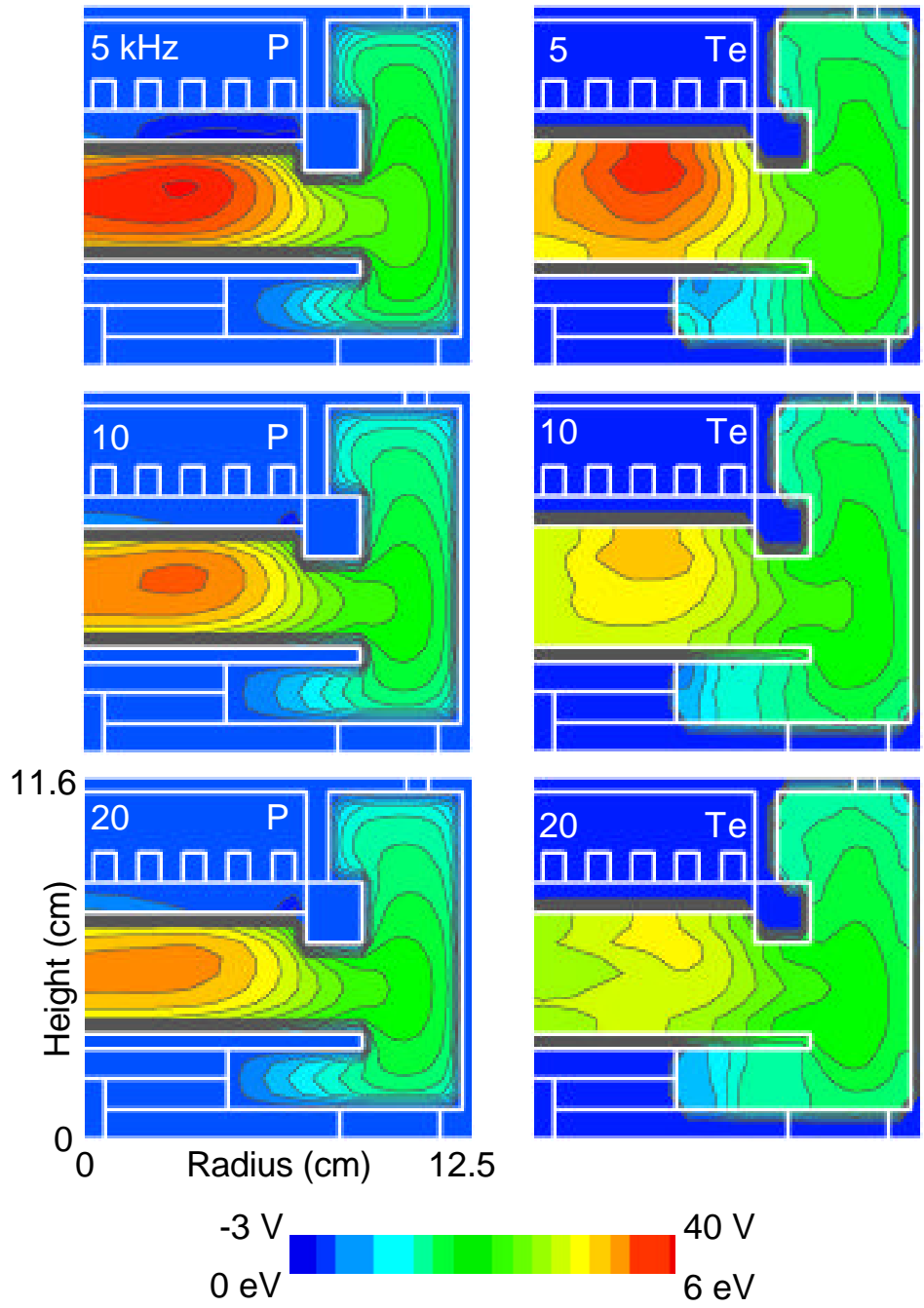


Figure 3.20 Plasma potential (P) and electron temperature (Te) when the peak in electron temperature occurs during the pulse as a function of pulse repetition frequency for a peak input power of 300 W and duty cycle of 50%.

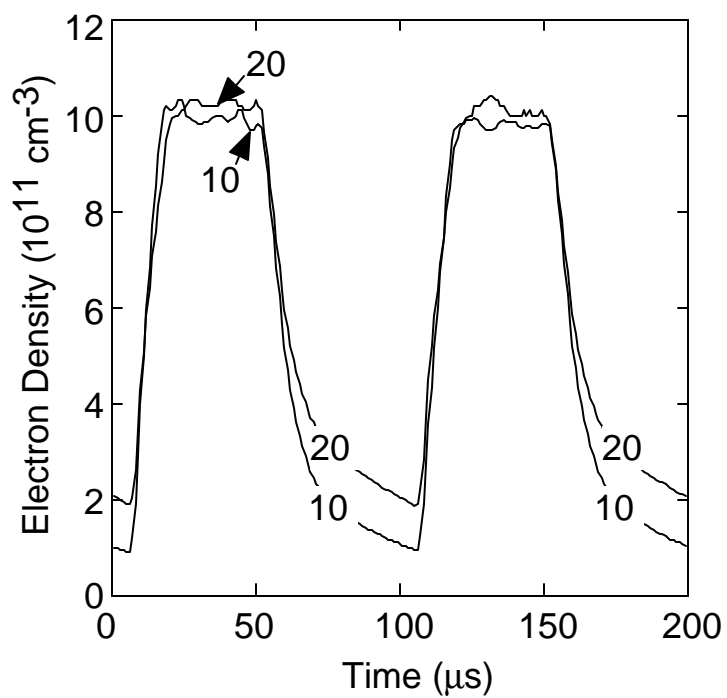


Figure 3.21 Electron density at different times as a function of pressure (mTorr) for a peak input power of 300 W, pulse repetition frequency of 10 kHz, and duty cycle of 50%.

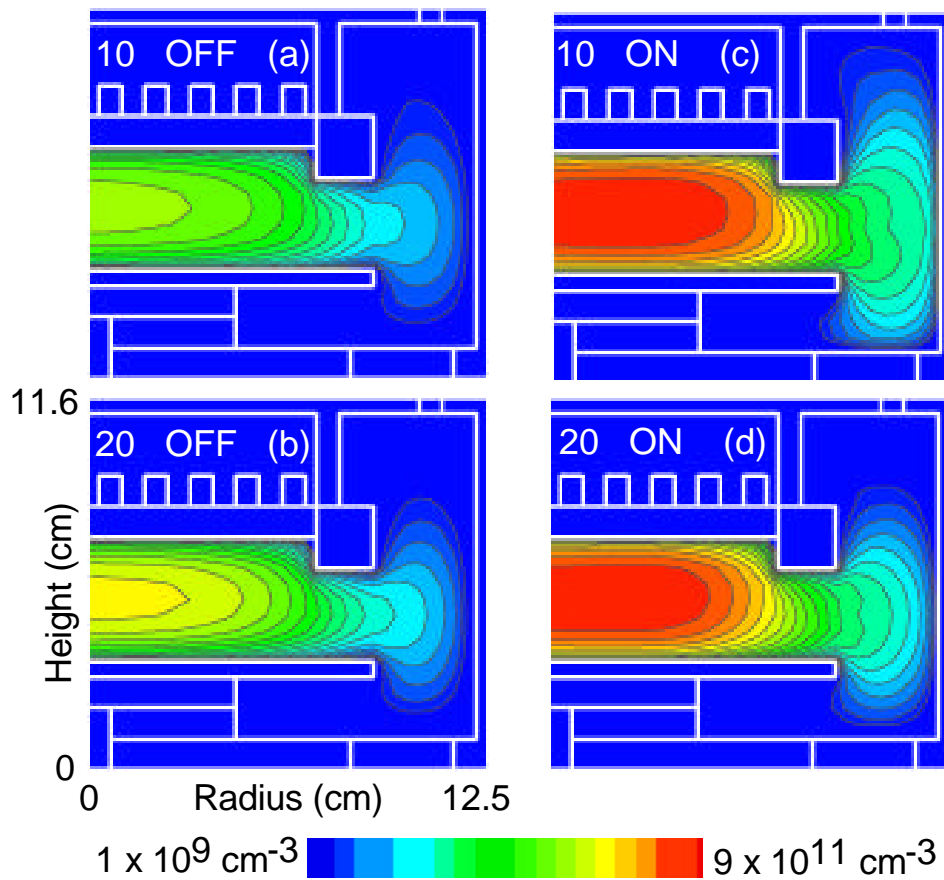


Figure 3.22 Electron density in the late after glow (a-b) and steady state (c-d) as a function of pressure (mTorr) for a peak input power of 300 W, pulse repetition frequency of 10 kHz, and duty cycle of 50%.

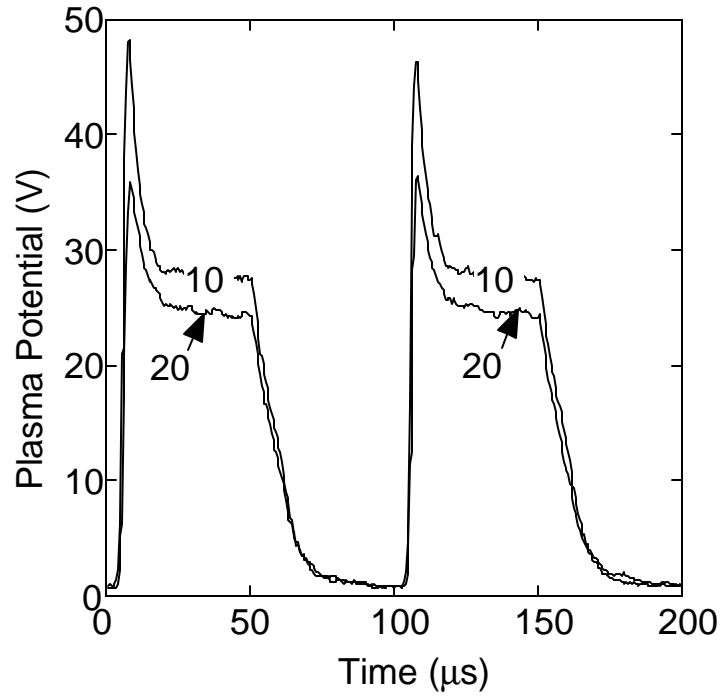


Figure 3.23 Plasma potential at different times as a function of pressure (mTorr) for a peak input power of 300 W, pulse repetition frequency of 10 kHz, and duty cycle of 50%.

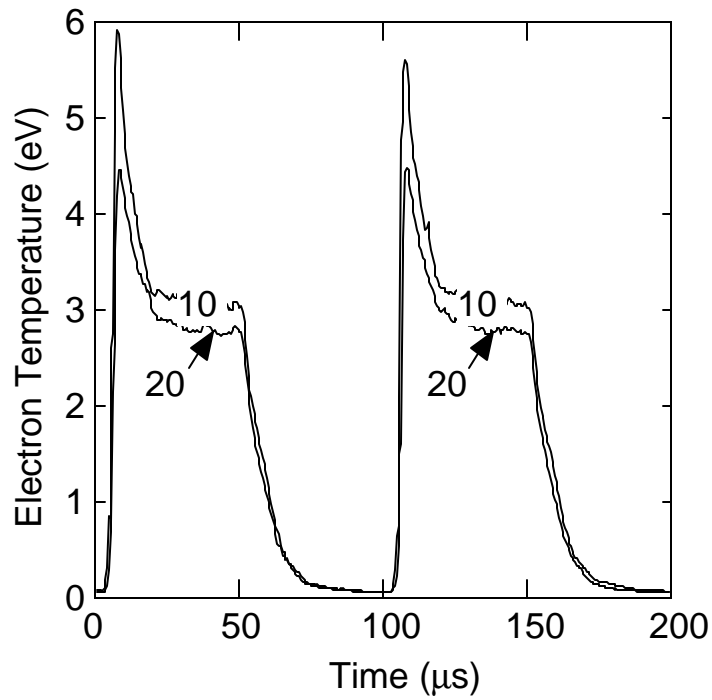


Figure 3.24 Electron temperature at different times as a function of pressure (mTorr) for a peak input power of 300 W, pulse repetition frequency of 10 kHz, and duty cycle of 50%.

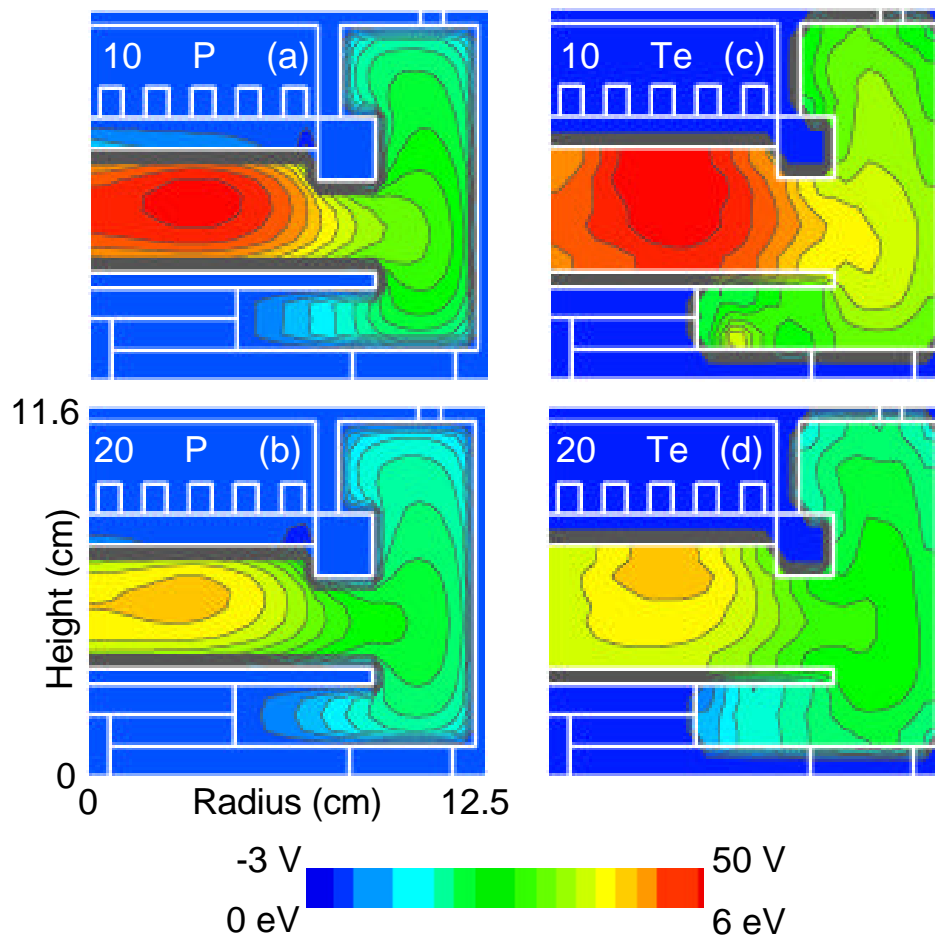


Figure 3.25 Plasma potential (a-b) and electron temperature (c-d) when the peak in electron temperature occurs during the pulse as a function of pressure (mTorr) for a peak input power of 300 W, pulse repetition frequency of 10 kHz and duty cycle of 50%.

3.9 References

1. G. A. Hebner and C. B. Fleddermann, J. Appl. Phys. **82**, 2814 (1997)
2. S. Ashida, M. R. Shim, and M. A. Leiberman, J. Vac. Sci. Technol. A **14**, 391 (1996)

4. INVESTIGATIONS OF Ar/Cl₂ PULSED PLASMAS

4.1 Introduction

In this chapter, the results from our investigations on Ar/Cl₂ pulsed plasmas are presented. The consequences of varying the pulse characteristics such as the duty cycle and the pulse repetition frequency are quantified. The effects of pressure and power on the pulsed plasma properties were also investigated. The plasma properties such as electron density, electron temperature, plasma potential and Cl⁻ ion density were tracked during the pulsed operation. The transients in the negative ion flux to the walls during the pulse and the spatiotemporal dynamics of the plasma properties as the pulse progresses are discussed. The simulation results are qualitatively compared with experiments performed in electronegative plasmas.^{1, 2}

4.2 Comparison with Experiments

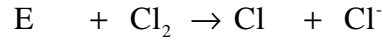
To validate the model, the simulation results were compared to experiments.^{1, 2} Hebner et al.¹ performed studies in pulse modulated chlorine plasmas in a GECRC by measuring the time dependent electron density and the Cl⁻ density. They also reported on the rf plasma potential in chlorine plasmas for the first few μs after power turn-on. The simulation conditions were similar to these experiments, with a feed gas mixture of Ar/Cl₂ = 80/20 at 20 mTorr. Only a qualitative comparison is made here as the simulations were performed with Ar/Cl₂ gas mixture instead of pure chlorine. Modeling plasma ignition after turn-off in pure chlorine plasmas required a constraint of minimum electron density in the late afterglow. Such a forceful constraint may affect the numerical

validity of the predictions and so is avoided in the present study by investigating electronegative plasmas in Ar/C₂ for which this problem does not arise. The trends in CI density during the pulse are captured well by the simulations as shown in Fig. 4.1. One-dimensional models³ have had difficulty capturing the exact dynamics of CI density seen in experiments, which is well explained with the present 2-D simulation. The 1-D model proposed by Midha et al.³ assumed a spatially uniform power input and Maxwellian distribution for electron energy distribution, which is not correct for low electron density in the early active glow. The two significant successes of our model are predicting the temporal evolution of CI density and the variation of electron density with pulse repetition frequency as observed in experiments. The 1-D model did not capture the non-monotonic behavior in electron density with pulse repetition frequency and did not capture the decrease in CI density in the late active glow in the center of the reactor. Our model captures both these trends as observed in experiments. An increase in electronegativity (about ten times) was observed by Malyshev et al.² in the late afterglow in pulsed C₂ plasmas at 10 mTorr with a peak power of 480 W modulated at 10 kHz and duty cycle of 50%. Simulations here also predict an increase in electronegativity (about 2-3 times) in the late afterglow in Ar/C₂ plasmas at 20 mTorr with a peak input power of 300 W modulated at 10 kHz and duty cycle of 50%.

4.3 Base Case Conditions

Simulations were performed for GECRC for a feed gas mixture of Ar/C₂ = 80/20 as shown in Fig. 1.1. The base case conditions were a total pressure of 20 mTorr and peak power of 300 W modulated at a pulse repetition frequency of 10 kHz and duty cycle of

50%. The Ar/Cl₂ reaction chemistry is given in Appendix B. Dissociative attachment of Cl₂ is given by



The rate of dissociative attachment determines the temporal evolution of electron density and ion density in the afterglow. The rate coefficient of dissociative attachment for Cl₂ scales inversely with electron temperature. The duty cycle was varied from 10% to 70%, and the pulse repetition frequency was varied from 5 kHz to 20 kHz. The peak power was varied from 165 W to 300 W, while the pressure was varied from 10 mTorr to 20 mTorr.

The electron density and electron temperature for the base case are shown in Fig. 4.2. The plasma is pulsed for four or more pulses to attain a periodic steady state in all simulations. When the plasma is turned off, the electron density decays monotonically. In the early afterglow, the rate of electron decay is higher as electrons are lost by ambipolar diffusion to the walls and by the dissociative attachment. In the late afterglow, the rate of electron decay decreases as the rate of dissociative attachment decreases and the loss of electrons is due to ambipolar diffusion losses. After the power is turned off, there is significant loss of electron energy due to collisions. Hence the electron temperature drops rapidly in the first few μ s. In the late afterglow, the rate of electron temperature decay becomes slower as the rate of inelastic collisions decreases due to lower electron temperature. The electron temperature reduces to a few eV in about 10 μ s for the base case conditions. The plasma potential shows similar transient behavior as the electron temperature.

When the power is turned on, the electron temperature peaks as the power deposition occurs in a small number of electrons. The production of electrons from

electron impact ionization reactions increases as the electron temperature rises and eventually supersedes the diffusion losses. The electron temperature then decreases to the quasi-steady-state value corresponding to the continuous wave operation. The electron density increases at a slower rate than electron temperature to reach the quasi-steady-state value corresponding to the peak input power. The rise time for electron density is about 50 μ s, while that for electron temperature is only about 5 μ s.

4.4 Effect of Duty Cycle

The effect of duty cycle on the plasma properties during the pulsed operation was investigated by varying the duty cycle from 10% to 70%. The results presented here are for duty cycles of 10%, 30%, 50%, and 70%. The peak input power was 300 W modulated at a pulse repetition frequency of 10 kHz. The total gas pressure was 20 mTorr.

The electron density at the center of the reactor is shown in Fig. 4.3. The electron density attains a quasi-steady-state value of $8 \times 10^{11} \text{ cm}^{-3}$ for the duty cycle of 70%. For all the other duty cycles, the on time is not sufficient for a quasi-steady-state to be attained. Higher duty cycles resulted in a steady state electron density, because there was enough time for establishing the balance between the loss and gain of electrons. At the power turn-off, the electron density decays. The rate of decay is faster in the early afterglow than in the late afterglow because the loss of electrons is due to the increased dissociative attachment rate and more rapid ambipolar diffusion in the early afterglow. The increased dissociative attachment rate is caused by the loss of electron energy due to inelastic collisions as the power is turned off, resulting in lower electron temperature. The

decay rate for different duty cycles is nearly same because it depends on the ambipolar diffusion rate, which scales with electron temperature and the rate of dissociative attachment, which scales inversely with electron temperature.

The temporal dynamics of CI density are shown in Fig. 4.4. The CI density significantly varies with different duty cycles. The peak CI density occurs at power turn-on and decreases as the duty cycle decreases. The CI density increases immediately as the power is turned on because the negative ions move to the center of the plasma, where the plasma potential is most positive. The peak density is larger at higher duty cycles because the CI density in the late afterglow is higher at higher duty cycles, and a larger number of CI move to the center of the plasma at power turn-on. As the electron temperature increases, the rate of dissociative attachment decreases, and hence the CI density decreases after peaking initially during the pulse-on period. Higher quasi-steady-state electron temperature in the late activeglow results in an increase the rate of ionization, forming a large number of positive ions, which then recombine with CI ions, thus resulting in the decrease of CI density in the late activeglow. When the power is turned off, the CI density rises as the rate of dissociative attachment increases with a decrease in electron temperature. At lower duty cycles, the off time is sufficient for the ambipolar diffusion losses to overcome the production of CI ions by dissociative attachment; therefore, the CI density decreases in the late afterglow. Thus, depending on the process requirement, the duty cycle can be varied to change the negative ion density and flux to the walls in the pulsed operation.

The 2-D spatiotemporal dynamics of electron density for the base case conditions are shown in Fig. 4.5. The electron densities at different instants of time during a single

pulse are shown. As the power is turned on, the electron density increases and the peak in electron density occurs under the inductive coil as the majority of power deposition occurs there. This is because the electric fields peak near the coil and the power deposition scales as the square of the electric field. As time progresses, a quasi-steady state is attained with plasma having an electronegative core and electropositive periphery. This is due to the electrostatic fields established to push the negative ions from the walls during the on period. When a quasi steady state is attained, the peak in electron density is about $6.5 \times 10^{11} \text{ cm}^{-3}$ and is at the center of the reactor. As the power is turned off, the electrons are lost due to ambipolar diffusion and dissociative attachment. The plasma then turns from electron-ion plasma to ion-ion plasma as shown in Fig. 4.6, where the Cl⁻ density is plotted. The Cl⁻ density increases and the plasma develops an electropositive core as seen in Figs. 4.5(f) and 4.6(f) with a uniform Cl⁻ density in the center of the plasma. The peak Cl⁻ density in the late afterglow was $1 \times 10^{11} \text{ cm}^{-3}$, while the electron density was $6 \times 10^{10} \text{ cm}^{-3}$, and hence the plasma is ion dominated. During the on period in the pulsed operation, the negative ions tend to move to the center of the plasma. However, due to the inertia of the ions, there is still a significant number of ions in the outer region which are not able to move to the center of the plasma as seen in Fig. 4.6(c)-(e). The acceleration of electrons scales with the electric field, and it takes about 25 μs for the ions to move to the center of the plasma from the periphery. However, the plasma potential varies at a faster rate similar to electron temperature; hence, the ions lag behind the changes in the plasma potential. Thus, the spatial distribution of negative ions shows localized peaks in density, which can be disastrous for processing.

The temporal dynamics of plasma potential and electron temperature are shown in Figs. 4.7 and 4.8, respectively. The plasma potential and electron temperature show similar transient behavior. When the power is turned off, the plasma potential and electron temperature decay rapidly. The decay in electron temperature is due to loss of electron energy due to inelastic collisions. The rate of decay of electron temperature is the same for all duty cycles as it depends on the collision frequency, which scales with pressure. For the 10% duty cycle case, the electron temperature and plasma potential peak exceptionally high at plasma turn-on. The heating rate for the 10% duty cycle case is about 10 MeV per second. This is due to the deposition of a large amount of power in a small number of electrons existing in the late afterglow for the 10% duty cycle case. The electron density for the 10% duty cycle decays to very low values of $3 \times 10^9 \text{ cm}^{-3}$, which is 2 orders of magnitude lower than the 70% duty cycle case. The decay time of the electron temperature was about 30 μs while the rise time was about 4 μs and was similar for different duty cycles.

The spatial distributions of plasma potential and electron temperature are shown in Figs. 4.9 and 4.10. The plasma potential and electron temperature peak under the coil at plasma turn-on due to larger electric fields near the coils, causing larger power deposition. As time progresses, plasma potential and electron temperature attain a quasi-steady state as seen in Figs. 4.9(c) and 4.10(c), respectively. During the power turn-off, the electron temperature decreases at the center of the plasma more rapidly as the hot electrons are lost from the center due to ambipolar diffusion. As seen from Fig. 4.8(d), there is small island of lower plasma potential in the periphery where the negative ion

density shows a local peak. This plasma potential distribution is established to redistribute the source of negative ions produced at that location in the reactor.

The spatiotemporal dynamics of the CI flux at different times during the pulse are shown in Fig. 4.11. When the pulse is turned on, the negative ion flux moves away from the walls of the reactor as seen in 4.11(b). The ions tend to move to the peak in plasma potential at the center of the plasma. The ions from the periphery also tend to move to the center of the plasma. However, inertia prevents the heavier ions from immediately following the changes in the plasma potential. There are still negative ions moving towards the wall at 5 μs after the plasma turn-on at locations near the nozzle and the pump port. This is because the ambipolar electric fields were about 0.1 V/cm and were still smaller and hence did not trap the negative ions. As seen in Fig. 4.11(c), at about 10 μs after the power-on, the ions tend to move away from the wall at all reactor locations. When the power is turned off, the ions which were in the center of the plasma move towards the wall immediately due to ambipolar diffusion as seen in Fig. 4.11(e). However, the ions from the periphery still try to move to the center of the plasma because it takes some time for these ions to respond to the pulse turn off. This is because the motion of ions depends on the strength of the electric fields. The electric field in the bulk plasma is about 2 to 3 V/cm, and hence it takes about 25 μs for the ions to reach the center from the periphery. After 90 μs , the plasma potential has been significantly reduced and the negative ion flux is directed towards the wall of the reactor at all spatial locations due to the ambipolar diffusion as seen in Fig. 4.11(f). Thus, the negative ion flux to the walls can be altered by pulsed operation, which can significantly reduce the charge buildup in fine features.

4.5 Effect of Power

The effect of power on plasma properties was investigated by varying from 165 W to 300 W. The gas pressure was 20 mTorr, the pulse repetition frequency was 10 kHz, and the duty cycle was 30%. The electron density scales linearly with power as shown in Fig. 4.12. The pulse-on time is not sufficient for establishing a quasi-steady state. As the peak power was reduced, the peak electron density also decreased. The variation of CI density with time as a function of power is shown in Fig. 4.13. The CI density was lower in the late activeglow at higher power as the C_2 undergoes more dissociation rather than attachment. The peak in CI density in the afterglow was nearly the same for all the cases as the peak corresponds to the establishment of a balance between loss due to ambipolar diffusion and generation due to dissociative attachment. These two processes are dependent on electron temperature in the afterglow, which was same in all the three cases. The electron and CI densities in the late afterglow for various powers are shown in Fig. 4.14. In the late afterglow the electronegativity of the plasma increases as the plasma transits from an electron-ion plasma in the on-period to ion-ion plasma in the off-period. The electronegativity of the plasma in the late afterglow is higher at lower powers as the electron density drops to lower values at lower powers. At 70 μ s after pulse turn-off, the ratio of CI density to electron density was 3.7 for a power of 300 W, while it was 7.75 for a power of 165 W at the center of the plasma

The plasma potential and electron temperature are shown in Figs. 4.15 and 4.16. The plasma potential peaked around 40 V and electron temperature at about 7 eV during the power turn on. The decay time for electron temperature is about 25 μ s, while the rise time is about 5 μ s. The spatial distribution of plasma potential and electron temperature

when the peak in electron temperature occurs during the initial on-phase of the pulse are shown in Fig. 4.17. The plasma potential and electron temperature peak under the coils where the peak in power deposition is located. The spatial distribution of electron temperature and plasma potential was also similar for the different powers chosen in the present study.

4.6 Effect of Pulse Repetition Frequency

Pulse repetition frequency is an important operating parameter in pulsed operation of plasmas. By varying the pulse repetition frequency, the on and off time, can be controlled to meet the necessary process requirement. This feature is not available to process engineers in continuous wave operation. The effect of pulse repetition frequency was investigated by varying it from 5 kHz to 20 kHz. The peak input power was 300 W and the duty cycle was 50%.

The time evolution of electron density in the center of the plasma is shown in Fig. 4.18 for pulse repetition frequencies of 5 kHz, 10 kHz, and 20 kHz. As the pulse repetition frequency was lowered to 5 kHz from the base case value of 10 kHz, a quasi-steady state was attained. This is because the plasma is turned on for enough time to establish a balance of gains and losses of electrons. As the pulse repetition frequency was increased to 20 kHz, the electron density did not attain a quasi-steady-state value. The electron decay rate was similar for all the cases. However, as the pulse is turned off for a longer time in the 5kHz case, the electron density decays to lower values. This is due to the higher rate of dissociation of C_2 at lower duty cycles and the lower rate of dissociative attachment. The temporal dynamics of CI density are shown in Fig. 4.19.

The peak in CI density in the initial phase of the power turn-on period was higher for 10 kHz and 20 kHz. This is because of the higher CI density in the late afterglow, which moves to the center of the plasma at the power turn-on as the plasma is more positive at the center. For the 5 kHz case, the off time during a pulse was long enough so that the diffusion losses dominate over the production of negative ions by dissociative attachment; hence the negative density attains a peak at about 50 μ s after plasma turn-off. For the 10 kHz and 20 kHz cases, the off time was not sufficiently long for ambipolar diffusion losses to overcome the generation due to dissociative attachment, hence a peak in negative density in the afterglow is not observed.

The spatial distribution of electron density and CI density in the late afterglow are shown in Fig. 4.20. The transformation from electron-ion plasma during the on period to ion-ion plasma in the off period was more dominant at lower pulse repetition frequencies. This is because the pulse off period is long enough for the electron density to decay and for the plasma to become very electronegative in the late afterglow. For the 20 kHz case, the plasma is still electron-ion plasma in the late afterglow. The spatial distribution of CI density shows an island of higher negative ion density at the periphery as seen in Figs. 4.20(f) and 4.6(c)-(e). This is because the ions are not able to move to the center of the plasma during the on period of the pulse due to its inertia. These lobes are observed at higher pulse repetition frequencies as the pulse off time is not sufficient for the ions to respond to the changes in plasma potential.

The temporal evolution of plasma potential and electron temperature are shown in Figs. 4.21 and 4.22, respectively. The peak in the electron temperature is higher at lower pulse repetition frequencies as the power deposition is occurring in a smaller number of

electrons in the late afterglow. As the rate of decay of plasma potential and electron temperature depends on the rate of inelastic collision frequency, it was similar for all cases. The electron temperature was about 0.3 eV and the plasma potential was about 3 V for the 20 kHz case, while for the 5 kHz and 10 kHz cases, the electron temperature and plasma potential were 0.042 eV and 0.27 V, respectively.

The electron temperature and plasma potential during the peak in electron temperature are shown in Fig. 4.23. The electron temperature and plasma potential peak near the coil during the initial period of the power-on phase. The peak in electron temperature and plasma potential are larger for the lower pulse repetition frequency. At lower pulse repetition frequency, due to a higher rate of dissociation of C_2 , a lower electron density results at the end of the pulse-off period. When the power is turned on, the power deposition occurs into a smaller number of electrons ($3 \times 10^{10} \text{ cm}^{-3}$), resulting in a higher electron temperature at lower pulse repetition frequencies.

Thus varying pulse repetition frequency, the plasma can be made into ion-ion plasma, which has significant consequences in fabrication such as reducing charge buildup and notching. Hence, depending on the time needed for the wafer to be exposed to the negative ions, the pulse repetition frequency could be modulated to achieve the desired process requirement.

4.7 Effect of Pressure

The effect of pressure on plasma properties was investigated by varying the pressure from 10 mTorr to 20 mTorr. The base conditions for the simulations were a peak input power of 300 W, pulse repetition frequency of 10 kHz and duty cycle of 50%. The

peak electron density was higher at lower pressure as seen in Fig. 4.24. As the power is kept constant in all the simulations and the pressure is lowered, the electron temperature increases as the same power deposition occurs in a smaller number of electrons. As the electron temperature is higher at lower pressure, the rate of production of electrons is higher, resulting in a higher electron density at lower pressure. The effect of higher electron temperature counteracts the decrease in neutral density, thus resulting in higher electron density. However, in the afterglow the electron density is lower at lower pressure because the effective ambipolar diffusion rate increases with the decrease in pressure. This is because the effective diffusion coefficient scales with the electron temperature, which increases as the pressure decreases. The electron temperatures in the late afterglow were about 0.5 eV and 0.042 eV at pressure of 10 mTorr and 20 mTorr, respectively. The time evolution of CI density is shown in Fig. 4.25. The CI density is higher for the 20 mTorr case as the rate of dissociative attachment is higher at higher pressures due to increased neutral density. The peak in the CI density in the power turn-on period is higher at higher pressures as the afterglow negative ion density was higher at higher pressures. The spatial distribution of electron density and CI density in the late afterglow is shown in Fig. 4.26. At higher pressures, the plasma was more electronegative as the production of negative ions was enhanced at higher pressure due to the higher rate of dissociative attachment, though the electron density distribution was nearly similar.

The temporal dynamics of plasma potential and electron temperature as the pressure is varied are shown in Figs. 4.27 and 4.28. The electron temperature and plasma potential peaked to higher values at lower pressure. This is because the lower neutral density at lower pressure results in a smaller number of electrons to which the same

power is deposited. The peak electron temperature was 5.5 eV and plasma potential was 42 V for a pressure of 10 mTorr, while the electron temperature peaked at 5 eV and plasma potential at 32 V for a pressure of 20 mTorr. The decay and rise times for electron temperature were also similar at different pressures. The spatial distribution of plasma potential and electron temperature during the peak in electron temperature is shown in Fig. 4.29. The plasma potential and electron temperature peak near the coils, where the electric fields from the inductive coils are the largest. After the peak in electron temperature, the electrons begin to lose energy due to inelastic collisions and hence the electron temperature falls to the value of 3 eV, corresponding to continuous wave operation. Therefore, for low pressure processing applications, the power turn on has to be done carefully because the electron temperature peaks to very high values that can cause device damages.

4.8 Conclusions

The consequences of varying pulse repetition frequency, duty cycle, pressure, and power in Ar/Cl₂ ICPs were investigated in the present study. The 2-D simulations were performed by varying the important plasma operating parameters. The temporal dynamics of CI density were dependent on duty cycle and pulse repetition frequency. As the duty cycle was varied from 70% to 10%, CI density showed a peak of about $9 \times 10^{10} \text{ cm}^{-3}$ in the afterglow at about 50 μs after power-off. The inertia of the negative ions to respond to the changes in plasma potential resulted in lobes of higher negative ion density in the periphery. It takes about 25 μs for the ions to respond to the changes in the plasma potential and move to the center of the plasma. The electron density showed a non-

monotonic behavior as observed in experiments, as the pulse repetition frequency was varied.¹ As the pulse repetition frequency is varied, the transition from electron-ion plasma to ion-ion plasma can be controlled. The time averaged electron density and CI density were higher at higher pulse repetition frequencies. The time averaged electron densities were about $4.3 \times 10^{11} \text{ cm}^{-3}$ and $3.6 \times 10^{11} \text{ cm}^{-3}$ for 20 kHz and 5 kHz, respectively. The dynamics of electron temperature and plasma potential did not vary with changes in power. The peak electron temperature was about 8 eV and the peak plasma potential was about 40 V for power varying from 165 W to 300 W. The spatial distribution of electron temperature showed a larger peak in electron temperature at lower pulse repetition frequency, pressure, and duty cycle. The model predicted results which were qualitatively similar to the experiments performed in pulsed electronegative plasmas.^{1, 2} The model was able to predict the non monotonic behavior with pulse repetition frequency and the spatial distribution of CI density, which was not accurately predicted by the 1-D models.³

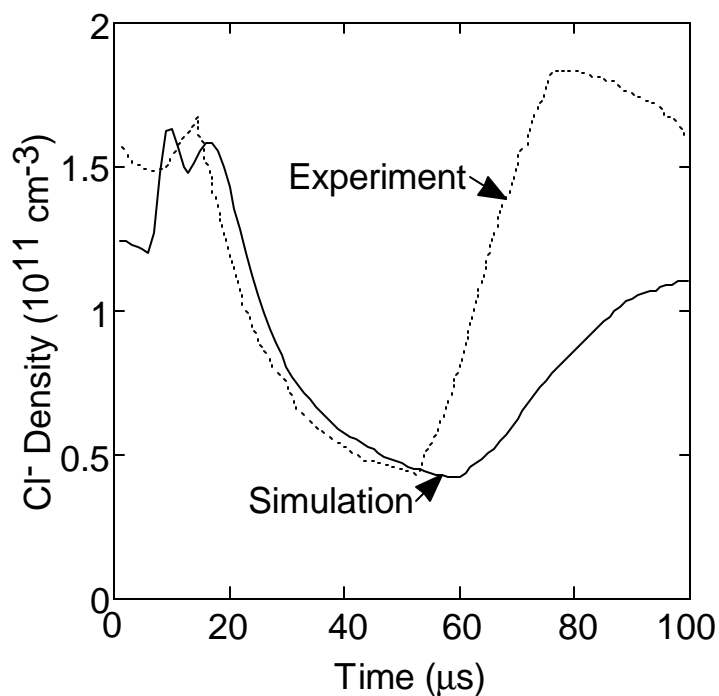


Figure 4.1 Comparison of CF⁻ density in C₂ (experiment) and Ar/C₂ (simulation) to show that the model captures the trends in temporal evolution of negative ion density in electronegative plasmas.

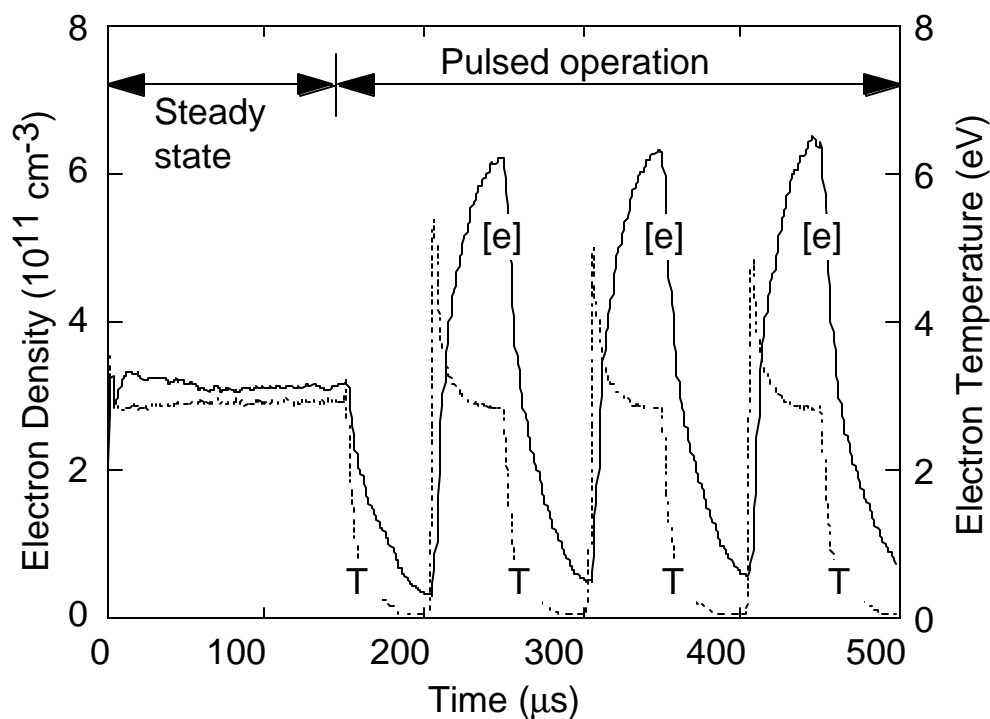


Figure 4.2 Electron density and plasma potential at different times for a peak input power of 300 W, pulse repetition frequency of 10 kHz, and duty cycle of 50%.

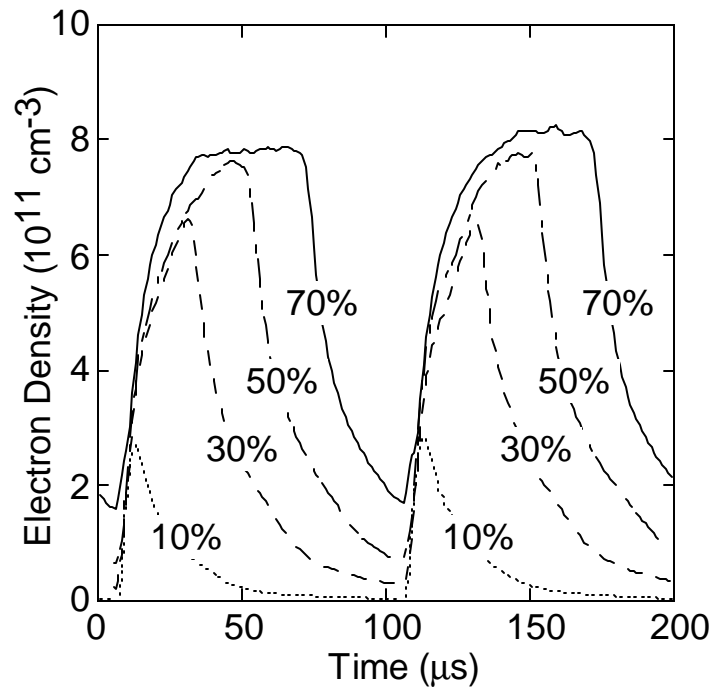


Figure 4.3 Electron density at different times as a function of duty cycle for a peak input power of 300 W and pulse repetition frequency of 10 kHz.

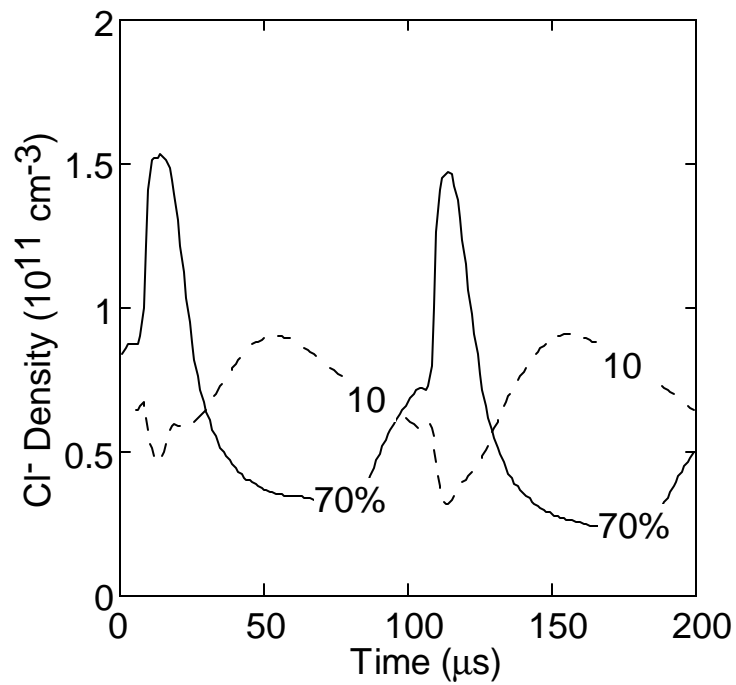


Figure 4.4 Cl⁻ density at different times as a function of duty cycle for a peak input power of 300 W and pulse repetition frequency of 10 kHz.

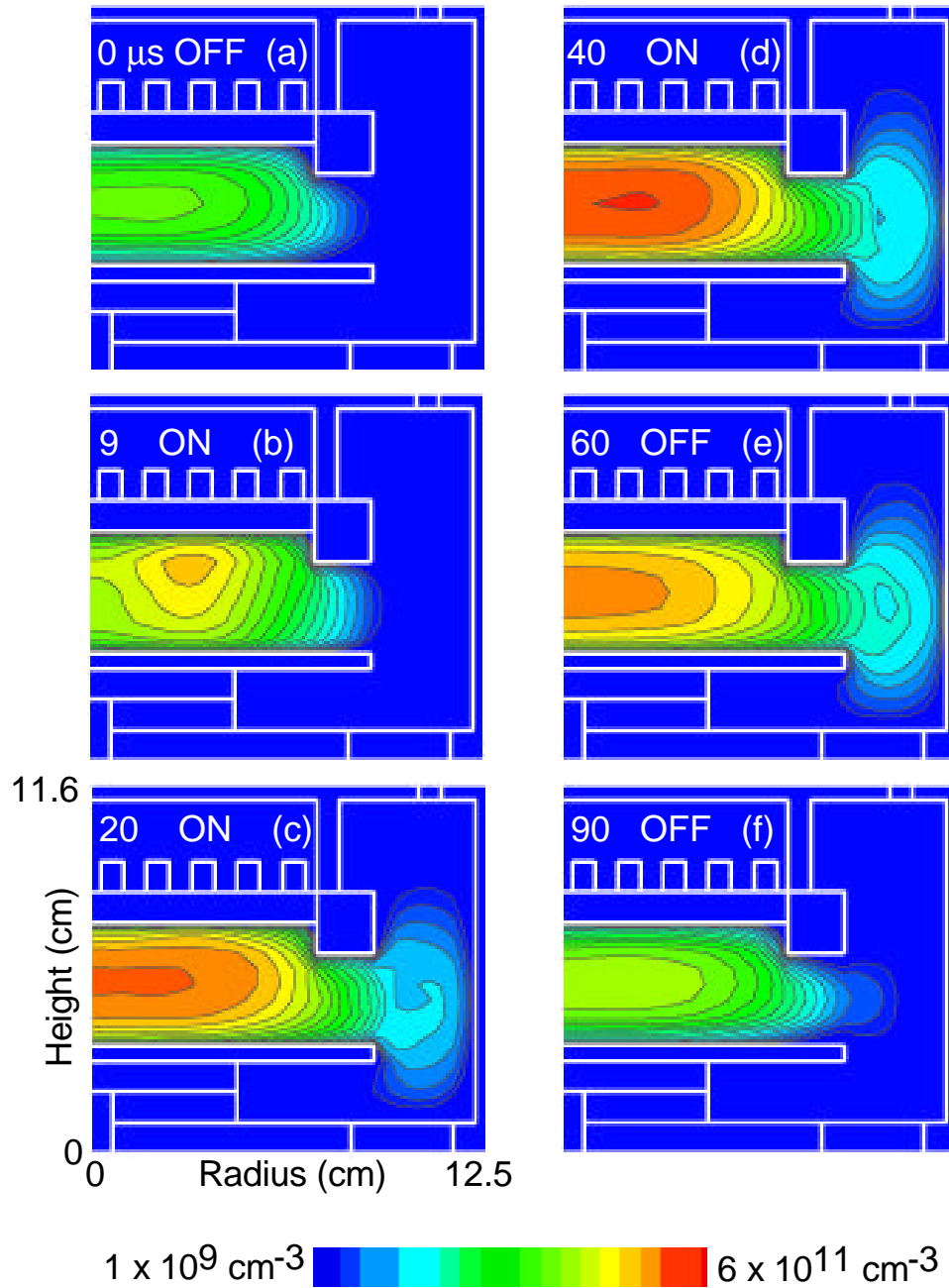


Figure 4.5 Electron density for a single pulse at different times for a peak power of 300 W, pulse repetition frequency of 10 kHz and duty cycle of 50%. The figures a, b, c, and d are at 0 μs , 9 μs , 20 μs , 40 μs during the pulse after the power is turned on and figures e, and f are at 60 μs , 90 μs during the pulse after the power is turned off at 50 μs .

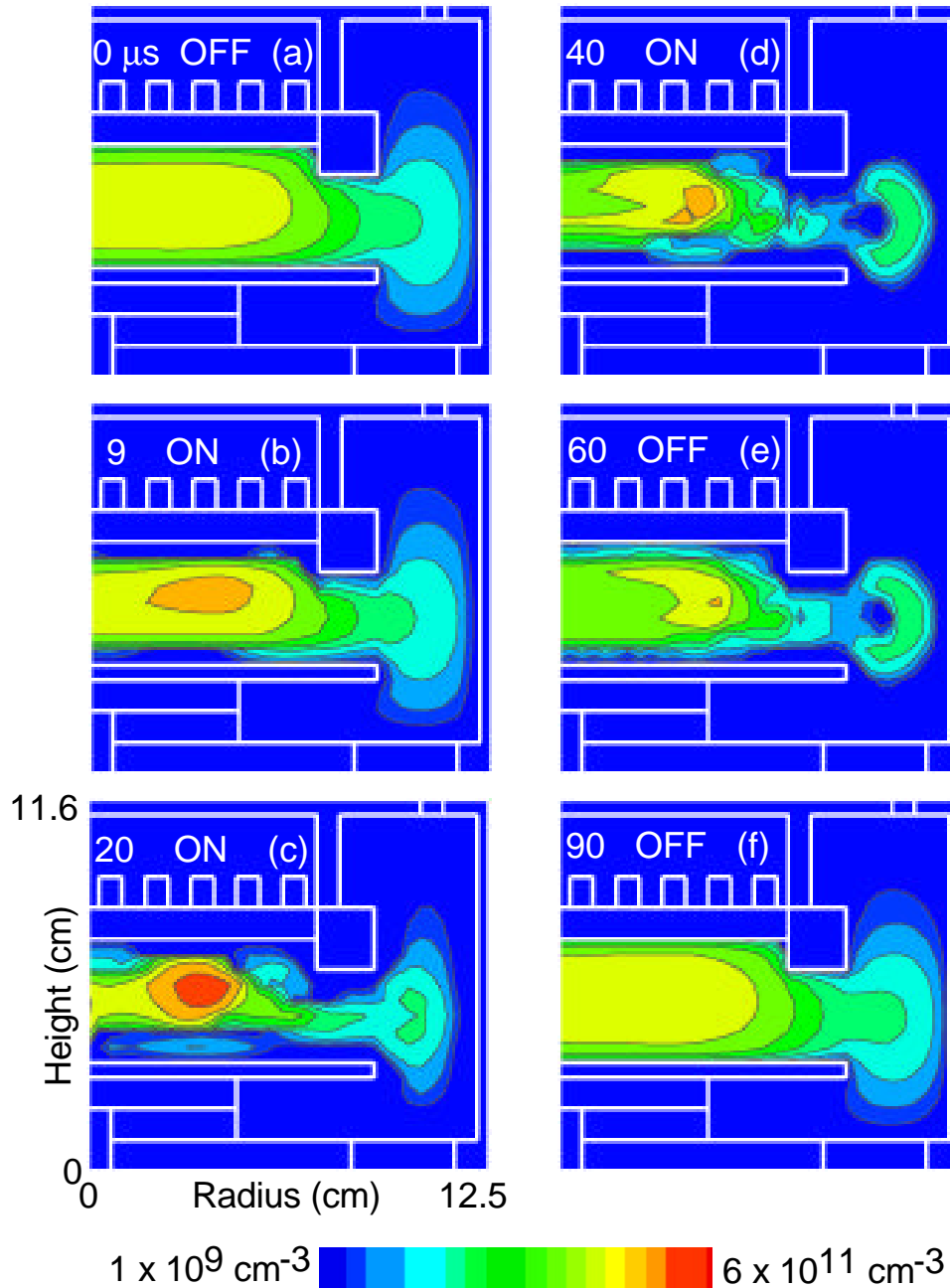


Figure 4.6 CI density for a single pulse at different times for a peak power of 300 W, pulse repetition frequency of 10 kHz and duty cycle of 50%. The figures a, b, c, and d are at 0 μs , 9 μs , 20 μs , 40 μs during the pulse after the power is turned on and figures e, and f are at 60 μs , 90 μs during the pulse after the power is turned off at 50 μs .

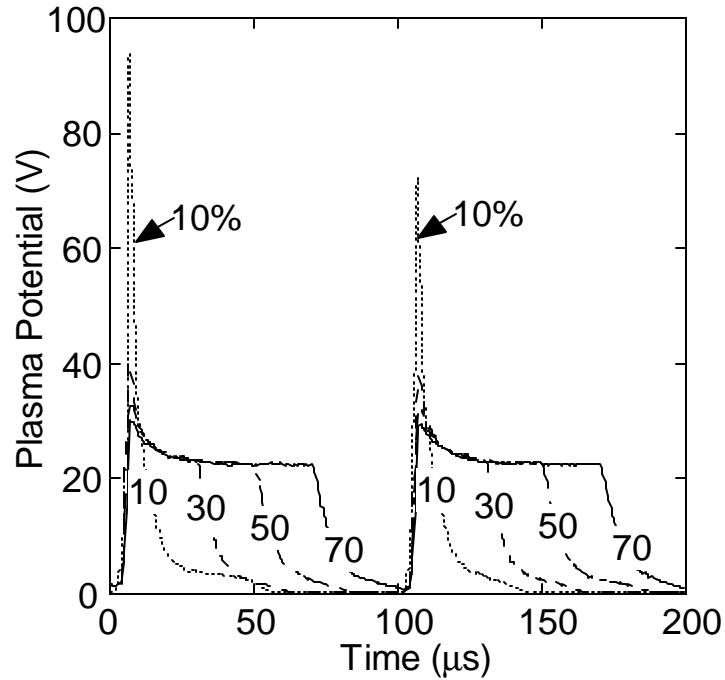


Figure 4.7 Plasma potential at different times as a function of duty cycle for a peak input power of 300 W and pulse repetition frequency of 10 kHz.

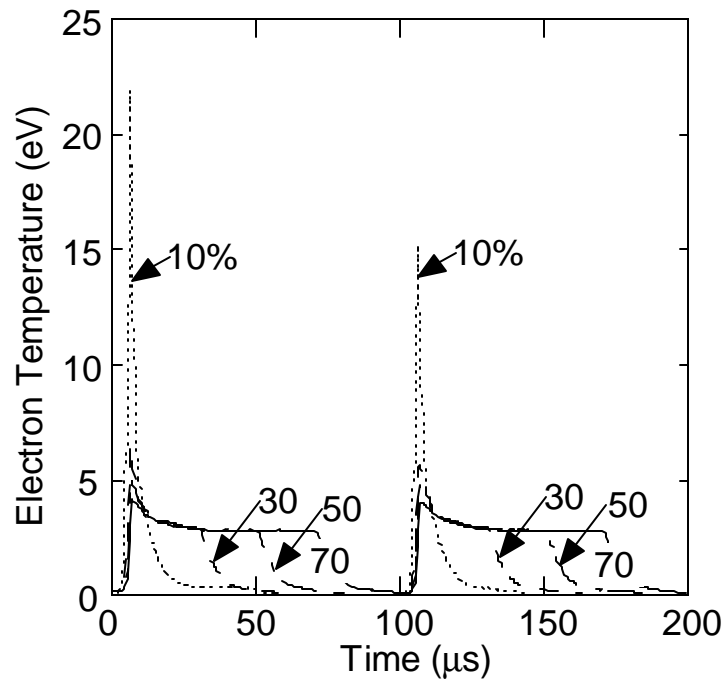


Figure 4.8 Electron temperature at different times as a function of duty cycle for a peak input power of 300 W and pulse repetition frequency of 10 kHz.

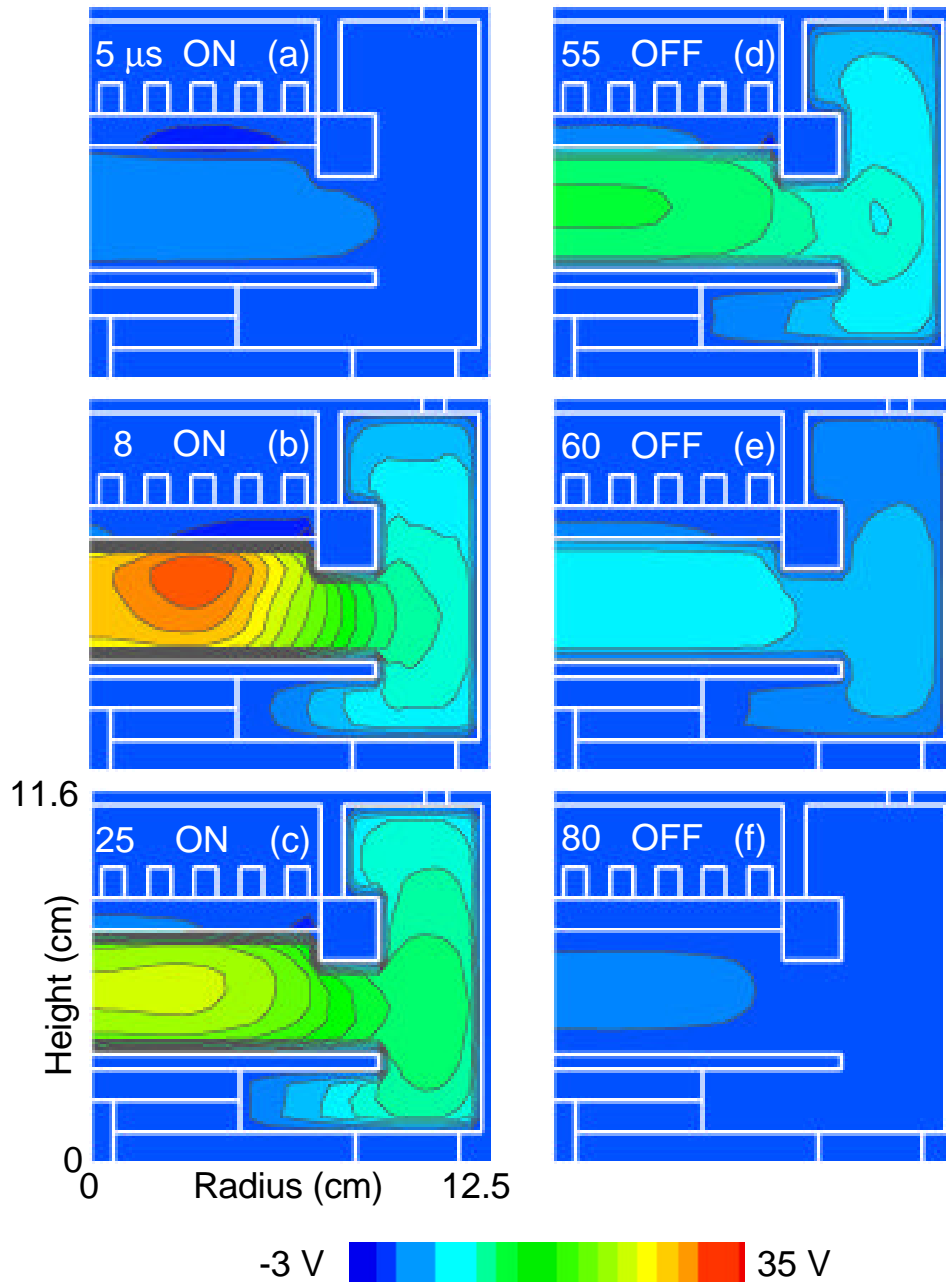


Figure 4.9 Plasma potential for a single pulse at different times for a peak power of 300 W, pulse repetition frequency of 10 kHz, and duty cycle of 50%. The figures a, b, and c are at 5 μ s, 8 μ s, 25 μ s during the pulse after the power is turned on and figures d, e, and f are at 55 μ s, 60 μ s, 80 μ s during the pulse after the power is turned off at 50 μ s.

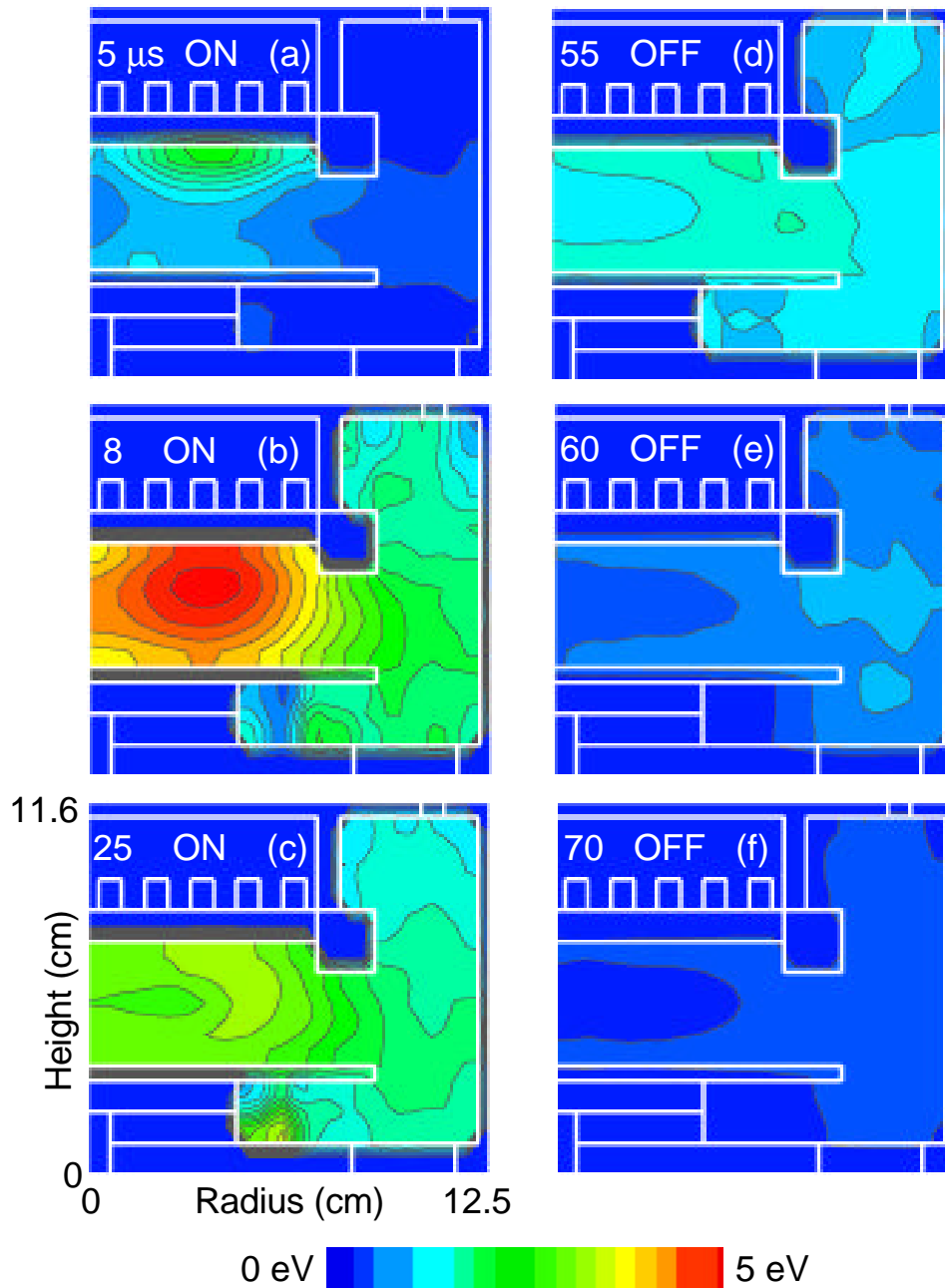


Figure 4.10 Electron temperature for a single pulse at different times for a peak power of 300 W, pulse repetition frequency of 10 kHz, and duty cycle of 50%. The figures a, b, and c are at 5 μs , 8 μs , 25 μs during the pulse after the power is turned on and figures d, e, and f are at 55 μs , 60 μs , 70 μs during the pulse after the power is turned off at 50 μs .

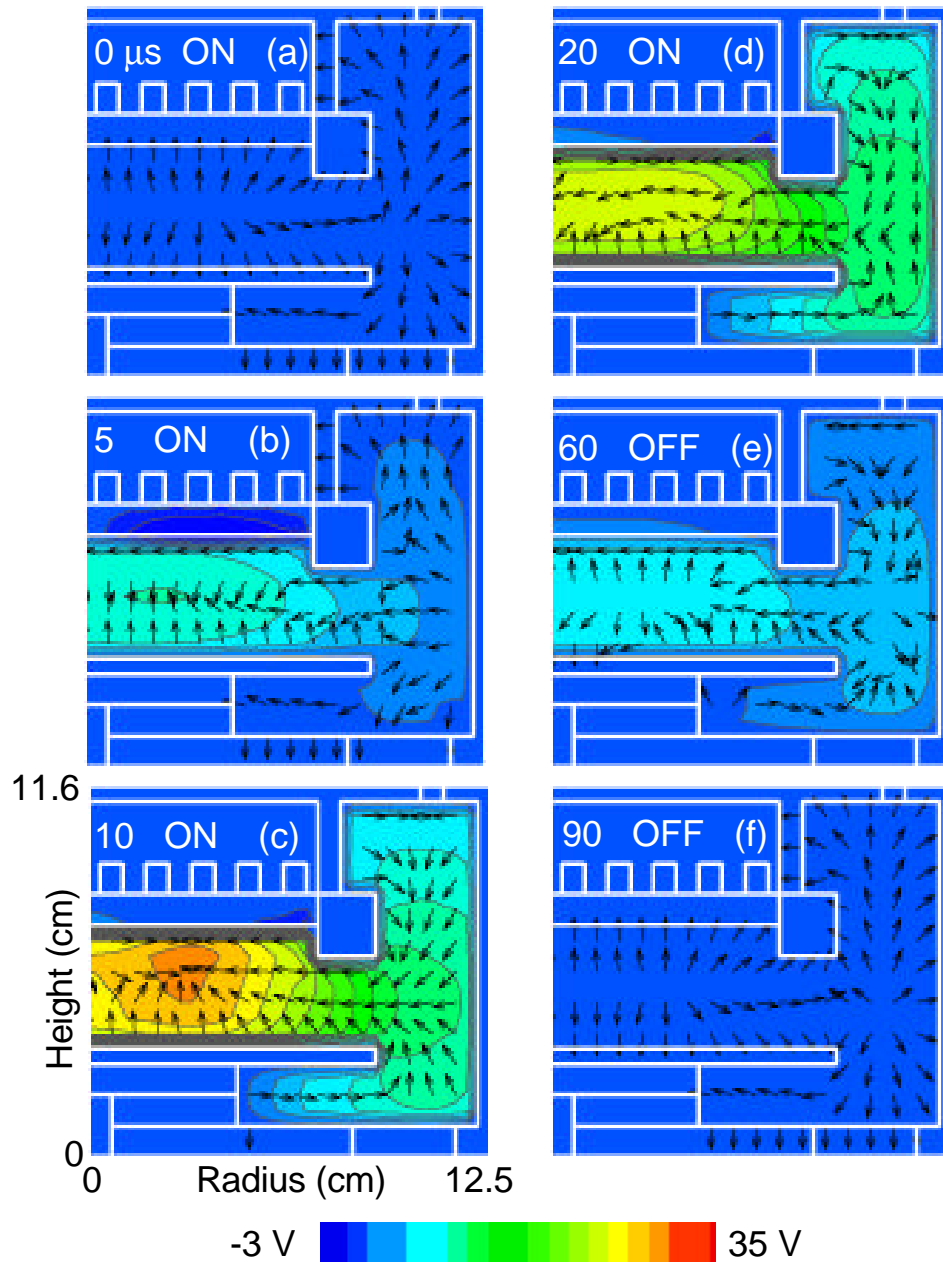


Figure 4.11 CI flux and plasma potential for a single pulse at different times for a peak power of 300 W, pulse repetition frequency of 10 kHz, and duty cycle of 50%. (CI flux vectors are all of same length and not scaled with respect to the magnitude.) The figures a, b, c, and d are at 0 μ s, 5 μ s, 10 μ s, 20 μ s during the pulse after the power is turned on and figures e and f are at 60 μ s, 90 μ s during the pulse after the power is turned off at 50 μ s.

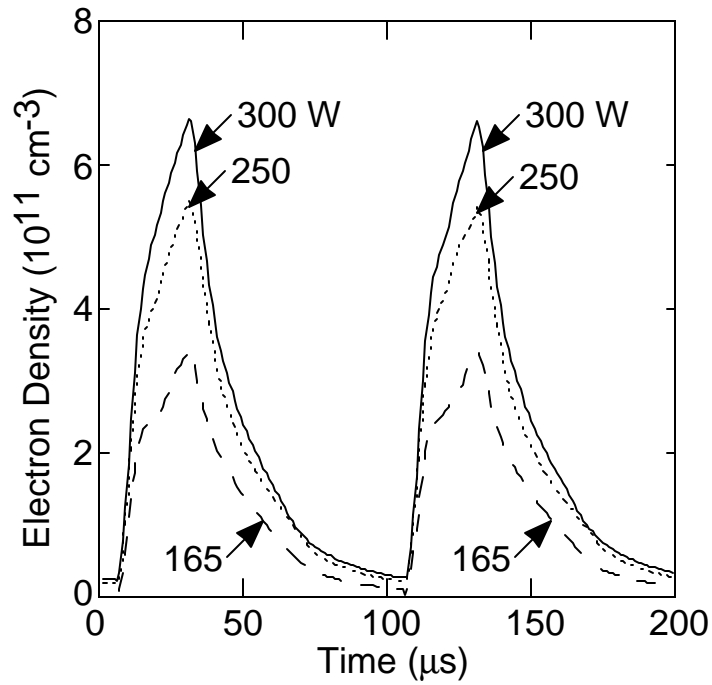


Figure 4.12 Electron density at different times as a function of peak input power for a pulse repetition frequency of 10 kHz and duty cycle of 30%.

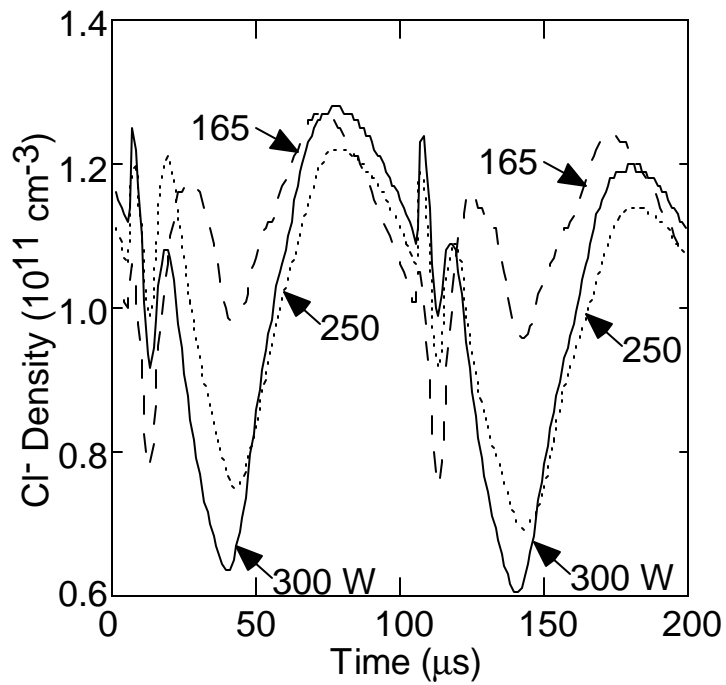


Figure 4.13 Cl⁻ density at different times as a function of peak input power for a pulse repetition frequency of 10 kHz and duty cycle of 30%.

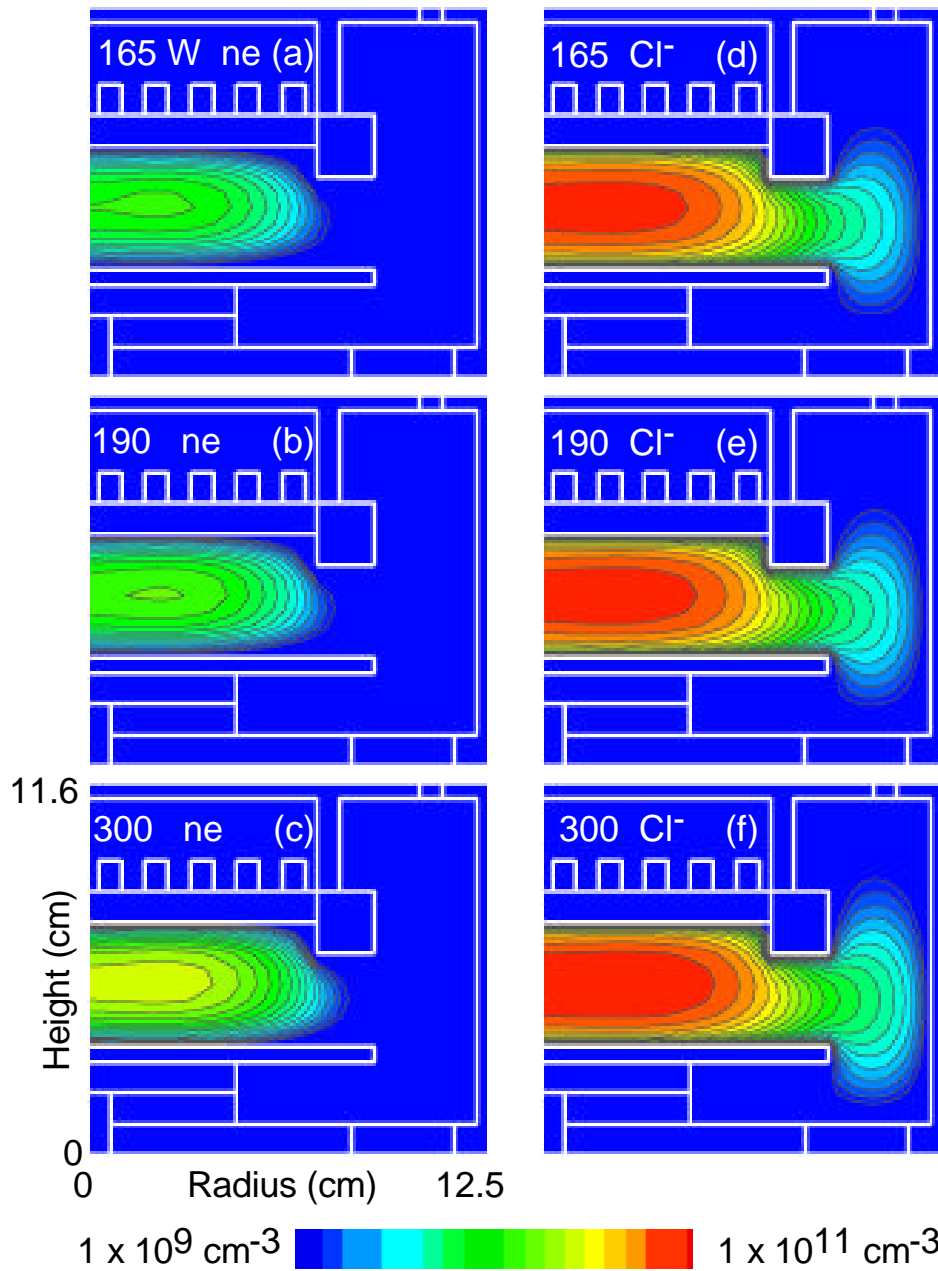


Figure 4.14 Electron density (n_e) (a-c) and Cl⁻ density (d-f) in the late afterglow as a function of power for a pulse repetition frequency of 10 kHz and duty cycle of 30%.

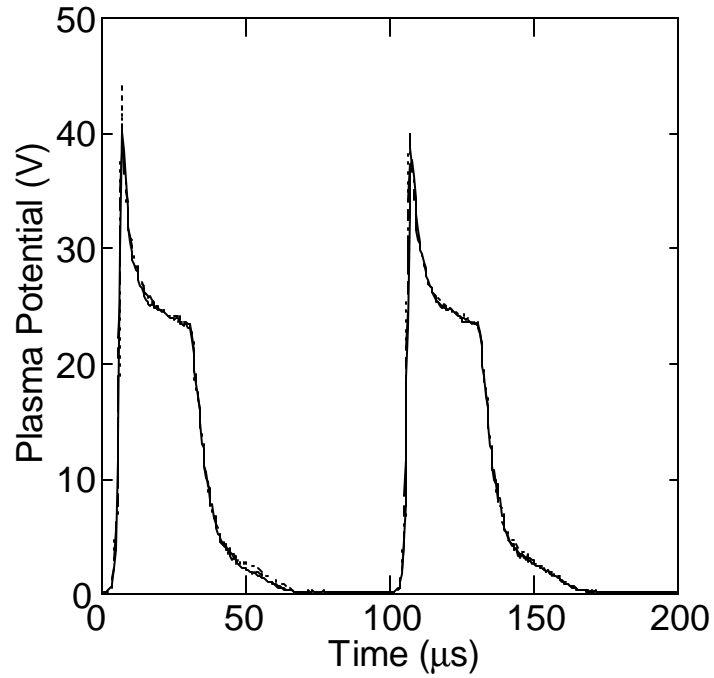


Figure 4.15 Plasma potential at different times as a function of peak input power for a pulse repetition frequency of 10 kHz and duty cycle of 30%.

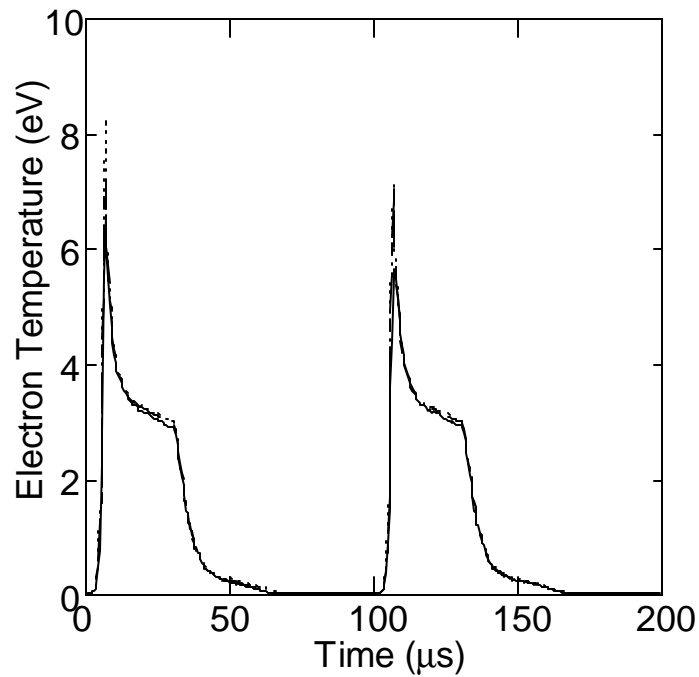


Figure 4.16 Electron temperature at different times as a function of peak input power for a pulse repetition frequency of 10 kHz and duty cycle of 30%.

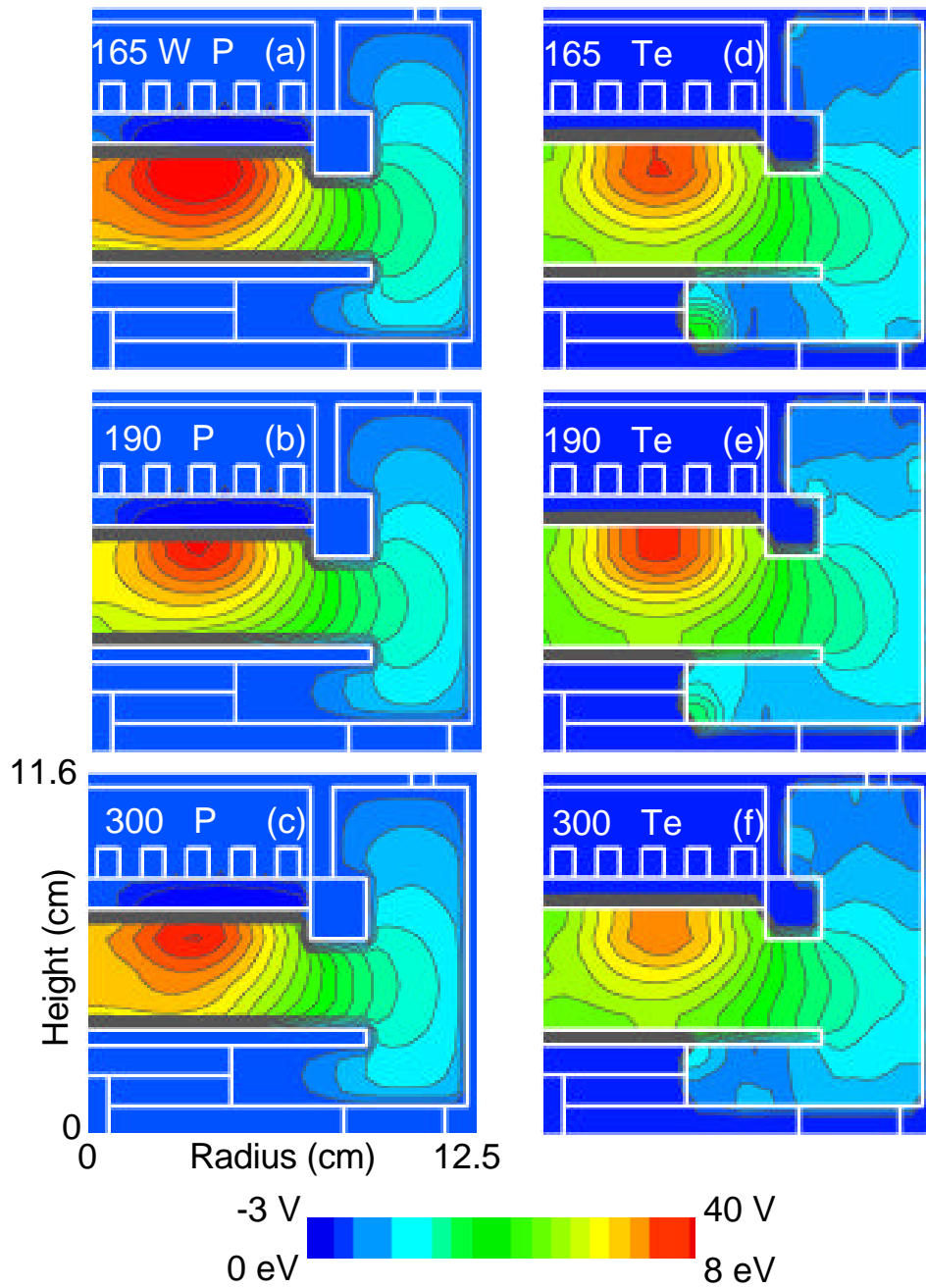


Figure 4.17 Plasma potential (P) (a-c) and electron temperature (Te) (d-f) when the peak in electron temperature occurs during the pulse as a function of power for a pulse repetition frequency of 10 kHz and duty cycle of 30%.

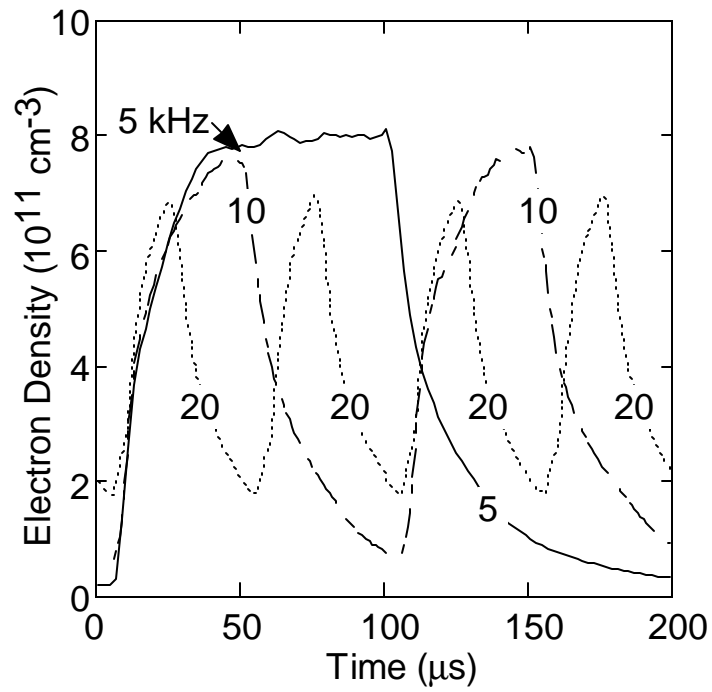


Figure 4.18 Electron density at different times as a function of pulse repetition frequency for a peak input power of 300 W and duty cycle of 50%.

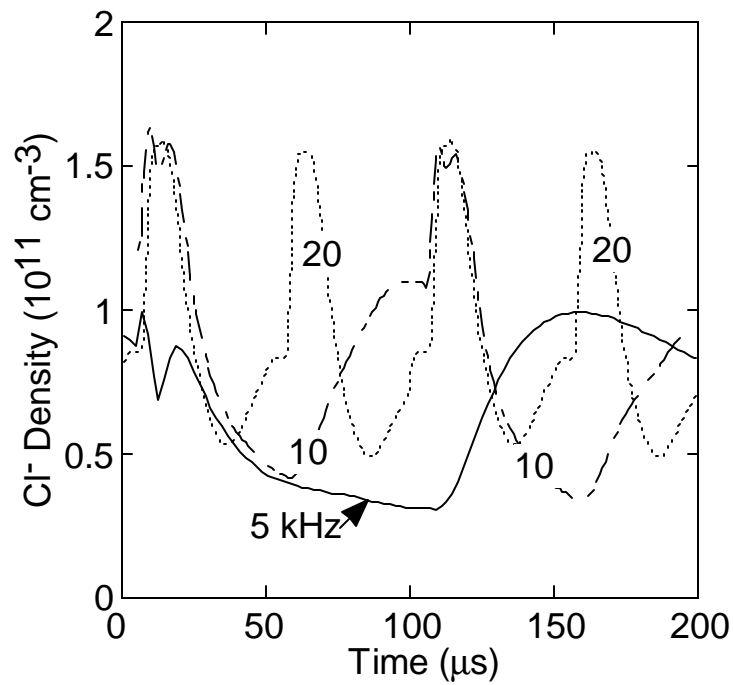


Figure 4.19 Cl⁻ density at different times as a function of pulse repetition frequency for a peak input power of 300 W and duty cycle of 50%.

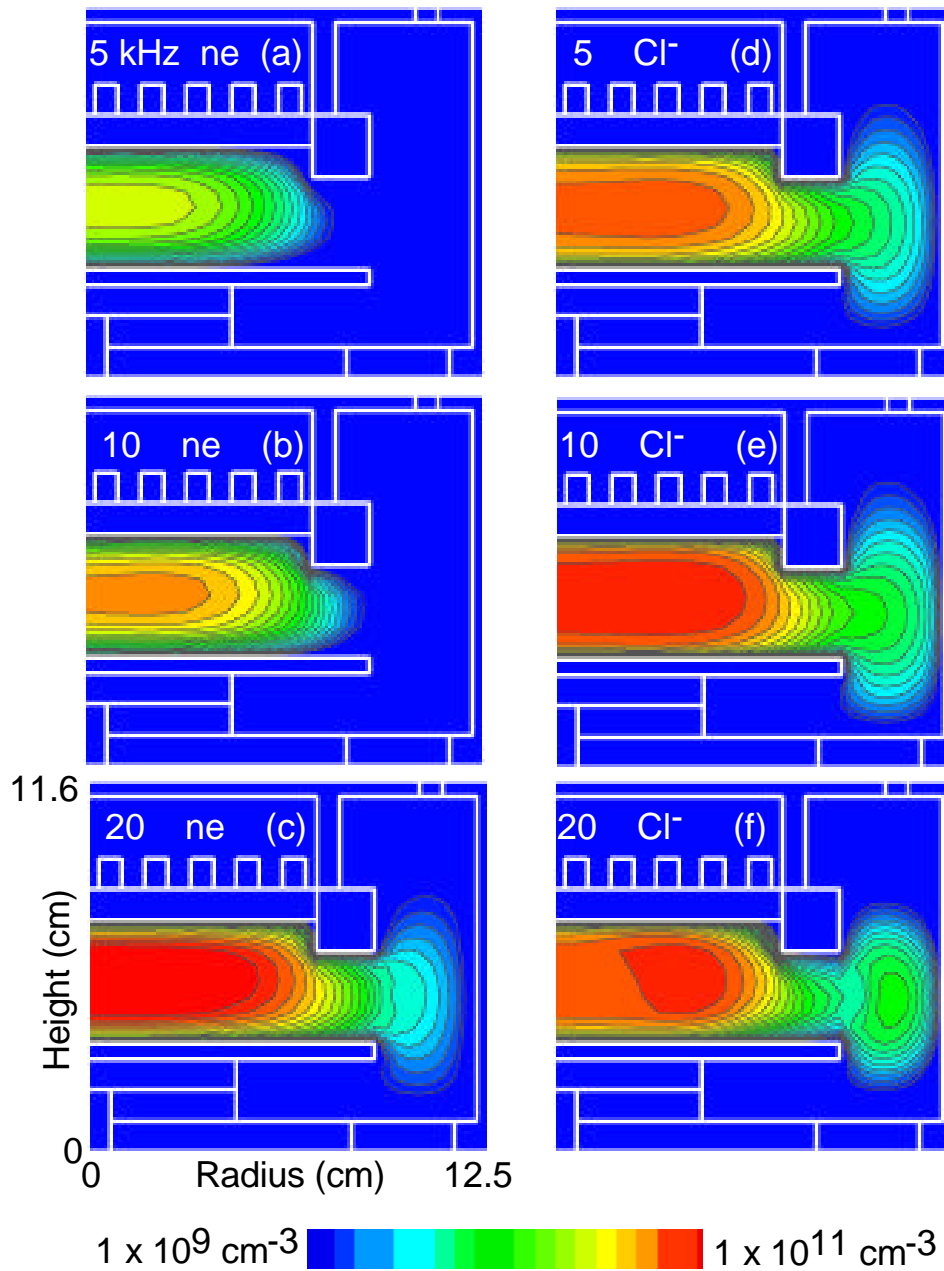


Figure 4.20 Electron density (n_e) (a-c) and Cl⁻ density (d-f) in the late afterglow as a function of pulse repetition frequency for a peak power of 300 W and duty cycle of 50%.

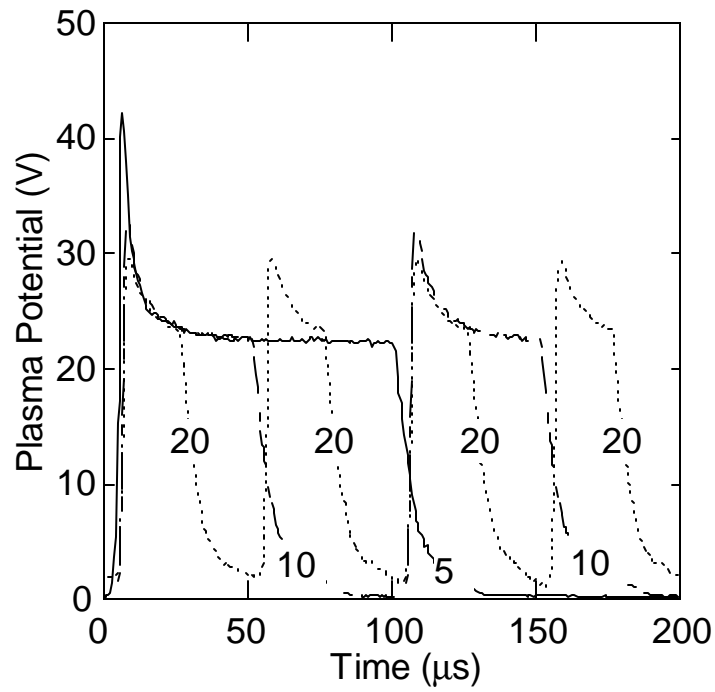


Figure 4.21 Plasma potential at different times as a function of pulse repetition frequency (kHz) for a peak input power of 300 W and duty cycle of 50%.

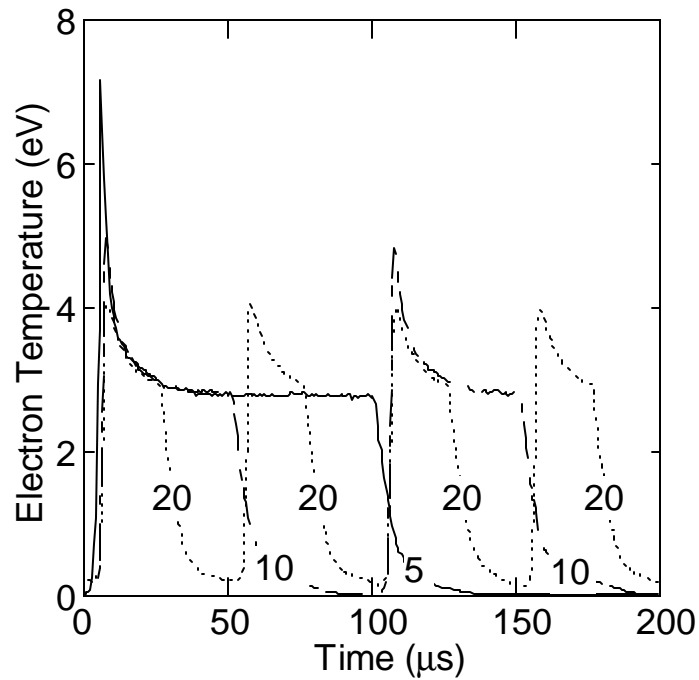


Figure 4.22 Electron temperature at different times as a function of pulse repetition frequency (kHz) for a peak input power of 300 W and duty cycle of 50%.

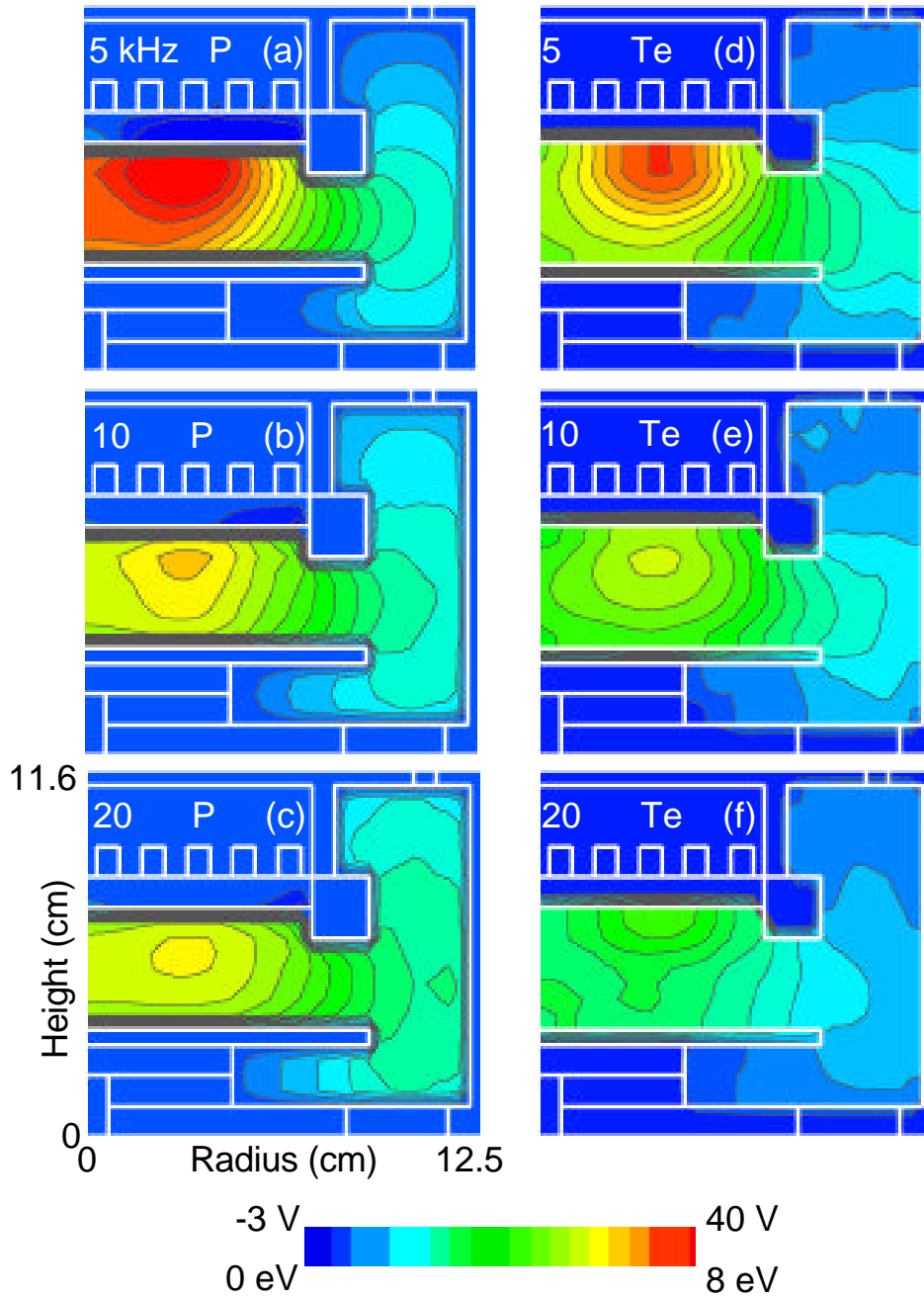


Figure 4.23 Plasma potential (P) (a-c) and electron temperature (Te) (d-f) when the peak in electron temperature occurs during the pulse as a function of pulse repetition frequency for a peak power of 300 W and duty cycle of 50%.

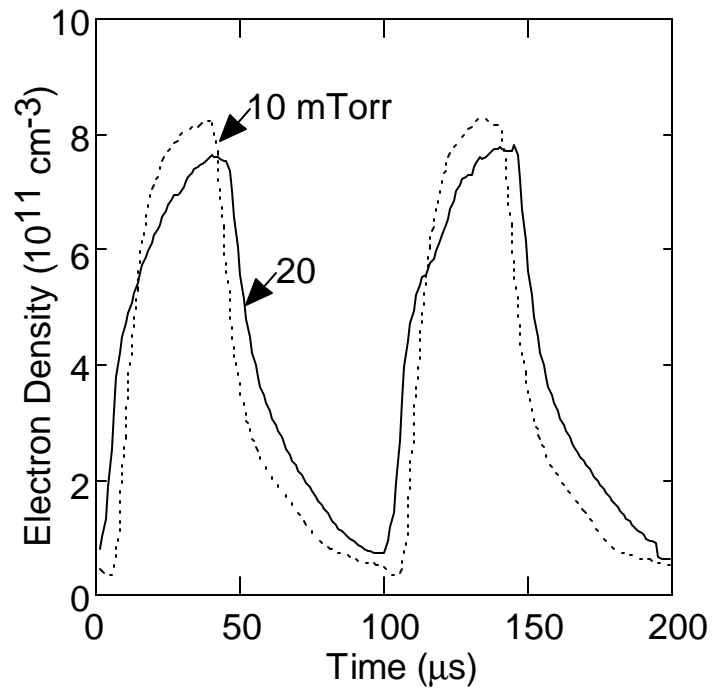


Figure 4.24 Electron density at different times as a function of pressure for a peak input power of 300 W, pulse repetition frequency of 10 kHz, and duty cycle of 50%.

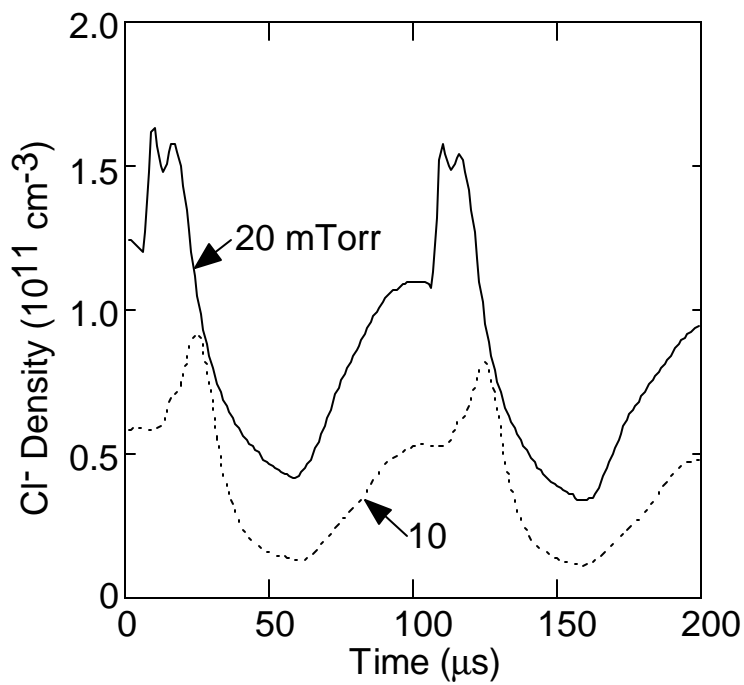


Figure 4.25 Cl⁻ density at different times as a function of pressure for a peak input power of 300 W, pulse repetition frequency of 10 kHz, and duty cycle of 50%.

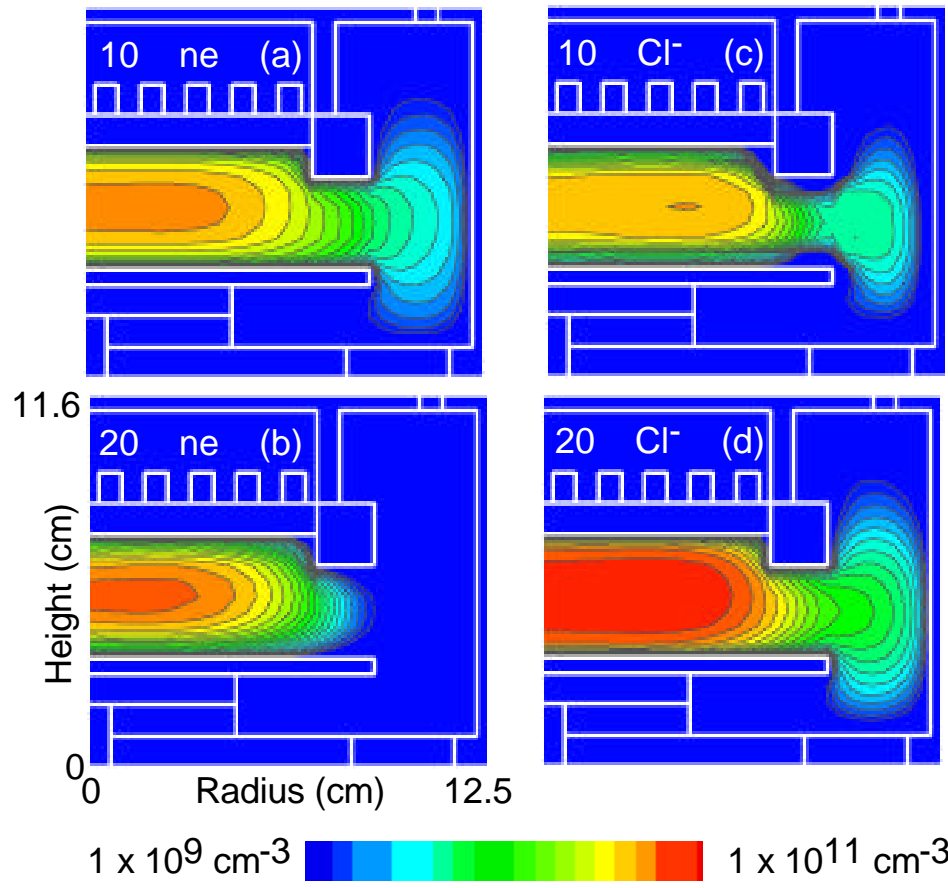


Figure 4.26 Electron density (n_e) (a-b) and Cl^- density (c-d) in the late afterglow as a function of pressure (mTorr) for a peak power of 300 W, pulse repetition frequency of 10 kHz and duty cycle of 50%.

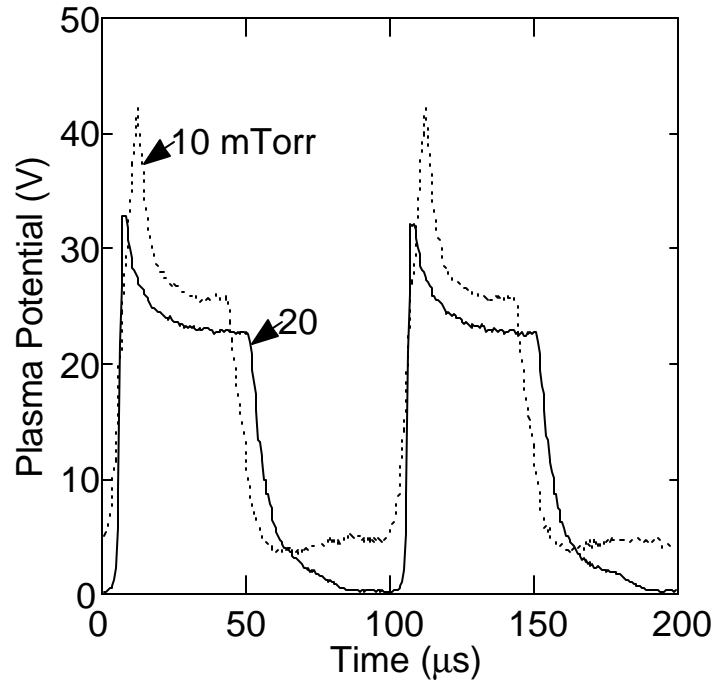


Figure 4.27 Plasma potential at different times as a function of pressure for a peak input power of 300 W, pulse repetition frequency of 10 kHz, and duty cycle of 50%.

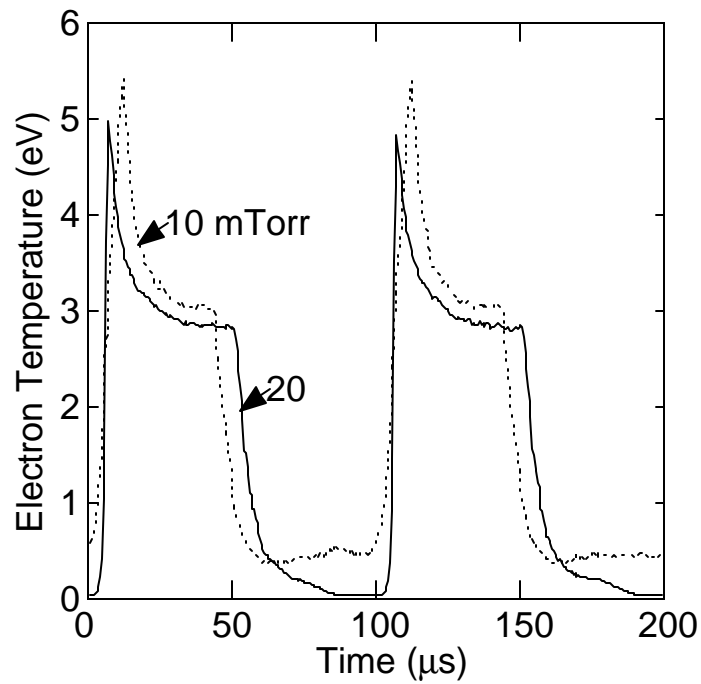


Figure 4.28 Electron temperature at different times as a function of pressure for a peak input power of 300 W, pulse repetition frequency of 10 kHz, and duty cycle of 50%.

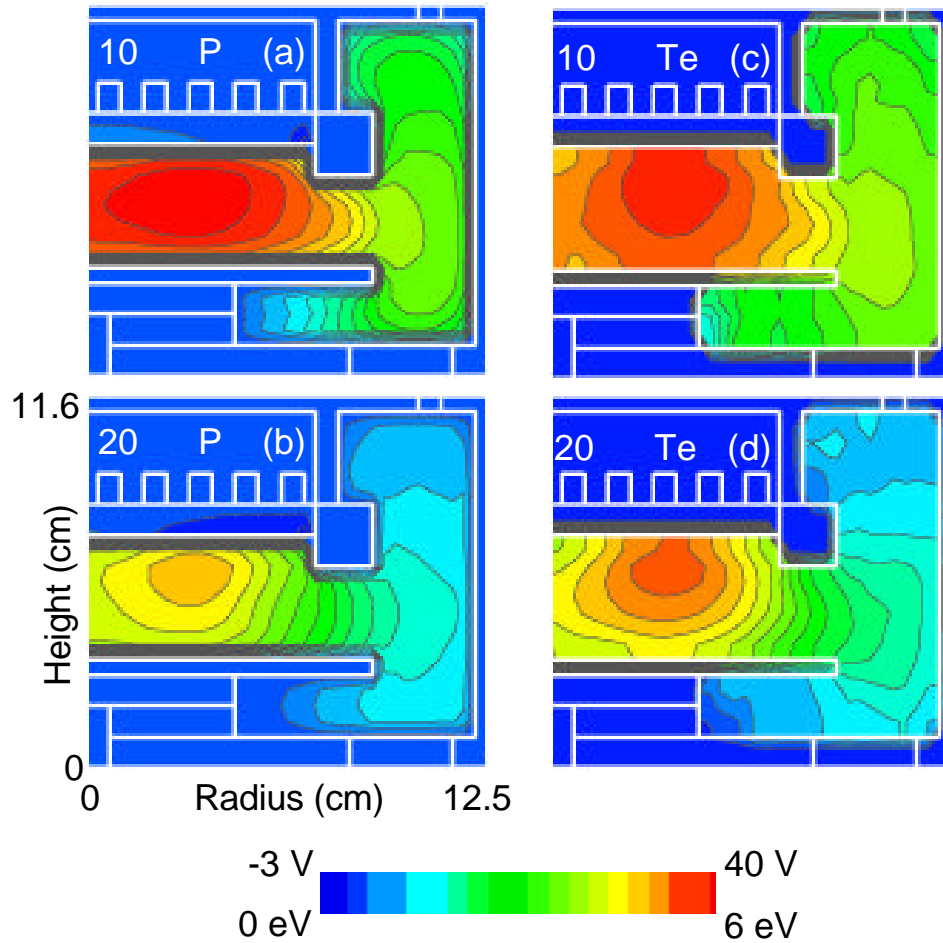


Figure 4.29 Plasma potential (P) (a-b) and electron temperature (Te) (c-d) when the peak in electron temperature occurs during the pulse as a function of pressure (mTorr) for a peak power of 300 W, pulse repetition frequency of 10 kHz, and duty cycle of 30%.

4.9 References

31. G. A. Hebner and C. B. Fleddermann, *J. Appl. Phys.* **82**, 2814 (1997)
32. M. V. Malyshev, V. M. Donnelly, S. Samukawa, and J. I. Colonell, *J. Appl. Phys.* **86**, 4813 (1999)
33. V. Midha and D. J. Economou, *Plasma Sources Sci. Technol.* **9**, 256 (2000)

5. CONCLUSIONS

Quantifying transient plasma processing phenomena such as startup, shutdown, recipe changes, and pulsed operation is important to optimizing plasma and materials properties. There have been only a few modeling efforts to investigate pulse modulated high plasma density low pressure ICPs. Global and 1-D models were inadequate to study the effect of pulsed plasmas as the experimental setup is at least two dimensional. Two dimensional models are needed to characterize pulsed plasmas, which is emerging as a promising candidate for achieving improved etch rate, uniformity, and selectivity.

A new 2-D model was proposed for addressing transients based on moderate parallelism, which interfaces the short scale plasma time scales with the long term neutral time scales. Plasma transport, neutral fluid transport, and electromagnetics are simultaneously computed on separate processors. Fluid conditions (e.g., changes in pressure, mole fractions, and flow fields) which are slowly evolving over time are made available to the simultaneous calculation of plasma properties (e.g., electron and ion density, electrostatic fields) through shared memory.

Computational studies were performed for pulsed operation in argon ICPs. Investigations showed that pulse repetition frequency and duty cycle can significantly change plasma properties such as electron density, electron temperature, and plasma potential. In the present study, the 2-D simulations were performed by varying duty cycle, power, pulse repetition frequency, and pressure. The peak electron temperature increased with a decrease in duty cycle as the same power was deposited into a smaller number of electrons. The dynamics of plasma potential and electron temperature did not vary much with changes in peak input power as the increased power was deposited to a

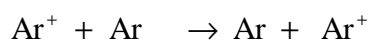
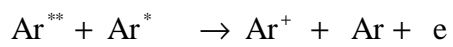
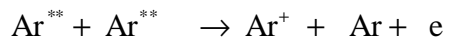
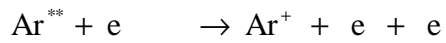
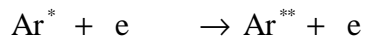
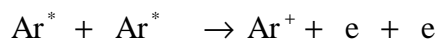
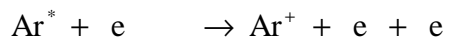
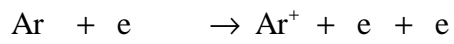
larger number of electrons, which scales almost linearly with power. As the pulse repetition frequency decreased, the peak in electron temperature increased. The spatial distribution of electron temperature showed a larger peak at lower pulse repetition frequencies. The spatial distribution of electron density showed that losses due to diffusion are higher at lower pressures in the late afterglow. The simulation results compared well with the experiments. The dynamics predicted captured the experimental trends closely. The rise and fall times predicted by the model were similar to the times reported.

The consequences of varying pulse repetition frequency, duty cycle, pressure, and power in Ar/C₂ ICPs were also investigated. The temporal dynamics of CI density were dependent on duty cycle and pulse repetition frequency. As the pulse repetition frequency is varied, the transition from electron-ion plasma to ion-ion plasma can be controlled. The spatial distribution of electron temperature showed a larger peak in electron temperature at lower pulse repetition frequency, pressure, and duty cycle as the power deposition occurs in a smaller number of electrons left in the plasma at the end of the off period. The model results were qualitatively similar to the experiments performed in pulsed electronegative plasmas.

The effect of RF bias on the substrate during the pulsed operation can also be investigated by employing the numerical technique developed. The proposed method can be extended to study pulsed ECRs. The charge buildup in fine features during etching can be adequately modeled by interfacing the parallel equipment scale model (HPEM-P) and the feature scale model.

APPENDIX A: LIST OF REACTIONS FOR Ar

The reaction chemistry for argon used in the present study is given below:



APPENDIX B : LIST OF REACTIONS FOR Ar/Cl₂

The reaction chemistry for an Ar/Cl₂ gas mixture used in the present study is given below:

